Analysis of neutrophil chemotaxis spatial signal processing using optogenetic receptor control

By

GEORGE R.R. BELL
DISSERTATION

Submitted in partial satisfaction of the requirements for the degree of

DOCTOR OF PHILOSOPHY

in

Biochemistry, Molecular, Cellular, and Developmental Biology

in the

OFFICE OF GRADUATE STUDIES

of the

UNIVERSITY OF CALIFORNIA

DAVIS

Approved:

Sean Collins, Chair

Lesilee Rose

Edward Pugh

Committee in Charge

2021

Contents

Abstract

Neutrophils are early responders of the innate immune system that use chemotaxis, the directed migration of cells along a chemical gradient, to reach sites of infection and inflammation. Deciphering the spatial patterns of chemoattractant signals is a fundamental challenge at the cellular level due to diffusion and inherent stochasticity of signaling molecules. Despite these sources of noise, neutrophils respond to changing chemoattractant gradients with high spatial and temporal precision by integrating information from receptors with a cell-autonomous polarity and motility signaling program[1–4]. The wiring of the chemotaxis signaling network is complex with multiple layers of feedbacks and potentially feedforward connections. Understanding how cell polarity programs interpret and respond to chemotaxis receptor signals remains a key challenge in the field, as deciphering the interconnections of the network are not trivial. To better understand how cell polarity regulators in the Rho GTPase family signal within chemotaxing cells, I developed a high-magnification chemotaxis assay that enables measurement of Rho GTPase activity biosensors downstream of photo-activation of chemoattractants (Chapter 2).

Chemoattractant gradients are inherently spatial, and it remains unclear how cells encode this spatially relevant information from the receptors in the downstream chemotaxis signaling programs. Experiments using diffusible chemoattractants are limiting, as achieving well-defined and highly local

receptor stimulation is unfeasible. To overcome this challenge, I developed a new molecular tool kit that uses light-driven chemotaxis signaling to improve the spatial and temporal control of receptor activation. I paired this receptor with a red-shifted biosensor for a cell front polarity regulator, enabling stimulation and response measurements in the same cells. Using this system, I explored how cell polarity signals are propagated in space and time downstream of receptor stimulation. Additionally, I investigated how negative signals shape the polarity response (Chapter 3).

Through collaboration, the light-activated chemotaxis receptor was also used to unlock another experimental question that was limited by chemoattractant diffusion. Specifically, we investigated whether existing cell front/back polarity is resistant to receptor activation at the cell rear (Chapter 4). Collectively, the methodologies developed, and information gleaned from this work lay the foundation for systematic interrogation of spatial signal transduction that occurs during neutrophil chemotaxis.

Acknowledgements

I would like to thank my dissertation advisor, Dr. Sean Collins for his outstanding mentorship. I have grown by leaps and bounds throughout the PhD experience and his advice and guidance have been an important catalyst. I will be sure to keep tabs on the exciting breakthroughs that will come from his research group in the future!

I would like to thank my dissertation committee members, Dr. Lesilee Rose and Dr. Edward Pugh, for their thoughtful critiques of my project and guidance for future directions. Additionally, I would like to thank my collaborators, Amalia Hadjitheodorou and Dr. Julie Theriot for recognizing the potential in my work and then taking it to new heights. It was a pleasure working with you all.

Finally, I would like to thank my lab mates for making the Collins Lab a fun and exciting place to work. Our deep scientific discussions broadened my view of the chemotaxis field and beyond, helping me grow into a better scientist. But more importantly, I am leaving this experience with several life-long friends. Who could ask for better?

Table of Contents

List of Figures

List of Supplementary Figures

Chapter 1

Introduction

1.1 Abstract

This chapter discusses the relevant background information regarding the experiments conducted in this work. Topics include the *in vivo* roles for chemotaxis (1.2), and an introduction to chemotaxis signaling (1.3). Additionally, neutrophil spatial signal processing (1.4) and feedback from the cell polarity circuit to the chemotaxis receptors (1.5) are discussed.

1.2 Biological functions of chemotaxis

Chemotaxis, the directed cellular movement along chemical gradients, is critically important for several biological functions. During embryogenesis, chemotaxis directs cell positioning for tissue and organ formation[5,6], while axon guidance cues direct nervous system wiring[7,8]. Similarly, effective immune system development and function relies on chemotaxis signaling[9,10]. For instance, during the initial phases of pathogen detection or inflammation, circulating neutrophils are among the first leukocytes recruited from the blood via chemotaxis to mediate pathogen killing. Not surprisingly, deficiencies in neutrophil chemotaxis lead to severe fungal and bacterial infections[11,12]. In contrast, hyper recruitment of neutrophils and other immune cells can promote disease, such as atherosclerosis progression in the arterial wall[13–15].

Despite the importance of chemotaxis to human health, our mechanistic understanding of spatial signal processing during chemotaxis remains poorly understood.

1.3 Introduction to neutrophil chemotaxis

Chemotaxis signaling behaviors are highly complex and involve coordinating directional cues from the receptors with the underlying cell polarity network to build morphologically and chemically polarized cell front and rear domains[1,2,16–18]. The polarity network and the actin cytoskeleton are intimately linked[16,19], enabling cells to spontaneously polarize and randomly move in the absence of chemoattractants[20]. In contrast to the "random walk" of unstimulated cells, neutrophils respond to chemoattractants by persistently biasing their motility up the gradient. Thus, to effectively chemotax, the cell must integrate input from the receptors with cell-autonomous polarity, coupling directional sensing and polarity programs[1].

The directional sensing component of the chemotaxis signaling network comprises G-Protein Coupled Receptors (GPCRs) that couple, primarily, to the $G_i\alpha$ family of heterotrimeric G-Proteins[1,21,22]. Heterotrimeric G-Proteins are composed of three subunits, a switch-like Gα subunit and an obligate heterodimer subunit comprising Gβ and Gγ subunits. GPCR signaling uses the following paradigm: In the receptor off-state, the Gα-GDP subunit is bound to the Gβγ subunits and coupled to a GPCR. Ligand binding by the receptor initiates a conformational change that allows the receptor to trigger GDP release from the Gα subunit. Gα will then bind GTP, which is the more abundant nucleotide in the cytoplasm[23]. GTP binding promotes the dissociation of the Gα-GTP and Gβγ subunits, allowing the G-Proteins to interact with and signal through downstream effectors. The Gα subunit has slow, endogenous GTPase activity, and will eventually hydrolyze GTP into GDP, thus turning off the Gα subunit and promoting reformation of the heterotrimer complex. However, the rate of GTP hydrolysis can be greatly enhanced

by Regulators of G-Protein Signaling (RGS) proteins; indeed the rapid G-Protein turnover rates *in vivo* indicate that RGS proteins are required for normal cell physiology[23–25].

Downstream of receptors, neutrophil polarity is largely governed by the Rho-family GTPases and phosphoinositide lipid signaling. The Rho-GTPases, Rac and Cdc42, along with PI3K/PtdIns(3,4,5)P3 are well established cell front polarity regulators that collaborate to drive branched actin formation in the lamellipodium [2,4,17,18,26–30]. At the cell rear, RhoA activity coordinates the formation of contractile actomyosin complexes, while the phosphatase, PTEN, maintains the cell rear associated lipid PtdIns(4,5)P2[17,26,27,31]. Locally, these cell front and rear domains are self-reinforcing via positive feedback, but are mutually antagonistic to enhance asymmetric cell polarization[18].

How GPCR and G-Protein signaling biases and coordinates the downstream polarity circuit remains poorly understood; however, there is growing evidence that role specialization at the heterotrimeric G-Protein level and within the Rho-GTPases cascade is an important feature of the network. To investigate the role of heterotrimeric G-Proteins in chemotaxis signaling, siRNA knockdown of $G_i\alpha$ and Gβ were paired with a high-throughput (HT) chemotaxis assay[32]. The assay combines photo-release of chemoattractant gradients and live cell tracking, enabling measurements of directional accuracy, basal cell speed, and cell speed increases post stimulation (chemokinesis)[32]. The knockdown of $G_i\alpha$ yielded directionality defects for low and high chemoattractant concentrations in the automated HT-chemotaxis assay. Indeed, this directional accuracy phenotype was about as strong as one of the formyl-peptide receptor siRNA conditions. Interestingly, the $G_i\alpha$ KD perturbation also enhanced chemokinesis for both chemoattractant conditions. The consistency of the $G_i\alpha$ KD directionality phenotype across chemoattractant conditions suggests that $G_i\alpha$ plays a specific role in cell steering[32]. In contrast, knock down of Gβ yielded both, a directional accuracy and a chemokinesis defect at the low chemoattractant concentration. However, the high chemoattractant concentration rescued both defects in the Gβ KD condition. These results suggest that Gβ is critical for response sensitivity and amplification; strong receptor activation can compensate for the low Gβ levels, but weak receptor stimulation cannot, causing

the cells to have defects in both steering and movement[32]. PI3K /PIP3 and Rac are downstream effectors of Gβγ, which function with F-actin in a positive feedback loop to promote the cell front[33–37]. The low chemokinesis and poor directional accuracy phenotypes from the Gβ KD experiments suggest that a minimum threshold of Gβγ signaling is required to activate this front-amplifying positive feedback loop. While some molecular connections between the heterotrimeric G-proteins and the polarity cascade have been established, the mechanisms that drive G-protein subunit specificity and function remain an open question [3,33,34,38,39]

While members of the front/rear cell polarity axis are well established, the roles for specific polarity regulators within the cell front are also being defined. Analysis of Rho GTPase activities within chemotaxing neutrophils highlights that each GTPase has differing subcellular spatial activities. Active Rac is localized broadly across the entire cell front with activity peaking 4-5um from the leading edge[4]. Downstream, Rac coordinates the WAVE regulatory complex, which coordinates broad waves of branched F-actin in the cell front[35]. In combination with the positive feedback loop with PI3K/PIP3 and F-actin[33–37], Rac appears poised to broadly maintain lamellipodia and the cell front. In contrast to Rac, peak Cdc42 signaling is tightly associated with the very leading edge, while it's activity was shown to be predictive of cell turning in chemotaxis assays[4]. Additionally, dominant-negative Cdc42 and Cdc42-KO cells had reduced directional accuracy in chemotaxis assays, and the propensity to generate many, short-live protrusions[29,40]. These results indicate that Cdc42 is required for stabilizing the cell front/rear polarity while also positioning Cdc42 as the signal integrator between receptor signals and the polarity pathway for cell steering. Collectively, the Rho-GTPases that control the cell front appear to coordinate different facets of the cell front response.

1.4 The directional accuracy and signal amplification paradox.

In neutrophils, chemotaxis is a spatially accurate behavior, with cells able to measure the difference between chemoattractant gradients that are as shallow as 1% across the length of the cell[20]. The remarkable precision of this behavior is paradoxical; on one hand, the cell needs to preserve the spatial information encoded by receptor signaling while on the other, cell polarization requires signal amplification, which could distort spatial information.

This paradox has long been observed in the field, and a number of conceptual models have been proposed to explain neutrophil directional accuracy[1,2,16,38–42]. One of the leading models is the Local Excitation, Global Inhibition (LEGI) model, which stipulates that receptor activity locally produces a diffusion-restricted excitatory signal as well as a freely diffusible inhibitory signal. Regions of the cell facing the chemoattractant gradient locally produce more excitatory signal than the cell wide inhibition signal, determining the direction for the cell front[1,2,38,39]. In the model, the excitatory and inhibitory signals impinge on the "response regulator", which specifies the directional output of the response. A well-documented limitation of this model is that the identity of the global inhibitor is still unknown[40]. Additionally, testing this hypothesis has been challenging because many components in the cell front polarity circuit could be the response regulator; thus, rejecting the hypothesis must be done on a case-by-case basis.

While these theoretical models have spurred important work in the chemotaxis field, understanding how spatial cues are encoded in the signaling network requires empirical measurements of spatial signal processing. Measuring spatial signal processing in live cells requires high magnification, high resolution microscopy, and control over chemoattractant gradient generation. To overcome these challenges, I collaborated within the Collins Lab to develop an automated, high-resolution microscopy assay for measuring Rho GTPase activity in chemotaxing neutrophils. This method was updated to include Total Internal Reflectance Fluorescence Microscopy (TIRF) and Confocal microscopy, for increased signal to noise data. Additionally, it includes updates for how to use UV light to pattern photo-release of a chemoattractant gradient. A description of this method is included in chapter 2.

Diffusion of small chemoattractant molecules represents an important experimental limitation for measuring spatial signal processing. Locally stimulating a well-defined subset of receptors with a diffusible chemoattractant to measure where downstream signals increase or decrease is experimentally impossible. Overcoming this challenge was a central goal of my dissertation research. To improve spatial and temporal control over chemotaxis signaling, I developed zebrafish parapinopsina, an optogenetic tool that enables local (~1um) and reversible stimulation of chemotaxis behavior with light. Downstream of the parapinopsin receptor, Cdc42 activity was used as the cell polarity readout as it is predictive of cell turning[4]. A complete description of this work to decipher how spatial signal processing functions in neutrophils is described in Chapter 3.

1.5 Polarity feedback to receptors

The cell polarity circuit is capable of spontaneous self-organization and sustained signaling through spatially-segregated feedbacks and mutual antagonism between front and back signaling domains[18,20]. Supporting the stability of the polarity signaling, chemotaxing neutrophils will often U-turn when presented with a new gradient, rather than fully repolarize[43]. Understanding whether this behavior arises because the cell front has greater signal amplification or because the cell rear is insensitive to receptor inputs remains an open question. Like questions regarding spatial processing, differentiating between these two hypotheses is limited by rapid diffusion of chemoattractants, as locally deployed signals will rapidly spread across the cell. To address the question of whether the cell rear is insensitive to receptor inputs, I collaborated with Amalia Hadjitheodorou from the Theriot lab at the University of Washington and the Allen Institute. We paired my optogenetic receptor and red-shifted biosensor with straight channel microfluidic devices to deliver subcellular receptor stimulation at the cell rear in an environment that prevented the cells from U-Turning. The complete description of this work is detailed in chapter 4.

1.6 References

1. Devreotes, P. & Janetopoulos, C. Eukaryotic chemotaxis: distinctions between directional sensing and polarization. *J. Biol. Chem.* **278**, 20445–20448 (2003).

2. Parent, C. A. & Devreotes, P. N. A cell's sense of direction. *Science* **284**, 765–770 (1999).

3. Li, Z. *et al.* Directional sensing requires Gβγ-mediated PAK1 and PIX alpha-dependent activation of Cdc42. *Cell* **114**, 215–27 (2003).

4. Yang, H. W., Collins, S. R. & Meyer, T. Locally excitable Cdc42 signals steer cells during chemotaxis. *Nat Cell Biol* **18**, 191–201 (2016).

5. Wood, W., Faria, C. & Jacinto, A. Distinct mechanisms regulate hemocyte chemotaxis during development and wound healing in Drosophila melanogaster. *J Cell Biol* **173**, 405–416 (2006).

6. Armstrong, P. B. The control of cell motility during embryogenesis. *Cancer Metastasis Rev.* **4**, 59–79 (1985).

7. Reiss, K., Mentlein, R., Sievers, J. & Hartmann, D. Stromal cell-derived factor 1 is secreted by meningeal cells and acts as chemotactic factor on neuronal stem cells of the cerebellar external granular layer. *Neuroscience* **115**, 295–305 (2002).

8. Lyuksyutova, A. I. *et al.* Anterior-posterior guidance of commissural axons by Wnt-frizzled signaling. *Science* **302**, 1984–1988 (2003).

9. Weiskopf, K. *et al.* Myeloid cell origins, differentiation, and clinical implications. *Microbiol. Spectr.* **4**, (2016).

10. Jin, T., Xu, X. & Hereld, D. Chemotaxis, chemokine receptors and human disease. *Cytokine* **44**, 1–8 (2008).

11. Lakshman, R. & Finn, A. Neutrophil disorders and their management. *J Clin Pathol* **54**, 7–19 (2001).

12. Aker, M., Zimran, A., Abrahamov, A., Horowitz, M. & Matzner, Y. Abnormal neutrophil chemotaxis in Gaucher disease. *Br J Haematol* **83**, 187–91 (1993).

13. Hartwig, H., Silvestre Roig, C., Daemen, M., Lutgens, E. & Soehnlein, O. Neutrophils in atherosclerosis. A brief overview. *Hamostaseologie* **35**, 121–7 (2015).

14. Kolaczkowska, E. & Kubes, P. Neutrophil recruitment and function in health and inflammation. *Nat Rev Immunol* **13**, 159–75 (2013).

15. Mazor, R. *et al.* Primed polymorphonuclear leukocytes constitute a possible link between inflammation and oxidative stress in hyperlipidemic patients. *Atherosclerosis* **197**, 937–943 (2008).

16. Devreotes, P. N. *et al.* Excitable Signal Transduction Networks in Directed Cell Migration. *Annu. Rev. Cell Dev. Biol.* **33**, 103–125 (2017).

17. Van Haastert, P. J. M. & Devreotes, P. N. Chemotaxis: Signaling the way forward. *Nat. Rev. Mol. Cell Biol.* **5**, 626–634 (2004).

18. Wang, Y. *et al.* Identifying network motifs that buffer front-to-back signaling in polarized neutrophils. *Cell Rep.* **3**, 1607–1616 (2013).

19. Huang, C.-H., Tang, M., Shi, C., Iglesias, P. A. & Devreotes, P. N. An excitable signal integrator couples to an idling cytoskeletal oscillator to drive cell migration. *Nat Cell Biol* **15**, 1307 (2013).

20. Zigmond, S. H. Ability of polymorphonuclear leukocytes to orient in gradients of chemotactic factors. *J. Cell Biol.* **75**, 606–616 (1977).

21. Weiner, O. D. Regulation of cell polarity during eukaryotic chemotaxis: the chemotactic compass. *Curr. Opin. Cell Biol.* **14**, 196–202 (2002).

22. Xu, J. *et al.* Divergent signals and cytoskeletal assemblies regulate self-organizing polarity in neutrophils. *Cell* **114**, 201–14 (2003).

23. Kamp, M. E., Liu, Y. & Kortholt, A. Function and Regulation of Heterotrimeric G Proteins during Chemotaxis. *Int. J. Mol. Sci.* **17**, 90 (2016).

24. Arshavsky, V. Y. & Pugh Jr, E. N. Lifetime Regulation of G Protein–Effector Complex: Emerging Importance of RGS Proteins. *Neuron* **20**, 11–14 (1998).

25. Koelle, M. R. A new family of G-protein regulators—the RGS proteins. *Curr. Opin. Cell Biol.* **9**, 143–147 (1997).

26. Hind, L. E., Vincent, W. J. & Huttenlocher, A. Leading from the Back: The Role of the Uropod in Neutrophil Polarization and Migration. *Dev. Cell* **38**, 161–9 (2016).

27. Bagorda, A. & Parent, C. A. Eukaryotic chemotaxis at a glance. *J. Cell Sci.* **121**, 2621–2624 (2008).

28. Weiner, O. D. *et al.* A PtdInsP 3 - and Rho GTPase-mediated positive feedback loop regulates neutrophil polarity. *Nat. Cell Biol.* **4**, 509–513 (2002).

29. Srinivasan, S. *et al.* Rac and Cdc42 play distinct roles in regulating PI(3,4,5)P3 and polarity during neutrophil chemotaxis. *J Cell Biol* **160**, 375–85 (2003).

30. Servant, G. *et al.* Polarization of Chemoattractant Receptor Signaling During Neutrophil Chemotaxis. *Science* **287**, 1037–1040 (2000).

31. Iijima, M. & Devreotes, P. Tumor Suppressor PTEN Mediates Sensing of Chemoattractant Gradients. *Cell* **109**, 599–610 (2002).

32. Collins, S. R. *et al.* Using light to shape chemical gradients for parallel and automated analysis of chemotaxis. *Mol. Syst. Biol.* **11**, 804 (2015).

33. Stephens, L. *et al.* A novel phosphoinositide 3 kinase activity in myeloid-derived cells is activated by G protein βγ subunits. *Cell* **77**, 83–93 (1994).

34. Welch, H. C. *et al.* P-Rex1, a PtdIns (3, 4, 5) P 3-and Gβγ-regulated guanine-nucleotide exchange factor for Rac. *Cell* **108**, 809–821 (2002).

35. Weiner, O. D. *et al.* Hem-1 complexes are essential for Rac activation, actin polymerization, and myosin regulation during neutrophil chemotaxis. *PLOS Biol.* **4**, e38 (2006).

36. Inoue, T. & Meyer, T. Synthetic activation of endogenous PI3K and Rac identifies an AND-gate switch for cell polarization and migration. *PLoS One* **3**, e3068 (2008).

37. Van Keymeulen, A. *et al.* To stabilize neutrophil polarity, PIP3 and Cdc42 augment RhoA activity at the back as well as signals at the front. *J. Cell Biol.* **174**, 437–445 (2006).

38. Kamakura, S. *et al.* The Cell Polarity Protein mInsc Regulates Neutrophil Chemotaxis via a Noncanonical G Protein Signaling Pathway. *Dev. Cell* **26**, 292–302 (2013).

39. Hawkins, P. T., Stephens, L. R., Suire, S. & Wilson, M. PI3K signaling in neutrophils. in *Phosphoinositide 3-kinase in Health and Disease* 183–202 (Springer, 2011).

40. Szczur, K., Zheng, Y. & Filippi, M.-D. The small Rho GTPase Cdc42 regulates neutrophil polarity via CD11b integrin signaling. *Blood* **114**, 4527–4537 (2009).

41. Devreotes, P. N. & Zigmond, S. H. Chemotaxis in Eukaryotic Cells: A Focus on Leukocytes and Dictyostelium. *Annu. Rev. Cell Biol.* **4**, 649–686 (1988).

42. Xiong, Y., Huang, C. H., Iglesias, P. A. & Devreotes, P. N. Cells navigate with a local-excitation, global-inhibition-biased excitable network. *Proc. Natl. Acad. Sci. U. S. A.* **107**, 17079–86 (2010).

43. Jilkine, A. & Edelstein-Keshet, L. A comparison of mathematical models for polarization of single eukaryotic cells in response to guided cues. *PLoS Comput Biol* **7**, e1001121 (2011).

44. Mori, Y., Jilkine, A. & Edelstein-Keshet, L. Wave-Pinning and Cell Polarity from a Bistable Reaction-Diffusion System. *Biophys J* **94**, 3684–3697 (2008).

45. Levchenko, A. & Iglesias, P. A. Models of Eukaryotic Gradient Sensing: Application to Chemotaxis of Amoebae and Neutrophils. *Biophys J* **82**, 50–63 (2002).

46. Iijima, M., Huang, Y. E. & Devreotes, P. Temporal and Spatial Regulation of Chemotaxis. *Dev. Cell* **3**, 469–478 (2002).

Chapter 2

Parallel high resolution imaging of leukocyte chemotaxis under agarose with Rho family GTPase biosensors

George R. R. Bell[#], Dean E. Natwick[#], and Sean R. Collins*

[1]Department of Microbiology and Molecular Genetics, University of California, Davis, Davis, CA 95616, United States

[#] These authors contributed equally.

2.1 Preface

This method was originally published as a chapter in the "Rho GTPases: Methods and Protocols" from the "Methods in Molecular Biology" book series. Due to copyright restrictions, I was unable to reprint the method in this dissertation. Instead, please refer to the citation to access the book chapter. The summary below covers general details and the experimental advantages that this technique provides.

2.2 Citation

Bell, G. R. R., Natwick, D. E. & Collins, S. R. Parallel high-resolution imaging of leukocyte chemotaxis under agarose with Rho-family GTPase biosensors. in *Rho GTPases: Methods and Protocols* (ed. Rivero, F.) 71–85 (Springer, 2018).

2.3 Author contributions

G.R.R.B. and D.E.N. contributed equally to this work. G.R.R.B. and D.E.N. developed the cell culture and under agarose protocols. Additionally, G.R.R.B. and D.E.N. with advice from S.R.C. developed the TIRF microscopy imaging protocols for no-stimulated assays, uniform stimulation assays, and gradient stimulation assays. S.R.C. provided inspiration for the project as well as contributed the image processing sections that detail cell segmentation and alignment as well as ratiometric FRET analysis. G.R.R.B. D.E.N. and S.R.C. contributed to writing the manuscript.

2.4 Summary

Neutrophils are professional chemotactic cells of the innate immune system that follow chemical cues from the bloodstream to sites of inflammation or infection. During chemotaxis, chemoattractant cues are captured by G-Protein Coupled Receptors, which signal to the downstream cell polarity network[1–3]. Rho-family GTPases are critical regulators of this cell polarity signaling cascade. Their activity patterns within the cell define the front/rear polarity axis and they coordinate the formation of branched actin in the cell front and contractile acto-myosin in the cell rear to morphologically polarize the cell[4,5]. The regulation of the Rho GTPases is complex, including interconnected positive and negative feedback loops and inputs from receptors, yet much of the wiring remains poorly described[6–8]. Importantly, the spatial activity patterns of these GTPases are highly dynamic and are capable of changing on short timescales as the cells move and respond to stimuli [9,10]. Thus, deciphering the roles and coordination of these GTPases in chemotaxis requires tools for monitoring GTPase activity with high spatiotemporal resolution under reproducible chemoattractant stimulation conditions.

To measure Rho GTPase activity in chemotaxing neutrophil-like cells, we developed an under-agarose cell migration assay that is compatible with photo-activation of chemoattractant gradients and high-resolution imaging of Rho GTPase FRET biosensors. This assay design offers several experimental benefits. First, this method was optimized to use glass-bottomed 96-well plates to increase experimental throughput. Second, cells are plated between the glass-bottom of the imaging plate and the layer of agarose, constraining the cell movement to 2D, and simplifying cell tracking via image processing. Depending on experimental goals, this assay is compatible with high magnification (60x) imaging using epifluorescence, Total Internal Reflectance Fluorescence (TIRF) and confocal microscopy. Neutrophils move using low-adhesion, amoeboid motility and can migrate through dense tissues in vivo[11,12]. The under-agarose plating strategy confines cells and provides an optimal environment for amoeboid motility[13]. To gain control over chemoattractant gradient formation, UV-sensitive caged chemoattractants including N-nitroveratryl-N-formyl-methionine-leucine-phenylalanine (Nv-fMLF)[14], can be mixed with the agarose prior to plating. The caged chemoattractants enable user-controlled, photo-release and maintenance of chemoattractant gradients at physiologic concentrations. Finally, the under-agarose assay can be combined with cells stably expressing FRET biosensors for the Rho-family GTPases to measure spatial and temporal GTPase activity patters in cells responding to chemoattractant gradients.

2.5 References

1. Chen, L. *et al.* Two phases of actin polymerization display different dependencies on PI(3,4,5)P3 accumulation and have unique roles during chemotaxis. *Mol. Biol. Cell* **14**, 5028–5037 (2003).

2. Parent, C. A. & Devreotes, P. N. A cell's sense of direction. *Science* **284**, 765–770 (1999).

3. Devreotes, P. & Janetopoulos, C. Eukaryotic chemotaxis: distinctions between directional sensing and polarization. *J. Biol. Chem.* **278**, 20445–20448 (2003).

4. Ridley, A. J. *et al.* Cell Migration: Integrating Signals from Front to Back. *Science* **302**, 1704–1709 (2003).

5. Nobes, C. D. & Hall, A. Rho, Rac, and Cdc42 GTPases regulate the assembly of multimolecular focal complexes associated with actin stress fibers, lamellipodia, and filopodia. *Cell* **81**, 53–62 (1995).

6. Xu, J. *et al.* Divergent signals and cytoskeletal assemblies regulate self-organizing polarity in neutrophils. *Cell* **114**, 201–214 (2003).

7. Guilluy, C., Garcia-Mata, R. & Burridge, K. Rho protein crosstalk: Another social network? *Trends Cell Biol.* **21**, 718–726 (2011).

8. Hanna, S. & El-Sibai, M. Signaling networks of Rho GTPases in cell motility. *Cell. Signal.* **25**, 1955–1961 (2013).

9. Machacek, M. *et al.* Coordination of Rho GTPase activities during cell protrusion. *Nature* **461**, 99–103 (2009).

10. Yang, H. W., Collins, S. R. & Meyer, T. Locally excitable Cdc42 signals steer cells during chemotaxis. *Nat. Cell Biol.* **18**, 191–201 (2016).

11. Lämmermann, T. *et al.* Rapid leukocyte migration by integrin-independent flowing and squeezing. *Nature* **453**, 51–55 (2008).

12. Lam, P. Y. & Huttenlocher, A. Interstitial leukocyte migration in vivo. *Curr. Opin. Cell Biol.* **25**, 650–658 (2013).

13. Collins, S. R. *et al.* Using light to shape chemical gradients for parallel and automated analysis of chemotaxis. *Mol. Syst. Biol.* **11**, 804 (2015).

14. Pirrung, M. C., Drabik, S. J., Ahamed, J. & Ali, H. Caged chemotactic peptides. *Bioconjug. Chem.* **11**, 679–681 (2000).

Chapter 3

Optogenetic control of receptors reveals distinct roles for actin- and Cdc42-dependent negative signals in chemotactic signal processing

George R. R. Bell[1], Esther Rincón[1], Emel Akdoğan [1], and Sean R. Collins[1]*.

[1]Department of Microbiology and Molecular Genetics, University of California, Davis, Davis, CA 95616, United States

3.1 Preface

This chapter represents the primary research output for this dissertation, and includes unpublished work that is currently under review for publication. The manuscript for this chapter was written in the letter format and thus does not have subsections in the main text. The manuscript from this chapter and the subsequent chapter were co-submitted as affiliated manuscripts.

3.2 Citation

Bell, G. R. R., Rincón, E., Akdoğan, E. & Collins, S. R. Optogenetic control of receptors reveals distinct roles for actin- and Cdc42-dependent negative signals in chemotactic signal processing. *bioRxiv* 2021.04.03.438340 (2021) doi:10.1101/2021.04.03.438340.

3.3 Author Contributions

G.R.R.B and S.R.C conceived of the project. G.R.R.B constructed the parapinopsina and TomKat control cell lines and optimized the parapinopsina system. E.R.G. generated the Cdc42-KO clonal cell line, while E.A. created Cdc42-KO lines expressing parapinopsina and the TomKat FRET sensor. G.R.R.B conducted the experiments and performed the data analysis with guidance from S.R.C.. G.R.R.B and S.R.C. interpreted the results and wrote the manuscript. All authors have read and edited the manuscript.

3.4 Main Text

During chemotaxis, neutrophils use cell surface G-Protein Coupled Receptors (GPCRs) to detect chemoattractant gradients[1–4]. The downstream signaling system is wired with multiple feedback loops that amplify weak inputs and promote spatial separation of cell front and rear activities[1,5–8]. Positive feedback could promote rapid signal spreading[9], yet information from the receptors is transmitted with high spatial fidelity, enabling detection of small differences in chemoattractant concentration across the cell[1]. How the signal transduction network achieves signal amplification while preserving spatial information remains unclear. The GTPase Cdc42 is a cell-front polarity coordinator that is predictive of cell turning, suggesting an important role in spatial processing[10]. To directly measure information flow from receptors to Cdc42, we paired zebrafish parapinopsina, an optogenetic GPCR that allows reversible ON/OFF receptor control with a spectrally compatible red/far red Cdc42 FRET biosensor. Using this new toolkit, we show that positive and negative signals downstream of G-proteins shape a rapid, dose-dependent Cdc42 response. Furthermore, F-actin and Cdc42 itself provide two distinct negative signals that limit the duration and spatial spread of Cdc42 activation, maintaining output signals local to the originating receptors.

In leukocytes, chemotaxis is driven almost exclusively by GPCRs coupling to the $G_i\alpha$-family of G-proteins[1–4]. Through partially understood pathways, these receptors trigger activation of polarity and

motility signaling driven by Rho-family GTPases, phospholipid signaling, and different actin assemblies. Rac, Cdc42, phosphatidylinositol (3,4,5)-trisphosphate (PIP3), and branched actin coordinate the cell front while RhoA and contractile actomyosin complexes define the cell rear[1,5–8]. Accurate cell steering requires that the polarity programs receive and rapidly incorporate directional cues from receptors, enabling responses to differences in input strength across the cell. Prior studies indicate that receptors are uniformly distributed on the plasma membrane[11,12], and in *Dictyostelium discoideum* amoeba chemotaxis, G-protein activity largely mirrors receptor binding[4], suggesting that spatial processing occurs downstream. In neutrophils, Cdc42 likely plays a key role in this process, as it stabilizes cell front/rear polarity, and asymmetry in its activity is predictive of cell turning[10,13,14].

Signal processing in chemotaxis balances two potentially competing challenges. It must amplify signals using positive feedback to polarize cells with asymmetric protein activities, but it must also retain information about receptor status locally. Positive feedback could quickly distort spatial information, as it is capable of generating activity waves that can propagate faster than diffusion[9]. Indeed, Cdc42 activity can form traveling waves in neutrophil-like cells when actin is depolymerized[10]. Thus, many models for directional sensing in chemotaxis involve balancing of positive and negative feedback or feedforward loops that collaborate to restrict, but also amplify receptor-derived signals[2,3,5]. Nevertheless, the negative signaling mechanisms helping to maintain spatial information remain unclear.

We aimed to determine how inputs are processed downstream of receptors, including how signals spread spatially. Making these measurements requires sharply localized receptor activation, which would be very difficult to achieve with native attractants due to their rapid diffusion. Therefore, we developed parapinopsina, a nonvisual opsin GPCR, as an optogenetic tool that enables local (~1 μm) and reversible stimulation of chemotaxis behavior through activation of $G_i\alpha$-family G-proteins. UV light activates parapinopsina by photo-isomerizing its 9-*cis*-retinal cofactor to *trans*-retinal, while green light (> 530 nm) inactivates the receptor and regenerates 9-*cis*-retinal[15,16], allowing rapid activation and deactivation cycles (Fig. 1a). Previously, OPN1SW (human blue cone opsin) and lamprey paparinopsina were shown to elicit a chemotactic-like response in mouse macrophage RAW 264.7 cells, supporting the use of optogenetic

GPCRs to drive chemotaxis-like responses[17,18]. In a sister article, we used the parapinopsina optogenetic tool to investigate overwriting cell front-rear polarity in neutrophils migrating in 1-D microfluidic channels, further demonstrating its usefulness for investigating complex signaling cascades[19].

To measure Cdc42 signaling downstream of parapinopsina in single cells, we modified an existing Cdc42 FRET biosensor[20] to use a novel td-Tomato/td-Katushka2 (TomKat) FRET pair that is compatible with UV parapinopsina stimulation (Fig. 1b). Small GTPases are activated by guanine nucleotide exchange factors (GEFs) that catalyze GDP to GTP exchange, and inactivated by GTPase-activating proteins (GAPs) that promote GTP hydrolysis[21]. Importantly, this TomKat FRET sensor is localized to the plasma membrane and reports on the local balance of GEF and GAP activity regulating Cdc42 (Fig. 1b). We validated the TomKat FRET sensor by comparing its spatial activity pattern to that of the original CFP/YFP Cdc42 FRET sensor in randomly migrating neutrophil-like cells (differentiated PLB-985 cells). Both sensors reported very similar spatial activity (Fig. 1c). Although the dynamic range for the TomKat sensor (~11%) is less than that of the CFP/YFP sensor (~56%), the TomKat sensor brightness still enables collection of high signal-to-noise data.

We next tested whether we could measure changes in Cdc42 activity downstream of parapinopsina, and sought to verify wavelength-dependent, reversible control of the receptor. In a population of cells, we monitored Cdc42 activity and applied a global, 100 second stimulation period in which we delivered pulses of UV light immediately after acquiring each FRET image. Stimulation triggered a rapid Cdc42 response that peaked in less than 20 seconds and remained elevated while UV light was applied. Once the UV stimulation ceased, the response attenuated immediately, consistent with long wavelength illumination inactivating receptors (Fig. 1d and Supplementary Video 1). Importantly, the response was dependent on UV-light stimulation, and exogenous 9-*cis* retinal.

We also verified that the receptor directed cell migration by stimulating a small (~1-4 μm) region of the cell edge using a ~2 μW spot of 407 nm light while recording Cdc42 activity. Local activation triggered cell repolarization and migration in the direction of stimulation (Fig. 1e and Supplementary Video 2). In optogenetically driven cells, Cdc42 activity was high at the leading edge, and decreased

towards the cell rear, consistent with the spatial pattern observed in chemotaxing PLB-985 cells[10]. Collectively, these results demonstrate that we can optically activate parapinopsina to drive directed cell migration while recording spatial and temporal activity of Cdc42 using the spectrally compatible TomKat FRET sensor.

Many models for directional sensing and polarization involve integration of positive and negative signals downstream of receptors[3,22,23]. Therefore, we investigated whether both types of regulation act on Cdc42, by characterizing the temporal dynamics of receptor-initiated Cdc42 responses. (Fig. 2a). Using the global stimulation assay, we delivered a single stimulating light pulse to a population of cells, titrating the light stimulus strength. In all cases, the Cdc42 activity rapidly increased, peaked, and then attenuated, overshooting the pre-stimulus baseline within about 10 seconds (Fig. 2b and Supplementary Fig. 1a and Supplementary Video 3). The response eventually recovered from the negative overshoot, returning to a level near the pre-stimulus baseline after ~2 min for the highest intensity stimulation (Supplementary Fig. 1b). Both the positive and negative phases of the response were dose dependent. Cdc42 is rapidly activated downstream of receptors, but this activation is countered by a slower, longer lasting negative regulation.

The fact that the Cdc42 response was tunable (Fig. 2b) was intriguing since the chemotaxis signaling network is known to contain positive feedback loops that amplify responses, promote polarity, and contribute to "excitable" system behaviors, which can include all-or-nothing responses, refractory periods, and propagating waves of activity[7,24,25]. Cdc42 is regulated by positive feedback through PAK1[26] and its activity generates traveling waves when the actin cytoskeleton is depolymerized[10], indicating some excitable systems features. To verify that the Cdc42 response is tunable, despite positive feedbacks, we analyzed the same experiments at the single cell level, where cell-to-cell variability could not obscure all-or-nothing behavior. For each cell, we measured the response amplitude, relative to baseline, at the typical peak response time (Fig. 2c,d); as a control we performed the same analysis using a pre-stimulus time window (Supplementary Fig. 1c). We found that for intermediate stimulus levels, most cells responded with intermediate response amplitudes, indicating that the response was titratable at the single-

cell level (Fig. 2d). While this contrasts with earlier observations of switch-like behavior for PIP3 responses in HL-60 cells[27], the different roles of Cdc42 and PIP3 at the cell front may require alternate regulation mechanisms. Additionally, our system provides very precise control of stimulus intensity and timing, resolving differences in responses that peak within 10 seconds.

Leveraging precise control of cell stimulation, we used two-pulse and prolonged stimulation protocols to understand how the cells integrate signals temporally, potentially revealing adaptive behavior or other features of negative regulation. By applying two, pulse stimulations with varying time delays, we found that responses to sequential stimuli were largely independent. Closely spaced inputs added to produce larger responses, with no obvious refractory behavior (Fig. 2e,f and Supplementary Fig. 2). Interestingly, this result differs from Ras activation in Latrunculin-A treated *Dictyostelium* cells and PIP3 in HL-60 cells where a refractory period was observed[27,28]. The lack of a refractory period suggests that the Cdc42 circuit can rapidly respond to new inputs, a feature likely important for responding dynamically to pathogen cues and navigating complex environments. Next, we applied prolonged stimulations to investigate potential adaptive behavior. In response to prolonged low-power stimulus, the Cdc42 response gradually increased (dependent on continued input), until it reached a plateau at about 20 seconds, and then only slightly attenuating until the stimulation was removed (Fig. 2g). In contrast, a stronger prolonged stimulus caused a response that rapidly peaked, and then quickly began to attenuate. However, the rapid attenuation did not cause adaptation, but gave way to a shoulder phase with slower attenuation until the stimulation ceased (Fig. 2h). These experiments reinforce that the Cdc42 response is graded based on receptor input strength, but they also suggest complex, multi-tiered negative regulation of the circuit with differential kinetics.

Ultimately, we wanted to connect features of receptor-mediated Cdc42 signaling dynamics with molecular components to understand signal processing. Since Cdc42 activity is regulated by multiple feedback connections[13,26,29], we reasoned that this feedback may play an important role in shaping Cdc42 dynamics. To test this, we generated a clonal, homozygous Cdc42 knockout (Cdc42-KO) cell line using CRISPR/Cas9 ribonucleoprotein complexes targeted to excise a ~100 bp region of exon 4. We validated

the knockout using amplicon sequencing (Supplementary Fig. 3a) and western blot (Fig. 3a and Supplementary Fig. 3b). To examine the loss of feedback at the cellular level, we assessed Cdc42-KO cells for migration and polarity defects (Fig. 3b-g). Qualitatively, Cdc42-KO cells migrated randomly and tended to make multiple cell fronts that were less stable than the controls cells (Fig. 3e,f and Supplementary Video 4). Furthermore, we observed reduced migratory persistence in randomly migrating Cdc42KO cells compared to control, as evident in downward curvature of a mean square displacement plot (Fig. 3b), and in the faster decay of directionality of migrating cells (Fig. 3c). The multiple cell front behavior and poor migratory persistence are consistent with observations from HL-60 cells expressing dominant-negative Cdc42[13] and Cdc42-null mouse neutrophils[14]. Additionally, we noticed that many Cdc42-KO cells formed cell fronts that pulled away from the cell body, stretching out thin cytoplasmic tethers (Fig. 3g and Supplementary Video 5). Quantifying this behavior, we found that ~40% of Cdc42-KO cells formed cytoplasmic tethers compared to about 4% of control cells (Fig. 3d). Tethers observed in control cells were also typically much shorter and thicker than in the Cdc42-KO line. Interestingly, inhibition of myosin-II with blebbistatin can cause cytoplasmic tethers in HL-60 cells[3], and local Cdc42 activation can induce a long-distance myosin response[29]. Collectively, these findings suggest that Cdc42 cell front activity may mediate long-range regulation of protrusion-inhibiting, cell rear polarity signals.

Next, we probed the components and signaling processes that shape the Cdc42 response using drug perturbations and the Cdc42-KO cell line, with particular interest in the complex negative regulation. First, we investigated whether negative regulation involves heterotrimeric G-protein independent mechanisms, as documented in *Dictyostelium* amoeba[27] (Fig. 4a). We used pertussis toxin (PTX) to inhibit $G_i\alpha$ family G-protein signaling and asked whether the negative phase of the Cdc42 response was left intact. Instead, we found that PTX dramatically suppressed both the positive and negative phases, indicating that both are dependent on $G_i\alpha$ family G-proteins (Fig. 4b,c).

Next, we sought to verify that we could detect changes in the Cdc42 response due to specific perturbations downstream of the receptor and G-proteins. Since PAK1 kinase amplifies Cdc42 signaling through a positive feedback loop,[26] we reasoned that inhibition of PAK1 would result in a lower Cdc42

response magnitude. As expected, PAK1 inhibition with IPA-3 reduced the Cdc42 response overall (Fig. 4d and Supplementary Fig. 4a). Importantly, the kinetic profile shape was largely the same, indicating that we can detect alterations in the Cdc42 response that are due to specific disruptions in the signaling pathway.

We then investigated Cdc42-dependent feedback using the Cdc42-KO background. We hypothesized that if a Cdc42-dependent feedback was the primary pathway controlling signal attenuation, then it should be disrupted by loss of endogenous Cdc42. Since the Cdc42 TomKat sensor monitors the balance of regulating GEF and GAP activities, we expected its signal to remain elevated after stimulation. Instead, we observed more complex dynamics indicating multiple regulatory pathways. With a strong stimulus, the Cdc42-KO response magnitude was reduced as with PAK1 inhibition (Fig. 4d), suggesting that the Cdc42-dependent positive feedback loop was impaired. However, the attenuation dynamics were also slower and lacked the initial fast phase (Fig. 4e). Further supporting an important role for negative feedback, the Cdc42-KO response magnitude was double that of the control in response to a weaker stimulus (Fig. 4f). Interestingly, the post-stimulation attenuation phase of the response was unaltered by the knockout. Collectively, these results indicate that Cdc42 activity is negatively regulated by Cdc42-dependent feedback and by Cdc42-independent mechanisms.

We reasoned that actin assembly could be a second negative regulator, as it is known to feed back to polarity signaling through membrane and cortical tension. Growing protrusions increase tension, which globally limits actin polymerization and Rac activity[30,31]. To test this, we treated cells with Latrunculin-A to depolymerize F-actin. We found that the Cdc42 response dynamics retained fast and slow attenuation phases in response to prolonged stimulation. However, the amplitude was increased, the initial attenuation phase was slightly slower, and the post-stimulation negative response was faster and stronger (Fig. 4g). These differences were more obvious in pulse stimulation experiments (Fig. 4h). These results suggest that rapid, actin-dependent signaling limits Cdc42 responses, but that other major negative signals are independent of F-actin and membrane tension. The larger overshoot in the presence of Latrunculin-A suggests that other negative regulators are activated more strongly when the actin-

dependent signal is absent. Finally, we treated Cdc42-KO cells with Latrunctulin-A to determine if both were functioning in the same pathway. The response combined features of both perturbations, resulting in slower signal attenuation than with either alone (Fig 4i). These results suggest that F-actin and Cdc42-dependent feedback mechanisms provide two distinct negative signals regulating Cdc42.

These two negative regulators emerged as likely candidates for spatially constraining the spread of signaling downstream of receptor inputs. To test this, we developed a total internal reflection fluorescence (TIRF) microscopy assay to directly measure spatial signal processing in the basal plasma membrane. We automated cell identification and delivery of either one or five, low powered micron-scale, stimulus pulses to the cell center and followed the response over time (Fig. 5a and Supplementary Video 6). Qualitatively, the response was rapid, but did not spread across the whole cell (Fig. 5a,b). We quantified this by measuring the mean change in FRET ratio as a function of distance from the stimulation site (Fig. 5c). To simplify our analysis, we analyzed only non-polarized and slow-moving cells. In control cells, the Cdc42 response to a single local stimulus rapidly peaked (3.8 s) and began attenuating, returning to the pre-stimulus baseline at ~10 s (Fig. 5d and Supplementary Fig. 5a-b). Notably, the response did not spread across the whole cell, remaining nearly constant in regions distal (> 6 μm) to the stimulation site. However, the results were different for Cdc42-KO and Latrunculin-A-treated cells. Immediately after stimulation (0.8 s), all three conditions were indistinguishable, indicating that the profile of receptor activation was the same (Fig. 5e). In contrast, Cdc42-KO and Latrunculin-A-treated cells had larger, prolonged responses that extended more than 8 μm from the stimulation site at the response peak (Fig. 5f, Supplementary Fig. 5c-e). Because the single pulse stimulation experiment is transient, we asked whether the Cdc42 circuit could restrict information spread in the context of prolonged (5-pulse) stimulation. While the control Cdc42 response was still locally restricted near the stimulation site (Fig. 5g), the signal spreading in the Latrunculin-A condition was enhanced, highlighting the requirement for F-actin for proper spatial signal processing (Fig. 5h). Collectively, these results suggest that the Cdc42 circuit is organized to spatially restrict the spread of information from the receptor, while rapid response attenuation limits the duration of the signaling event.

Some models of directional sensing propose that signaling outputs are spatially restricted through integration of local positive and cell-wide inhibitory signals generated by receptor engagement[6,22,32]. These models would predict that Cdc42 activity should decrease distal from the stimulation site. However, we did not observe such negative responses (Fig. 5d,g and Supplementary Fig. 5b). These results suggest that, at least on short time scales (~12 s), regulation of Cdc42 downstream of receptors occurs locally.

How spatial information encoded by the chemotaxis receptors is processed by the signal transduction network has remained a longstanding open question. Using a new optogenetic molecular toolkit that enables precise measurements, we show that the Cdc42 signaling circuit is optimized to limit the duration and spatial spread of responses downstream of the receptor. Loss of either F-actin or Cdc42-dependent feedback loops were sufficient to disrupt the response's short and local, spatiotemporal span. In particular, the rapid negative regulation from F-actin was surprising, as F-actin also participates in a positive feedback loop with Rac and PIP3[33–35]. The negative regulation could depend on a number of GAPs that interact with F-actin[36]. GAPs often have complex regulation that require multiple signaling inputs; thus, actin binding could play a role in GAP activation or positioning[21,36]. More generally, our results demonstrate that GAP activity, in addition to GEF activity, is actively regulated downstream of receptor activation, and that multiple negative signals cooperate to coordinate the Cdc42 response (Fig. 5i). Of particular interest are the unidentified GAPs and regulatory mechanisms that respond quickly after receptor activation to attenuate and restrict responses. Finally, the Cdc42-KO phenotypes for both maintenance of cell-wide polarization and local preservation of information downstream of receptor inputs contributes to a growing body of evidence that Cdc42 plays a central role in integrating directional inputs with the cell polarity cascade.

3.5 Acknowledgements

The authors would like to thank Amalia Hadjitheodorou for insightful discussions of image analysis methodologies as well as edits to the manuscript. Additionally, we thank members of the Collins lab for support, especially Dean Natwick, Kwabena Badu-Nkansah, and Sam Hayes for thoughtful manuscript edits and discussions. Finally, G.R.R.B. thanks his thesis committee, Dr. Lesilee Rose and Dr. Edward Pugh, for thoughtful discussion and guidance. This work was supported by an NIH Director's New Innovator Award (DP2HD094656) to S.R.C. G.R.R.B would like to thank the National Science Foundation Graduate Research Fellowship (Grant Number 1650042) for support.

3.6 Author Contributions

G.R.R.B and S.R.C conceived of the project. G.R.R.B constructed the parapinopsina and TomKat control cell lines and optimized the parapinopsina system. E.R.G. generated the Cdc42-KO clonal cell line, while E.A. created Cdc42-KO lines expressing parapinopsina and the TomKat FRET sensor. G.R.R.B conducted the experiments and performed the data analysis with guidance from S.R.C. G.R.R.B and S.R.C. interpreted the results and wrote the manuscript. All authors have read and edited the manuscript.

3.7 Methods

Reagents. This study used Latrunculin-A at a final concentration of 1 µM (Calbiochem Cat# 428021), the PAK1 kinase inhibitor, IPA-3 (5 µM final concentration, Cayman Chemical Cat# 14759), and pertussis toxin (600 ng/ml final concentration, Invitrogen Cat# PHZ1174). Latrunculin-A and IPA-3 were reconstituted in Dimethyl Sulfoxide (DMSO), while the pertussis toxin was diluted in sterile, distilled water.

Cloning. A human codon-optimized version of the zebrafish parapinopsina gene was printed using the Thermofisher Gene Art service in a pUC57 bacterial expression plasmid. The Gene Art product also

contained the prolactin signal sequence peptide on the N-terminus of the parapinopsina gene to enhance protein expression on the cell membrane[37,38]. Using Gibson cloning, the prolactin-parapinopsin construct was C-terminally tagged with mCitrine and inserted into a lentiviral vector.

The Cdc42 TomKat FRET sensor was created by modifying the previously described CFP/YFP Cdc42 FRET sensor[20]. Using a combination of traditional restriction and Gibson cloning, the fluorescent proteins from the original sensor were removed and replaced with td-Tomato as the FRET donor and td-Katushka2 as the FRET acceptor. td-Katushka2 was a gift from Michael Davidson (Addgene # 56049)[39]. All plasmids and plasmid maps will be made available on Addgene for the published version of this manuscript.

Cell culture. PLB-985 cells were cultured in RPMI 1640 (Gibco) complete media as previously described[40]. Cells were differentiated into a neutrophil-like state by culturing 2 x 10^5 cells per ml in RPMI 1640 with 4.5-5% heat-inactivated FBS, 100 mg/ml streptomycin/ 100 U/ml penicillin (P/S), 1.3% DMSO, and 2% Nutridoma-CS (Roche) for 6 days[40]. HEK-293T (ATCC CRL-11268) were used for lentiviral production. Cells were cultured in high glucose DMEM (Sigma-Aldrich, D5671) that was supplemented with 10% heat-inactivated FBS, 1% Glutamax and 100 mg/ml streptomycin/ 100 U/ml penicillin (P/S). All cell lines were maintained in an incubator at 37 °C and 5% CO2. For imaging experiments, a modified "L-15 imaging media" (Leibovitz's L-15 media lacking dye, riboflavin, and folic acid (UC Davis Biological Media Services) was used to minimize media autofluorescence. Cell lines were tested prior to disposal for mycoplasma to confirm the lack of contamination. We note that the PLB-985 cell line is known to be a misidentified cell line that is actually a sub-line of HL-60 cells. We have confirmed this for our own PLB-985 cells by analysis of SNPs[40], and through short tandem repeat (STR) profiling by the ATCC. We chose to use this sub-line rather than HL-60 because we observed better migration in under agarose conditions, although the behavior of the two lines is very similar.

Cell line construction. The Cdc42-TomKat FRET sensor plasmid contains the Inverted Terminal Repeats (ITR) of the piggybac transposon system[41]. To create a stable cell line, the Cdc42-TomKat FRET sensor plasmid was co-electroporated at a 1:1 ratio with the piggybac transposase expression plasmid. Electroporation was achieved with the Neon electroporation system (Sigma-Aldrich). 2 x 10^6 cells were resuspended in the R-buffer from the kit, then 5 µg of each plasmid were added to the cells. Cells were electroporated in the 100 µL pipettes provided in the kit at 1350 V for 35 ms.

The parapinopsina construct was then stably integrated into PLB-985 cells expressing the Cdc42-TomKat sensor using 2nd generation lentivirus. To produce the virus, HEK-293T cells were co-transfected with envelope, packaging and transfer plasmids using Mirus TransIT-2020 (Cat# MIR 5404) transfection reagent. The following ratio of plasmids was used to transfect 1 well on a P6 plate: 0.64 µg Envelope: 1.26 µg Packaging: 1.93 µg Transfer.

Cdc42-KO cells were created by electroporating CRISPR-Cas9 Ribonucleoprotein (RNP) complexes into the PLB-985 cell line. A pair of CRISPR guides targeting a 102 bp region of Cdc42's exon 4 were designed and purchased from Synthego as part of their Gene Knockout Kit v2. Guide 1 had a sequence of 5'-TTTCTTTTTTCTAGGGCAAG while Guide 2 was 5'-ATTTGAAAACGTGAAAGAAA. Purified Cas9 protein was purchased from the QB3 MacroLab at UC Berkeley. To generate the RNPs, a solution containing 180 pmoles of the Synthego guide mixture and 5 µM Cas9 diluted in the Neon R-buffer was incubated at 37 °C for 10 min then stored at RT. Electroporation was conducted using a suspended-drop electroporation device as described[42]. For this device, a maximum volume of 10 µL is electroporated per well on a P96-well plate. Cells (3 x 10^5) were resuspended in 5 µL of Mirus Ingenio electroporation buffer (MIR 50111), mixed with 5 µL of RNP solution, and then electroporated at 120 V for 9 ms. Cells were allowed to recover in RPMI complete media with 20% heat-inactivated FBS for 1 week. To check heterogeneous knock out efficiency, genomic DNA (gDNA) was harvested, and PCR was used to amplify a fragment that covered 300 bp upstream and downstream of the CRISPR guides. This PCR fragment was sanger sequenced and then analyzed using Synthego's Inference of CRISPR Edits (ICE) tool. The Cdc42 forward sequencing primer had an

estimated indel frequency of 83% while the reverse sequencing primer indel frequency was 93%. Based on these results, we proceeded to clonal analysis. Serially diluted cells were plated at a density of 0.5 cells/well on a P96-well plate. Wells containing a single cell were identified by phase-contrast microscopy and tracked as the culture expanded. Ten clones were selected and were evaluated using several methods. First, the clones were analyzed using the Synthego ICE tool. Promising clones were next assessed by Amplicon sequencing, and Quantitative Western blot.

Amplicon sequencing. gDNA was harvested from 5 million cells for WT and Cdc42-KO clones (Invitrogen Purelink Genomic DNA Kit). The purified gDNA was then used as a PCR template for primers that flank the CRISPR cut site. The forward primer sequence was 5'-ACACTCTTTCCCTACACGACGCTCTTCCGATCTccagcatgcttttaacactttgagg while the reverse primer sequence was 5'- GACTGGAGTTCAGACGTGTGCTCTTCCGATCTgaaaggagtctttggacagtggtg. Upper case letters in the primer indicate the partial Illumina adapter sequences. The PCR product was cleaned (Zymo DNA clean and concentrator-5) and then sent to Genewiz for 2 x 250 bp amplicon sequencing (Amplicon-EZ service). The amplicon sequences were analyzed using MATLAB to identify unique sequences after excluding sequences that did not match the primer sequences. Additionally, a small number of nonspecific sequences of less than 100 bp that were observed in all samples were removed. For each remaining unique sequence, the number of identically matching reads was counted. Sequences were aligned to the genomic sequence of the human Cdc42 gene to determine deleted or mutated regions. The 3 most frequently observed sequences for both forward and reverse sequences are shown (Supplementary Fig. 3a).

Immunoblots. Cdc42 protein expression levels were compared using Western Blotting. Differentiated PLB-985 cells were lysed at 4 °C in NP40 buffer (150 mM NaCl, 50 mM Tris Base, 1% NP40, PH 8.0) plus protease inhibitor (Thermo cat#: 78429) by repeatedly passing the cells through a 21-gauge syringe

needle. Cell lysates were centrifuged to remove cellular debris, snap frozen in liquid nitrogen, and stored at -80 °C. Lysates were thawed on ice, and protein levels were quantified with the Pierce 660 nm protein absorbance assay kit (22660) on a Molecular Devices SpectraMax spectrophotometer. Lysates were then solubilized by mixing 3:1 lysate to Li-Cor 4x loading buffer (928-40004) plus 10% Beta-Mercaptoethanol (Sigma). Samples were denatured by boiling for 5 min followed by cooling on ice for 2 min. 15 µg of total protein per sample were loaded on a 4-15% gradient polyacrylamide gel (BioRad #4561084) and run for 15 min at 100 V followed by ~35 min at 150 V. Proteins were transferred onto nitrocellulose membranes for 1.25 hrs at 100 V. The membrane was blocked using Li-Cor Intercept TBS blocking buffer for 30 min. Anti-Cdc42 primary antibody (Abcam Cat# ab187643) was diluted 1:10,000 in blocking buffer and incubated overnight at 4 °C on a rotary shaker. The following day, the membrane was washed 3x with TBST (1% Tween 20 in Tris Buffered Saline), and then incubated with secondary antibody at RT for 1 hr on a rotary shaker in the dark. The secondary antibody (Li-Cor IRDye® 800CW Donkey anti-Rabbit IgG Secondary Antibody) was diluted 1:15,000 into blocking buffer + 0.2% Tween 20. Post staining, the membrane was washed 3x in TBST. Membranes were washed once in deionized water and imaged using the Li-Cor Odyssey Imager (model 9120) using the 800 nm channel. Post imaging, the antibody labeling steps were repeated on the same membrane for the rabbit anti-β-Actin antibody (Cell Signaling Technology Cat# 4967). The β-actin antibody was diluted 1:1000 in blocking buffer, incubated overnight, and labeled the next day with the Li-Cor 800CW Donkey anti-rabbit secondary. The membrane was imaged using the Li-Cor Odyssey Imager at 800 nm (Supplementary Fig. 3b).

Retinal preparation. All retinal solutions were prepared in a dark room with red-light sources. 9-*cis*-retinal (Sigma Aldrich R5754) was dissolved in argon purged, 200 proof ethanol (Sigma Aldrich) to reach a concentration of 10 mg/mL. Aliquots were stored in small amber glass tubes (Sigma Aldrich) at -80 °C. 9-*cis*-retinal is hydrophobic, and requires a 1% w/v BSA carrier solution[43,44]. To prepare the carrier solution, Bovine Serum Albumin (BSA), Fraction V—Low-Endotoxin Grade (Gemini Bio 700-102P) was

dissolved in L-15 imaging media. Importantly, this BSA product is low in non-esterified fatty acids, which can inhibit the effectiveness of the BSA as a carrier[44]. Next, 10 µL of retinal stock was diluted to a working concentration of 10 µg/mL by incrementally adding the 1% BSA solution (9 x 10 µL, 4 x 100 µL, 1 x 500 µL, 9 x 1 mL) until the final volume was 10 mL. The working retinal solution was then stored in a light-proof box and mixed overnight at 4 °C. Prior to an imaging experiment, cells were resuspended in the 10 µg/mL retinal solution and incubated for 1hr at 37 °C. The diluted retinal solution was kept for up to 3 days. All downstream processing steps after cells were incubated in retinal were carried out in the dark.

Microscope configuration for TomKat FRET sensor imaging. All imaging experiments were conducted using a Nikon Eclipse Ti stand with dual Andor Zyla 4.2 sCMOS cameras. The microscope is controlled by MATLAB via Micromanager, allowing automated and highly repeatable experimental scripts. Simultaneous image acquisition for each FRET channel was achieved using a Cairn TwinCam LS image splitter. The TomKat FRET sensor requires 561 nm excitation of td-Tomato while the FRET acceptor (td-Katushka2) has its excitation maxima at ~590 nm. Thus, we designed our optics to isolate the td-Tomato emission spectra (combined ~573-600 nm bandpass) to one camera, while the td-Katusha2 and any potential td-Tomato bleed-through emissions were sent to the second camera (> 610 nm). For global stimulation experiments with the TomKat FRET sensor, populations of cells were imaged at 20x (Nikon Apochromat 0.75 NA) via epifluorescent illumination with the X-Cite XLED1 GYX LED. For the high spatial resolution under-agarose experiments, a 561 nm laser line (Andor) was used for Total Internal Reflection Fluorescence Imaging (TIRF) with a 60x Nikon Apochromat objective (1.49 NA). Our GYX LED has a dual 560/640 band excitation filter, thus the TomKat filter cube requires a short pass excitation filter that blocks the longer wavelengths (Semrock, BSP01-633R excitation filter). The TomKat filter cube uses a single edge dichroic that reflects ~560 nm light while passing longer wavelengths for emission (ZT561rdc Chroma). Finally, the cube uses two ~570 nm long pass emission filters to prevent the TIRF laser illumination from reaching the cameras (ET570lp Chroma). The TwinCam image splitter

uses the following filter configuration to properly capture the two FRET channels on their appropriate cameras. The image splitter dichroic is positioned to reflect wavelengths < 605 nm to one camera and pass longer wavelengths to the other (ZT594rdc Chroma). The td-Tomato side of the cube (< 605 nm) additionally uses an emission filter to further block wavelengths > 600nm to ensure that only td-Tomato emission signal is hitting the camera (ET560_80m Chroma). Finally, the td-Katushka2 side of the cube uses a long pass emission filter that blocks wavelengths < 610 nm.

Camera and illumination corrections. The dark-state noise for each camera was empirically measured by capturing 79 images without illumination and with the light path switched to the oculars. The median over the stack was used to generate the dark-state correction image, which is then subtracted from all experimental images. Next, uniform dye preparations were used to correct for variability in pixel responsiveness as well as camera and illumination artifacts. Rose bengal dye solution (0.3 mg/mL) was centrifuged at 21,000 RCF for 5 min to remove insoluble particles. 2 µL of dye was plated in the center of a P96-glassbottomed imaging plate (Cellvis P96-1.5H-N). A 5 mm round coverslip was applied to the dye droplet to create a thin, uniform layer of dye. TomKat epifluorescent dye images were captured ($n \geq 1000$) and the median for each camera was taken over the image stack. To correct for differences between each half of the camera sensor, the ratio of the mean pixel intensity for two rows above and below the middle of the camera chip was used to generate a correction factor. This correction factor was then applied to the bottom half of an image-sized matrix of ones, creating a half-chip correction. The half-chip correction is multiplied by all imported images after the dark-state subtraction. Dust in the microscope light path was observed to cause a small dark spot in the dye image on one of the cameras. To correct for this illumination artifact, the median dye image was smoothed using a broad gaussian filter (sigma = 30) to create a filtered image that does not have the spot artifact. The ratio of the median dye image to the smoothed dye image was used to generate a logical mask for the dim pixels in the artifact spot. The pixels in the mask were smoothed with a gaussian filter (sigma = 10), then this image was divided by the median

dye image to create a dust correction image. These images were generated for both cameras and were applied after the half-chip correction for images collected at 60x.

A gradient in FRET ratio activity was empirically observed from the top to bottom of the TomKat FRET sensor images. A ratio correction image was developed to remove this gradient in FRET activity for both the 20x and 60x objectives. Images of unstimulated Cdc42 TomKat FRET sensor cells were collected with cells positioned randomly throughout the images so that at least one cell was imaged on every portion of the camera sensor. These images were processed with our standard pipeline to generate FRET ratio images. The pixel-by-pixel median FRET ratio was then taken over all images (including only data from pixels inside cells). To reduce noise and local variability, this median image was then broken into 24x24 pixel blocks and the median was taken for each block. The resulting image was smoothed using a gaussian filter (sigma = 5) and the image was resized to match the input image size. To apply the correction, FRET ratio images are divided by the ratio correction image.

For center stimulation experiments, local activation of the parapinopsina receptor with 407 nm light focused through the FRAP module causes a small amount of photobleaching of the Cdc42 FRET sensor which could cause bias in signaling measurements (Supplementary Fig. 6). To correct for this, we measured the diameter and recovery rate for bleached sensor molecules using a high-power stimulus (37 µW for 10 ms) to develop a diffusion model of the bleached sensor using an empirically fit initial bleaching pattern. The diffusion coefficient used in the model was 0.5 µm/s. A bleaching correction was generated for each post-stimulation frame for each cell by modeling sensor diffusion, centered around the empirically measured FRAP stimulation target site and scaled to match the experimental laser stimulation power.

Global stimulation imaging and image analysis. Post retinal incubation, differentiated cells were resuspended in L-15 imaging media that contained 2% heat-inactivated FBS and were plated in glass-bottomed 384-well plates at a density of ~1100 cells/µL x 20 µL (Corning Cat#: 4581). All imaging experiments were conducted at 37 °C and were terminated after 5 hours of imaging. Separate cell lines or

treatment conditions were positioned so that all lines were imaged evenly throughout the experiment. Global UV stimulations were delivered using the DAPI epifluorescent channel. Stimulation power was manipulated by altering exposure time and LED power. For continuous stimulation experiments, UV stimulation and TomKat FRET sensor imaging were alternated until the stimulation period was over. Images were captured at a frame rate of 1.5 s, although prolonged global stimulation experiments required DAPI and TomKat filter cube switching, which slowed the image capture rate.

For the global stimulation experiments, pertussis toxin (600 ng/ml), IPA-3 (5 μM) and Latrunculin-A (1 μM) were used to perturb signaling pathways. The pertussis toxin was added to the retinal incubation step, and the incubation duration was extended to 2.5 hrs. The control cells received the same extended retinal duration. For the Latrunculin-A and IPA-3 conditions, the inhibitors were added to the retinal solution and incubated for 1 hr. Additionally, cells were plated with these compounds added to the imaging media to ensure inhibition during the experiment.

FRET pair images were aligned with a custom MATLAB function that uses a coordinate-mapping strategy as described[10]. Aligned images were cropped to ensure that both images are the same size. Next, the dimmest pixels (1.5 percentile) across all frames were used to define the background pixels. Since the cells are densely packed, empty-well images (median of ~1400 for each channel) were used to estimate the background spatial profile. The dimmest pixels were used to scale the brightness of the empty-well images prior to background subtraction. Next, pixels were filtered and removed from further analysis if they were dim, near saturating, or if the FRET ratio of the pixel was low (< 0.8), indicating that the cell was unhealthy or dead. Dying and dead cells have high autofluorescence that is independent of the FRET sensor, causing high FRET donor signal and low FRET values. Because this filter was applied on a per pixel basis that changed across time points, a conservative dead cell FRET ratio threshold was selected. Finally, the mean intensity was calculated for each channel before the ratio was taken. Whole-frame mean FRET ratio values were computed for each well at each timepoint. Plots were generated from means and standard errors computed over all replicate wells from all experiments. Plotted data was normalized by the mean of the timepoints prior to stimulation. Qualitative trends were

consistent across experiments from different days. For global stimulation plots, time on the x-axis is relative to the Cdc42 FRET image immediately preceding stimulation.

The exact sample size for each global stimulation experiment was recorded in the figure legends, except for Fig. 2b. The following well replicates were used to generate Fig. 2b. $n_{well\ replicates} = 23$ for relative light intensity = 0, $n_{well\ replicates} = 7$ for relative light intensity = 1, $n_{well\ replicates} = 7$ for relative light intensity = 2, $n_{well\ replicates} = 7$ for relative light intensity = 3, $n_{well\ replicates} = 7$ for relative light intensity = 4, $n_{well\ replicates} = 7$ for relative light intensity = 5, $n_{well\ replicates} = 7$ for relative light intensity = 6, $n_{well\ replicates} = 7$ for relative light intensity = 7, $n_{well\ replicates} = 13$ for relative light intensity = 8, $n_{well\ replicates} = 7$ for relative light intensity = 9, $n_{well\ replicates} = 14$ for relative light intensity = 10, $n_{well\ replicates} = 7$ for relative light intensity = 20, $n_{well\ replicates} = 7$ for relative light intensity = 30, $n_{well\ replicates} = 13$ for relative light intensity = 40, $n_{well\ replicates} = 7$ for relative light intensity = 50, $n_{well\ replicates} = 7$ for relative light intensity = 60, $n_{well\ replicates} = 7$ for relative light intensity = 70, $n_{well\ replicates} = 13$ for relative light intensity = 80, $n_{well\ replicates} = 7$ for relative light intensity = 90, $n_{well\ replicates} = 7$ for relative light intensity = 100.

To investigate the Cdc42 response on a single cell level, single-pulse, global stimulation experiments were re-examined. Images were aligned, cropped, and background subtracted as above. The sum of the FRET donor and acceptor images was used for masking as the sum has better signal to noise ratio and is less susceptible to changes in signal intensity due to FRET. To generate cell masks for tracking, the sum image was smoothed using a gaussian filter with a standard deviation of 2 and then sharpened using unsharp masking. Automatic thresholding was used to define the cell masks. Strict minimum and maximum cell area thresholds were applied to the masks to remove cell fragments or cell aggregates. Finally, the centroids of the cell masks were tracked across all frames using a reciprocal nearest neighbor tracking strategy. Cells that could not be tracked across all images were removed from further analysis. Dead cells were filtered on a per cell basis using the FRET ratio mean of the first ten frames (pre-stimulus). Based on a bimodal distribution of measured baseline FRET values, cells with a baseline FRET ratio < 0.95 were thus removed from the analysis. Additionally, cells that contained saturated pixels in either the td-Tomato or td-Katushka2 channel were removed. FRET ratio fold change

was assessed by breaking the cellular response into three, 7.5 s windows (Control1 = -13.5 s to -7.5 s, Control2 = -6 s to 0 s, Peak = 4.5 s to 10.5 s). The response mean was taken over the five frames in each window and then the ratio of the Peak window to the Control2 window was taken. Additionally, the ratio of Control1 to Control2 was computed (Supplementary Fig. 1c). Histograms for single-cell data were computed for 4 experiments conducted on different days. These histograms were averaged, and the standard error of the mean was computed for each histogram bin. The qualitative trend was the same for all four experiments.

Under-agarose cell preparation. Several experiments were conducted using an under-agarose cell preparation on a 96-well plate format (Cellvis Cat#: P96-1.5H-N). A detailed protocol for the under-agarose preparation can be found as described[45]. In brief, differentiated cells (~1,000 – 1,500) were plated in the center of a well in a 5 µL drop of 2% heat-inactivated FBS + L-15 imaging media. Cells were allowed to adhere to the glass for 5 min, before a 195 µL layer of 1.5% low-melt agarose (Invitrogen Cat#: 16520-100) mixed with 10% heat-inactivated FBS + L-15 imaging media equilibrated to 37 °C was overlayed on top. The agarose solution was allowed to solidify at RT for 40 min before the plate was transferred to the microscope incubator and warmed to 37 °C for 40 min prior to imaging. Importantly, the cells must remain in the interface between the agarose and the glass for proper motility. Thus, careful pipetting of the agarose solution is required to prevent dislodging cells from the glass.

TIRF image background subtraction and cell segmentation. Raw images were first corrected for the camera dark-state noise, differences in camera chip sensitivity, and dust in the light path as described above. FRET pair images were aligned using the coordinate-mapping strategy noted above. Next, cells were segmented by first summing the FRET donor and acceptor images to enhance signal to noise. The sum images were used to conservatively define background and cell object pixels. Next, background intensity images were computed using the median intensity of background pixels in the local neighborhood for each pixel. Background images were subtracted from the sum image, and object edges

were enhanced using unsharp-masking. To perform unsharp-masking, the image was smoothed using a broad gaussian filter (sigma=25), and then was subtracted from the original image. Finally, the cell object masks were defined using Otsu's threshold method.

After segmentation, each FRET donor and acceptor image was background subtracted using the background mask defined in the segmentation section. Next each image was smoothed using a gaussian filter (sigma=1) and pixels not in the cell mask were defined as not a number (NaN) to remove them from further analysis. The FRET ratio image was calculated as FRET acceptor divided by FRET donor. The FRET ratio image was then divided by the ratio correction image to account for the observed gradient in FRET sensor activity in the images.

Cdc42 spatial activity analysis. The spatial activity pattern of the Cdc42 TomKat and CFP/YFP FRET sensors were measured and compared to validate proper function of the new TomKat FRET sensor. Differentiated Cells were plated using the under-agarose preparation. Then time-lapse TIRF microscopy images for randomly migrating, unstimulated cells were collected for each FRET pair. Assessment of the FRET sensor spatial activity was determined using the following image analysis steps as described[10]. Cells were segmented and tracked using the approximate nearest neighbor search method based on cell centroid positions. Cell tracks were manually curated to select only frames where cells were consistently moving. Cell protrusions were defined from frame to frame by subtracting the cell masks and identifying the largest connected protruding edge region. The protrusion was also required to be within one pixel of the defined protrusion from the previous and following frames. Next the shortest distance between each pixel in the cell mask and the protrusion mask was calculated using the bwdistgeodesic MATLAB function. The mean FRET ratio was calculated as a function of distance from the leading edge of the cell. Plotted data was normalized to be 1 at the leading edge (Distance from Protrusion = 0 μm).

Cdc42-KO cell phenotype characterization. Differentiated PLB-985 WT and Cdc42-KO cells were plated using the under-agarose preparation. Unstimulated, randomly migrating cells were imaged using

TIRF microscopy. Cells were segmented as described above and grayscale movies were generated. Cells were manually counted as the cytoplasmic tether phenotype was difficult to accurately segment. Four experiments were analyzed, and the standard error of the mean was calculated for the mean of the four experiments.

Analysis of persistence of cell migration. Differentiated PLB WT and Cdc42-KO cells were plated using the under-agarose preparation. Unstimulated, randomly migrating cells were imaged using 10X magnification epifluorescence microscopy. Cells were imaged for 7 min, with images acquired every 30 seconds. Cells were segmented and tracked using custom MATLAB software as previously described[46]. Briefly, cells were segmented using a manually determined intensity threshold, with minimum and maximum cell area thresholds. Cells were tracked using a reciprocal nearest neighbor algorithm. Two measures of persistence were computed. First, we computed the cosine of the angle between the direction of movement in the first 30 s, and the direction of movement in each subsequent frame-to-frame step. Only cells that moved at least 5 μm in the first 30 second step were included for analysis to capture only moving cells for which an initial direction could be determined accurately. We then computed the mean cosine value for each time point to determine the decay of directional persistence. Second, we computed the mean squared displacement as a function of time. Only cells that moved at least 5 μm from their starting position during the imaging interval were included for analysis to exclude unhealthy or nonmoving cells. The mean and standard error of the mean were computed at each timepoint over four independent experiments.

Optogenetic laser stimulation using the FRAP module. Optogenetic stimulation was achieved for high resolution, TIRF microscopy experiments, by stimulating cells with a 407 nm laser (Coherent Cube) focused through a Fluorescence Recovery After Photobleaching (FRAP) module on the microscope. The TomKat dichroic can pass 407 nm light, allowing for rapid FRAP stimulation without changing the filter cubes. To focus the FRAP module, PLB cells expressing the TomKat FRET sensor were plated using the

under-agarose preparation. Cells were imaged in TIRF to determine the appropriate focal plane. The FRAP laser was tuned to 40 ms exposure and 10 mW power. Cells were then selected and imaged using the FRAP channel. The X and Y translation knobs were used to adjust the FRAP spot until it was near the center of the image (~512x512 on a 1024x1024 pixel image). Next the Z-adjustment knob was used to focus the FRAP spot into a tight gaussian. Power measurements of the FRAP laser at the objective were taken using a Thorlabs handheld optical power meter (PM100D) and microscope slide power sensor (S170C). Cell driving experiments were conducted using ~2 µW power measured at the objective. Center-stimulation experiments were conducted using 4.3 or 0.8 µW power. The input laser could not be reliably tuned to achieve the 0.8 µW power value. Instead, a 1% neutral density filter was added to the FRAP module light path. This power level was also below the detection limit for the power meter. Three higher power measurements were collected with the ND filter installed, and a line was fitted to determine the nominal laser power required to stimulate cells at ~0.8 µW. On each experimental day, ten pictures of the FRAP spot were collected and averaged to identify the pixel with the maximum FRAP spot intensity. This pixel location was saved and used for the remainder of the experiment. The mean FRAP spot image was saved and used for identifying the FRAP spot location in the image analysis steps.

Optogenetic cell driving and cell center stimulation assays. For optogenetic experiments, differentiated cells were pre-incubated with the 9-*cis*-retinal solution, and all plating steps of the under-agarose preparation were conducted in the dark with a red headlamp for illumination. For Latrunculin-A experiments, cells were treated with 1 µM Latrunculin-A during the 1 hr retinal incubation period. Additionally, Latrunculin-A was added to the 10% heat-inactivated FBS + L-15 imaging media prior to mixing with the agarose solution to yield a final concentration of 1 µm Latrunculin-A.

Automated imaging scripts for cell driving and center-stimulation assays were developed in MATLAB. To automatically identify cells, an individual well on a 96-well plate was broken into a 7x7 search grid. A scan image was collected for each position in the grid, and objects were identified using the cell masking strategy described above. If a cell was detected, the script would center the stage on the cell

using the cell centroid. Driving a cell required consistent delivery of FRAP stimulation to a region on the cell edge. To achieve this, a target angle was selected by the user. A MATLAB function was developed that would calculate the angle between the cell centroid and all outermost pixels on the cell perimeter. The perimeter pixel that had the closest match to the target angle was selected. The stage was translated so that the cell edge was centered on the empirically measured FRAP spot location and a low powered, ~2 µw 407 nm FRAP stimulus was applied to the cell. Next the FRET images were collected, and the new cell coordinates were calculated from the td-Katushka-2 image using the cell masking and edge selection strategy. The stage coordinates for each movement required for imaging the cell were recorded and used for post processing of figures and movies. Cells were imaged using 3 or 5 second intervals. Once the experiment was completed for the individual cell, the script moved to the next position in the scan grid. When an individual grid was completed the script then moved to the next well and repeated the process. Depending on the experimental conditions, several hundred cells could be imaged in one, four-hour experiment automatically.

The center-stimulation assay used the same scanning and cell detection methods as the optogenetic driving assay. Once a cell was detected, the stage was moved to the centroid of the cell mask. This centering process was used for every frame before the FRAP stimulus was applied. Post stimulation however, the centering step was no longer required; this was true for both the single stimulation and 5-pulse stimulation experiments. Cells were imaged at a frame rate of 1 or 0.5 seconds. Prior to each center stimulation experiment, 3-5 cells were driven with the cell driving assay to confirm that the optogenetic receptor and stimulation system were functional.

To evaluate the spatial spread of Cdc42 activity in cells stimulated with the center-stimulation protocol, cell images were pre-screened to remove cell clusters or dead cells. Additionally, the saved FRAP spot image was converted into a logical mask where the brightest pixel in the FRAP spot was set to one. FRET images were aligned and segmented, and FRET ratio images were calculated using the TIRF image segmentation method described above. Next, cell mask, FRAP mask, and FRET images were adjusted using the stage translation recordings so that all image frames were aligned with the first frame

in the set. For accurate analysis results, cells were screened using an automated custom MATLAB function to ensure limited translocation away from the FRAP stimulus site. The function removed cells if the FRAP mask could not be overlayed with the cell mask, if the FRAP mask was less than four pixels from the cell edge or if the Euclidean distance traveled for the cell centroid was greater than 4 μm for any frame post-stimulation. The photobleaching correction was applied to the FRET ratio images to account for FRET sensor bleaching due to FRAP stimulation. All pixels within a cell mask were measured to determine their distance away from the FRAP stimulation site pixel. These distance masks were used to sort pixels into concentric bins that were 1 μm in width. Pixels closest to the stimulation site were placed in bin 1 while pixels on the cell periphery were placed in the higher bins (Fig. 5c). The mean intensity values for the donor and acceptor were calculated for each bin, and then the FRET ratio for each bin was calculated. For this analysis, the ratio correction image was applied to the FRET acceptor images before the bin analysis was applied. To evaluate FRET ratio fold-change, the FRET ratio values for each bin from frames post-stimulation were divided by the corresponding bins from the frame immediately preceding stimulation. These FRET ratio fold-change bin measurements were compiled for all cells within experimental groups and the mean used to generate the plots in Fig. 5.

3.8 Statistical analysis:

All error bar and shaded error regions represent standard error of the mean. Significance values were calculated using a two-tailed, t-test with unequal variance (MATLAB's ttest2 function). The t-test assumes that the underlying distributions are normal distributions. We used the unequal variance version because the variability was empirically larger for the Cdc42-KO cell line than for the control cell line. For Fig. 3d we computed a t-value of 5.65 with 3.01 degrees of freedom, and a 95% confidence interval for the effect size of 0.158 to 0.0562. For global stimulation assays used in Fig. 1d, 2b,e-h, 4b-i and Supplementary Fig. 1a,b, 2, and 4, measurements of populations of cells in distinct wells were used as the independent unit, with parallel measurements made for differing drug or light stimulation conditions.

Each experiment was repeated on at least two independent days, except for the control experiment in Fig. 4b, the control experiment in Supplementary Fig. 1b, and the PAK1-inhibited experiment from Supplementary Fig. 4a. For the local, center-stimulation experiments used in Fig. 5 and Supplementary Figure 5, individual cells were used as the independent unit, because each cell was stimulated and measured independently, and cell-to-cell variation was the largest source of variability.

3.9 Data availability:

The datasets generated from this study are available from the corresponding author upon reasonable request. Amplicon sequencing data is available on the NCBI-Trace sequence read archive under BioProject PRJNA720484. Control sequences (BioSample: SAMN18651945) and Cdc42-KO sequences (BioSample: SAMN18651944) are stored in separate files.

3.10 Code availability:

Custom MATLAB code used in this study is available from the corresponding author upon reasonable request.

3.11 References:

1. Van Haastert, P. J. M. & Devreotes, P. N. Chemotaxis: Signaling the way forward. *Nat. Rev. Mol. Cell Biol.* **5**, 626–634 (2004).

2. Weiner, O. D. Regulation of cell polarity during eukaryotic chemotaxis: the chemotactic compass. *Curr. Opin. Cell Biol.* **14**, 196–202 (2002).

3. Xu, J. *et al.* Divergent signals and cytoskeletal assemblies regulate self-organizing polarity in neutrophils. *Cell* **114**, 201–14 (2003).

4. Janetopoulos, C., Jin, T. & Devreotes, P. Receptor-mediated activation of heterotrimeric G-proteins in living cells. *Science* **291**, 2408–2411 (2001).

5. Devreotes, P. & Janetopoulos, C. Eukaryotic chemotaxis: distinctions between directional sensing and polarization. *J. Biol. Chem.* **278**, 20445–20448 (2003).

6. Parent, C. A. & Devreotes, P. N. A cell's sense of direction. *Science* **284**, 765–770 (1999).

7. Devreotes, P. N. *et al.* Excitable Signal Transduction Networks in Directed Cell Migration. *Annu. Rev. Cell Dev. Biol.* **33**, 103–125 (2017).

8. Wang, Y. *et al.* Identifying network motifs that buffer front-to-back signaling in polarized neutrophils. *Cell Rep.* **3**, 1607–1616 (2013).

9. Chang, J. B. & Ferrell, J. E. Mitotic trigger waves and the spatial coordination of the Xenopus cell cycle. *Nature* **500**, 603–607 (2013).

10. Yang, H. W., Collins, S. R. & Meyer, T. Locally excitable Cdc42 signals steer cells during chemotaxis. *Nat Cell Biol* **18**, 191–201 (2016).

11. Servant, G. *et al.* Polarization of Chemoattractant Receptor Signaling During Neutrophil Chemotaxis. *Science* **287**, 1037–1040 (2000).

12. Parent, C. A., Blacklock, B. J., Froehlich, W. M., Murphy, D. B. & Devreotes, P. N. G-protein signaling events are activated at the leading edge of chemotactic cells. *Cell* **95**, 81–91 (1998).

13. Srinivasan, S. *et al.* Rac and Cdc42 play distinct roles in regulating PI(3,4,5)P3 and polarity during neutrophil chemotaxis. *J Cell Biol* **160**, 375–85 (2003).

14. Szczur, K., Zheng, Y. & Filippi, M.-D. The small Rho GTPase Cdc42 regulates neutrophil polarity via CD11b integrin signaling. *Blood* **114**, 4527–4537 (2009).

15. Kawano-Yamashita, E. *et al.* Activation of transducin by bistable pigment parapinopsin in the pineal organ of lower vertebrates. *PLoS One* **10**, e0141280 (2015).

16. Koyanagi, M. *et al.* Diversification of non-visual photopigment parapinopsin in spectral sensitivity for diverse pineal functions. *BMC Biol* **13**, 73 (2015).

17. Karunarathne, W. K., Giri, L., Patel, A. K., Venkatesh, K. V. & Gautam, N. Optical control demonstrates switch-like PIP3 dynamics underlying the initiation of immune cell migration. *Proc Natl Acad Sci U A* **110**, E1575-83 (2013).

18. O'Neill, P. R. *et al.* Membrane flow drives an adhesion-independent amoeboid cell migration mode. *Dev. Cell* (2018).

19. Hadjitheodorou, A. *et al.* Directional reorientation of migrating neutrophils is limited by suppression of receptor input signaling at the cell rear through myosin II activity. *bioRxiv* 2021.04.04.438336 (2021) doi:10.1101/2021.04.04.438336.

20. Komatsu, N. *et al.* Development of an optimized backbone of FRET biosensors for kinases and GTPases. *Mol Biol Cell* **22**, 4647–4656 (2011).

21. Bos, J. L., Rehmann, H. & Wittinghofer, A. GEFs and GAPs: Critical elements in the control of small G-proteins. *Cell* **129**, 865–877 (2007).

22. Xiong, Y., Huang, C. H., Iglesias, P. A. & Devreotes, P. N. Cells navigate with a local-excitation, global-inhibition-biased excitable network. *Proc. Natl. Acad. Sci. U. S. A.* **107**, 17079–86 (2010).

23. Jilkine, A. & Edelstein-Keshet, L. A comparison of mathematical models for polarization of single eukaryotic cells in response to guided cues. *PLoS Comput Biol* **7**, e1001121 (2011).

24. Devreotes, P. & Horwitz, A. R. Signaling networks that regulate cell migration. *Cold Spring Harb. Perspect. Biol.* **7**, a005959 (2015).

25. Zhan, H. *et al.* An excitable Ras/PI3K/ERK signaling network controls migration and oncogenic transformation in epithelial cells. *Dev. Cell* **54**, 608-623.e5 (2020).

26. Li, Z. *et al.* Directional sensing requires Gβγ-mediated PAK1 and PIX alpha-dependent activation of Cdc42. *Cell* **114**, 215–27 (2003).

27. Tang, M. *et al.* Evolutionarily conserved coupling of adaptive and excitable networks mediates eukaryotic chemotaxis. *Nat Commun* **5**, 5175 (2014).

28. Huang, C.-H., Tang, M., Shi, C., Iglesias, P. A. & Devreotes, P. N. An excitable signal integrator couples to an idling cytoskeletal oscillator to drive cell migration. *Nat Cell Biol* **15**, 1307 (2013).

29. O'Neill, P. R., Kalyanaraman, V. & Gautam, N. Subcellular optogenetic activation of Cdc42 controls local and distal signaling to drive immune cell migration. *Mol Biol Cell* **27**, 1442–50 (2016).

30. Houk, A. R. *et al.* Membrane tension maintains cell polarity by confining signals to the leading edge during neutrophil migration. *Cell* **148**, 175–188 (2012).

31. Diz-Muñoz, A. *et al.* Membrane tension acts through PLD2 and mTORC2 to limit actin network assembly during neutrophil migration. *PLOS Biol.* **14**, e1002474 (2016).

32. Janetopoulos, C., Ma, L., Devreotes, P. N. & Iglesias, P. A. Chemoattractant-induced phosphatidylinositol 3,4,5-trisphosphate accumulation is spatially amplified and adapts, independent of the actin cytoskeleton. *Proc. Natl. Acad. Sci.* **101**, 8951–8956 (2004).

33. Weiner, O. D. *et al.* Hem-1 complexes are essential for Rac activation, actin polymerization, and myosin regulation during neutrophil chemotaxis. *PLOS Biol.* **4**, e38 (2006).

34. Inoue, T. & Meyer, T. Synthetic activation of endogenous PI3K and Rac identifies an AND-gate switch for cell polarization and migration. *PLoS One* **3**, e3068 (2008).

35. Van Keymeulen, A. *et al.* To stabilize neutrophil polarity, PIP3 and Cdc42 augment RhoA activity at the back as well as signals at the front. *J. Cell Biol.* **174**, 437–445 (2006).

36. Müller, P. M. *et al.* Systems analysis of RhoGEF and RhoGAP regulatory proteins reveals spatially organized RAC1 signaling from integrin adhesions. *Nat. Cell Biol.* **22**, 498–511 (2020).

37. Ishii, K., Hein, L., Kobilka, B. & Coughlin, S. R. Kinetics of thrombin receptor cleavage on intact cells. Relation to signaling. *J Biol Chem* **268**, 9780–6 (1993).

38. Coward, P. *et al.* Controlling signaling with a specifically designed Gi-coupled receptor. *Proc. Natl. Acad. Sci.* **95**, 352–357 (1998).

39. Shcherbo, D. *et al.* Far-red fluorescent tags for protein imaging in living tissues. *Biochem. J.* **418**, 567–574 (2009).

40. Rincón, E., Rocha-Gregg, B. L. & Collins, S. R. A map of gene expression in neutrophil-like cell lines. *BMC Genomics* **19**, 573 (2018).

41. Yusa, K., Rad, R., Takeda, J. & Bradley, A. Generation of transgene-free induced pluripotent mouse stem cells by the piggyBac transposon. *Nat. Methods* **6**, 363–369 (2009).

42. Guignet, E. G. & Meyer, T. Suspended-drop electroporation for high-throughput delivery of biomolecules into cells. *Nat. Methods* **5**, 393–395 (2008).

43. Frederiksen, R. *et al.* Low aqueous solubility of 11-cis-retinal limits the rate of pigment formation and dark adaptation in salamander rods. *J. Gen. Physiol.* **139**, 493–505 (2012).

44. Yue, W. W. S. *et al.* Spontaneous activation of visual pigments in relation to openness/closedness of chromophore-binding pocket. *Elife* **6**, e18492 (2017).

44. Bell, G. R. R., Natwick, D. E. & Collins, S. R. Parallel high-resolution imaging of leukocyte chemotaxis under agarose with Rho-family GTPase biosensors. in *Rho GTPases: Methods and Protocols* (ed. Rivero, F.) 71–85 (Springer, 2018).

46. Collins, S. R. *et al.* Using light to shape chemical gradients for parallel and automated analysis of chemotaxis. *Mol. Syst. Biol.* **11**, 804 (2015).

3.12 Figures:

Figure 1

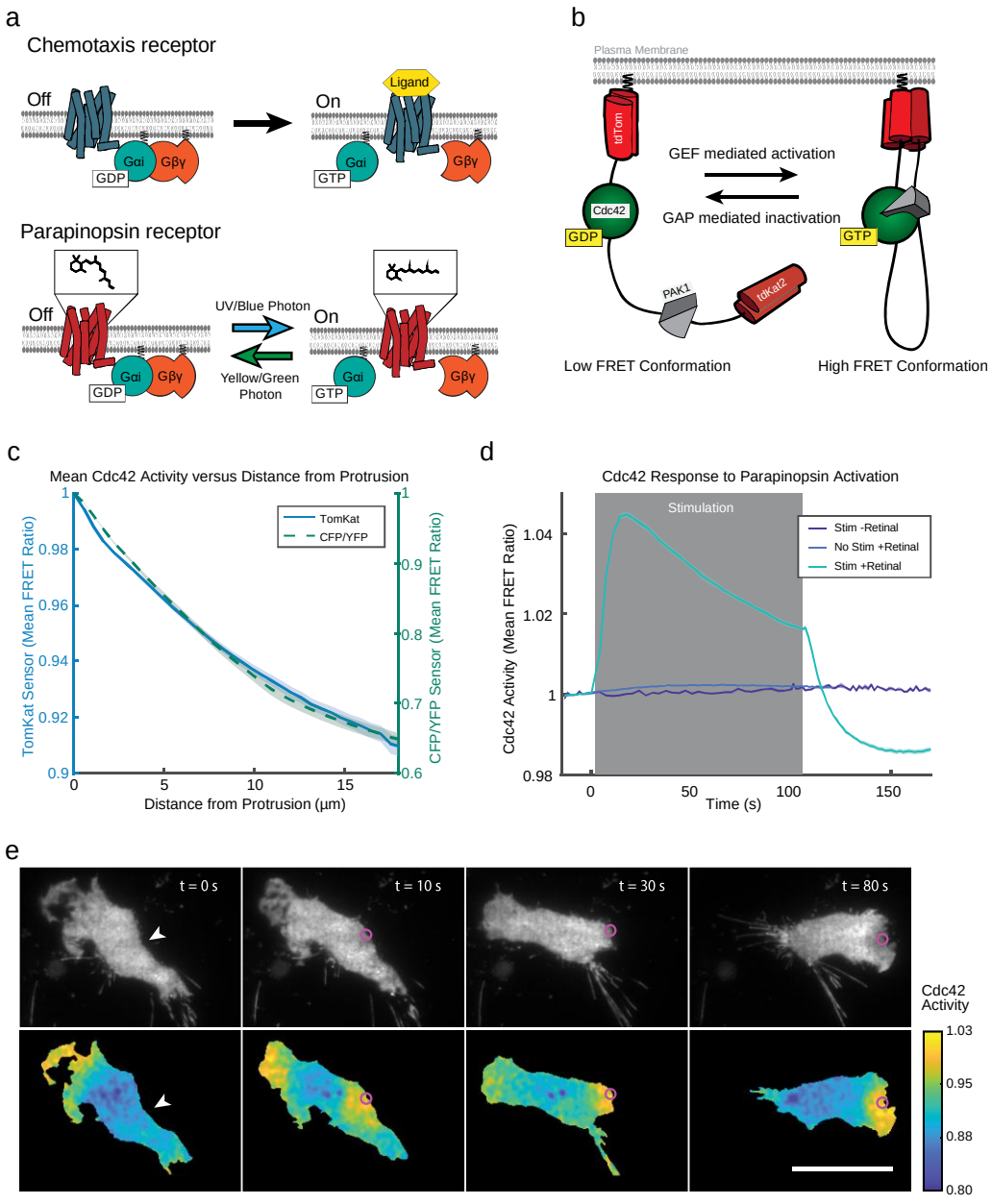

Figure 3.1 A molecular toolkit for optical control of receptor activity and measurement of signaling outputs in the same cell.

(**a**) Like chemoattractant receptors (above), parapinopsina (below) is a $G_i\alpha$ coupled GPCR that is activated by blue light. The chemical structure above the parapinopsina receptor represents the retinal

chromophore that facilitates photon detection and receptor activation. Blue light photo-isomerizes 9-*cis*-retinal to all *trans*-retinal, activating the receptor. Longer wavelengths inactivate the receptor and photo-isomerize the retinal chromophore back to the cis-conformation. (**b**) Schematic for the "TomKat" FRET sensor that is spectrally compatible with the optogenetic GPCR (parapinopsina). The FRET donor is tdTomato while tdKatushka2 is the FRET acceptor. The sensor contains the Cdc42 binding domain from PAK1 and a C-terminally truncated Cdc42 that are separated by a linker domain. The sensor C-terminus contains the K-Ras C-terminal polybasic region and CAAX motif. The CAAX motif is post translationally modified (farnesylated) and serves as a lipid anchor, associating the sensor with the plasma membrane. (**c**) The spatial activity profiles reported by TomKat and CFP/YFP FRET sensors in randomly moving differentiated PLB-985 cells. Shaded error regions represent ± s.e.m. of n=73 cells for TomKat sensor, n=59 cells for CFP/YFP sensor. (**d**) Cdc42 activity responses to global optogenetic GPCR activation are dependent on blue light stimulation and 9-*cis*-retinal cofactor. The response rapidly attenuates after stimulations cease, indicating that the receptor is inactivated by imaging with longer (> 530 nm) wavelengths of light. Shaded error regions represent ± s.e.m. of $n_{\text{well replicates}} = 19$ well replicates for no retinal condition (Stim -Ret), $n_{\text{well replicates}} = 31$ for no stimulation condition (No Stim +Ret), $n_{\text{well replicates}} = 59$ for stimulation with retinal (Stim +Ret). Relative light intesnsity = 10. Time on the x-axis is relative to the last FRET image before stimulation. (**e**) Focal stimulation of optogenetic-GPCR can repolarize a cell and drive a chemotaxis response. The white arrowheads indicate the target region pre-stimulus, while the magenta circles indicate the stimulated region. The Cdc42 TomKat sensor can be used to measure subcellular Cdc42 activity in the optogenetic GPCR stimulated cells. Scale bar, 25 μm.

Figure 2

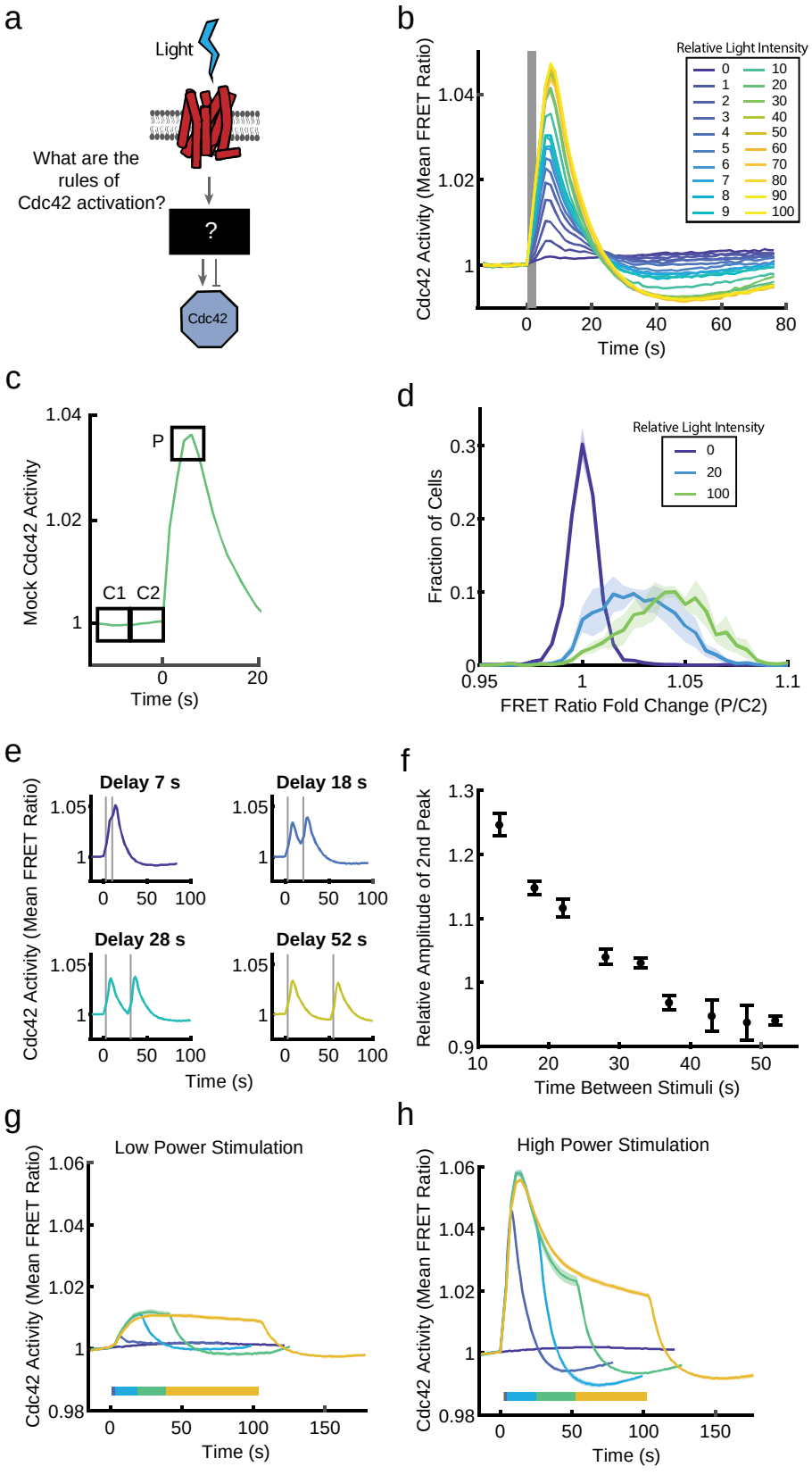
a
Light
What are the rules of Cdc42 activation?
?
Cdc42
b
Relative Light Intensity
0 1 2 3 4 5 6 7 8 9 10 20 30 40 50 60 70 80 90 100
Cdc42 Activity (Mean FRET Ratio)
1.04
1.02
1
0 20 40 60 80
Time (s)
c
Mock Cdc42 Activity
1.04
1.02
1
P
C1 C2
0 20
Time (s)
d
Relative Light Intensity
0 20 100
Fraction of Cells
0.3
0.2
0.1
0
0.95 1 1.05 1.1
FRET Ratio Fold Change (P/C2)
e
Delay 7 s
Delay 18 s
Delay 28 s
Delay 52 s
Cdc42 Activity (Mean FRET Ratio)
1.05
1
0 50 100
Time (s)
f
Relative Amplitude of 2nd Peak
1.3 1.2 1.1 1 0.9
10 20 30 40 50
Time Between Stimuli (s)
g
Low Power Stimulation
Cdc42 Activity (Mean FRET Ratio)
1.06 1.04 1.02 1 0.98
0 50 100 150
Time (s)
h
High Power Stimulation
Cdc42 Activity (Mean FRET Ratio)
1.06 1.04 1.02 1 0.98
0 50 100 150
Time (s)

Figure 3.2 Dose-dependent positive and negative signals downstream of receptors shape a graded Cdc42 response.

(**a**) Schematic of unknown signal processing between receptors and Cdc42. (**b**) Populations of PLB-985 cells expressing parapinopsina and the Cdc42 TomKat sensor were stimulated with a single light pulse of the indicated intensities. Mean FRET ratio was measured as a function of time. Stimulus duration is indicated by the gray bar. A minimum of seven well replicates were performed for each condition (exact numbers listed in the methods). See Supplementary Fig. 1a for plot with error bars. Tens to hundreds of cells were imaged in each well. (**c**) Schematic for analysis of single cell response amplitudes. For each cell, the response was broken into three, 7.5 s windows. The mean FRET ratio was calculated for each window (C1 = -13.5 s to -7.5 s, C2 = -6 s to 0 s, P = 4.5 s to 10.5 s). (**d**) Histograms of single-cell response amplitudes to a single light pulse stimulus of the indicated intensities. FRET ratio fold change was calculated by taking the ratio of the peak response (P) to the control window (C2). Total cell numbers of n=4127 cells (Relative light intensity = 0), n=2317 cells (Relative light intensity = 20), n=2261 cells (Relative light intensity =100) were analyzed from 4 independent experiments. The mean and standard error of the mean of the histogram values over the 4 experiments are shown. (**e**) Cdc42 responses are shown four different two pulse stimulation protocols with the indicated delay times between stimulations. The Relative Light Intensity was 10 for all plots. A minimum of four well replicates were performed for each condition. See Supplementary Fig. 2 for all two pulse stimulation plots. Stimulus duration indicated by gray bars. (**f**) Relative amplitude of the second Cdc42 response peak as a function of time between stimuli. The relative amplitude is calculated as the ratio of the second peak to the first peak. Time delay of 7 seconds was not included because a second peak could not be resolved from the first. The error bars indicate ± s.e.m. of $n_{\text{well replicates}}$ = 6 for 13 s, $n_{\text{well replicates}}$ = 6 for 18 s, $n_{\text{well replicates}}$ = 6 for 22 s, $n_{\text{well replicates}}$ = 6 for 28 s, $n_{\text{well replicates}}$ = 26 for 33 s, $n_{\text{well replicates}}$ = 4 for 37 s, $n_{\text{well replicates}}$ = 4 for 43 s, $n_{\text{well replicates}}$ = 4 for 48 s, $n_{\text{well replicates}}$ = 4 for 52 s. (**g**-**h**) Repeated global stimulations were applied to simulate continuous receptor stimulation. Stimulation duration indicated by horizontal color bars. (**g**) Cdc42 response to the

indicated stimulus durations with low power stimulation (Relative Light Intensity = 1). Shaded error regions represent ± s.e.m. of $n_{well\ replicates}$ = 65 for non-stimulated, $n_{well\ replicates}$ = 21 for 1 stimulation, $n_{well\ replicates}$ = 20 for 7 stimulations, $n_{well\ replicates}$ = 21 for 15 stimulations, and $n_{well\ replicates}$ = 27 for 30 stimulations. (**h**) Cdc42 response to the indicated stimulus durations with high power stimulation (Relative light lntensity = 100). Shaded error regions represent ± s.e.m. of $n_{well\ replicates}$ = 65 for 0 stimulation condition, $n_{well\ replicates}$ = 12 for 1 stimulation, $n_{well\ replicates}$ = 12 for 7 stimulations, $n_{well\ replicates}$ = 12 for 15 stimulations, and $n_{well\ replicates}$ = 77 for 30 stimulations.

Figure 3

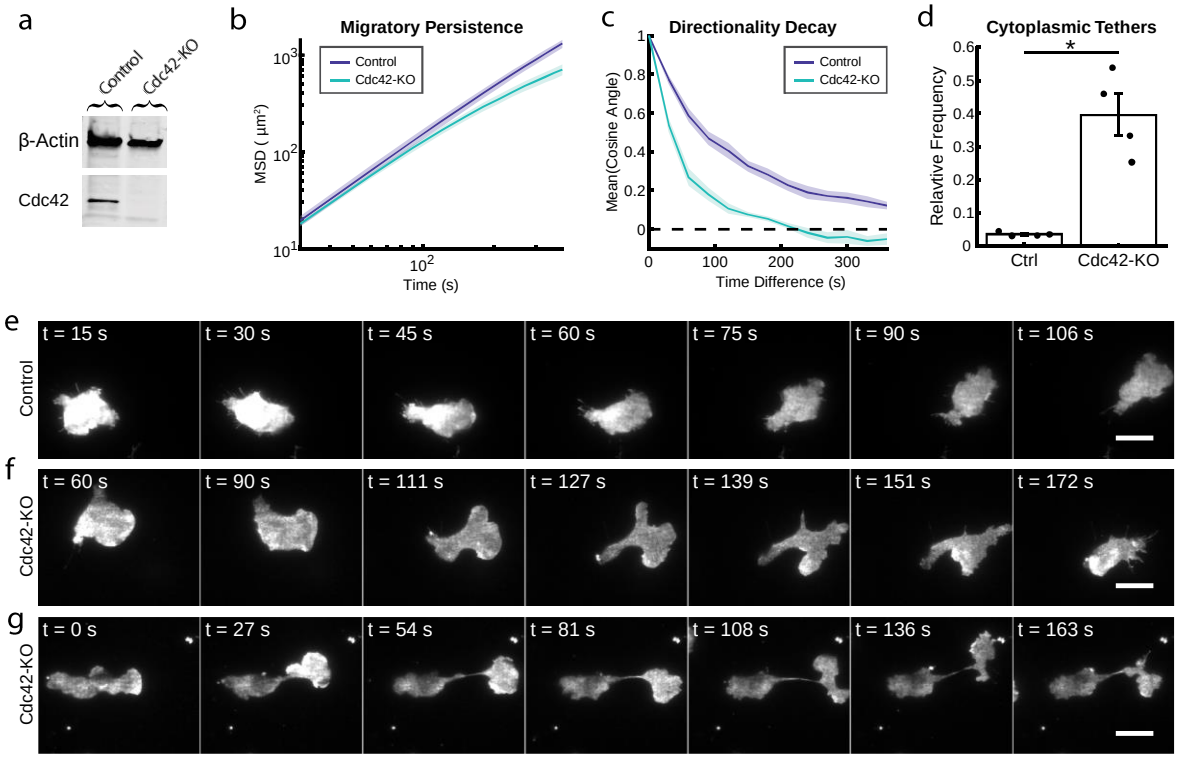

Figure 3.3 Genetic knockout of Cdc42 reveals a central role in organizing and maintaining cell polarity.

(**a**) Western blot comparing the Cdc42 knockout (Cdc42-KO) and control cell lines stained for β-actin and Cdc42. (**b**) The mean squared displacement (MSD) was measured as a function of time for control and Cdc42-KO cells randomly migrating in an under-agarose condition. Shaded error regions represent ± s.e.m. of $n_{experiment} = 4$. A total of 10,687 control cells and 3,018 Cdc42-KO cells were analyzed across the four experiments. (**c**) As a measure of directional persistence, the mean cosine of the angle between a migrating cell's movement direction at two different time points was measured as a function of the difference in time between the two measurements. Cells migrating in a straight line would have a mean cosine angle of 1. Shaded error regions represent ± s.e.m. of $n_{experiment} = 4$. A total of 4,821 control cells and 1,098 Cdc42-KO cells were analyzed across the four experiments. (**d**) Fraction of cells exhibiting the cytoplasmic tether phenotype. The error bars represent ± s.e.m. of $n_{experiment} = 4$. A total of 331 control

cells and 194 Cdc42-KO cells were analyzed across the four experiments. * indicates p-value =0.0108 using t-test with unequal variances. Scattered points represent relative frequency for each experimental replicate. (**e**) Time-lapse image series of control cell randomly migrating. Control cells tend to maintain one cell front at a time and migrate more persistently. Time points match the corresponding supplemental video. Scale bar, 15 μm. (**f**) Time-lapse image series of a Cdc42-KO cell randomly migrating. This cell displays a range of phenotypes including: a very large, crescent-shaped leading edge in the first time point and multiple repolarization events thereafter. Time points match the corresponding supplemental video. Scale bar, 15 μm. (**g**) Time-lapse image series of a representative Cdc42-KO cell randomly migrating. This cell displays the cytoplasmic tether phenotype where the leading edge pulls away from the cell body, but remains linked by a thin cytoplasmic filament. Time points match the corresponding supplemental video. Scale bar, 15 μm.

Figure 4

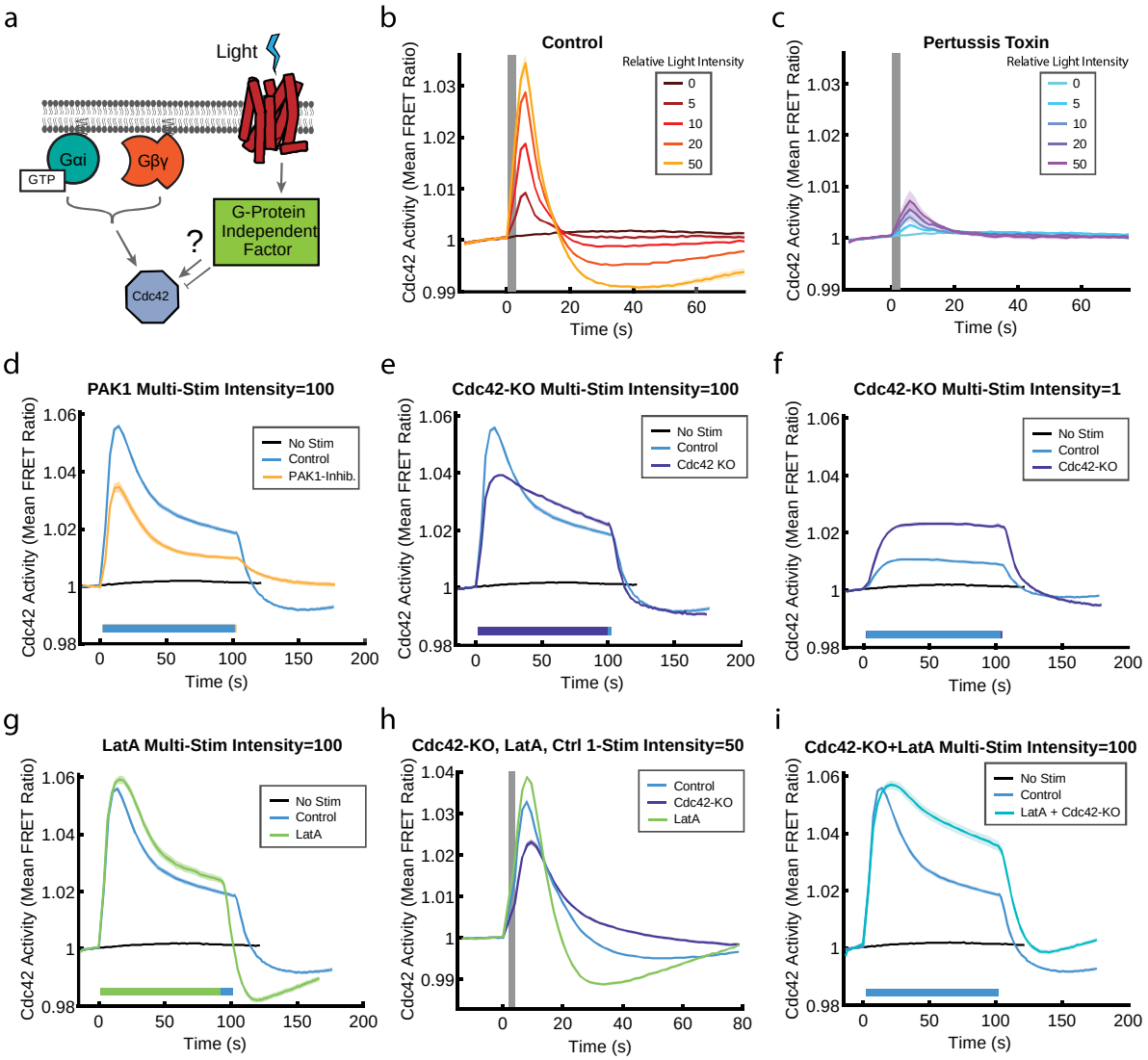

Figure 3.4 Multiple negative signals downstream of G-proteins collaborate to regulate the Cdc42 response.

(**a**) Schematic indicating the potential for Cdc42 response regulation independent of heterotrimeric G-protein signals. (**b-c**) Single pulse stimulations of populations of PLB-985 cells expressing parapinopsina and the Cdc42 TomKat sensor either without (b) or after treatment with 600 ng/ml Pertussis toxin (PTX) to inhibit $G_i\alpha$ dependent signals (c). Shaded error region represents ± s.e.m of $n_{\text{well replicates}}$ = 16 for all conditions. Stimulus duration indicated by gray bar. (**d**) Comparison of Cdc42 responses to prolonged

stimulation with or without treatment with 5 mM PAK1 inhibitor IPA-3. Shaded error region ± s.e.m. of $n_{well\ replicates}$ = 65 for non-stimulated, $n_{well\ replicates}$ = 77 for control, $n_{well\ replicates}$ = 32 for PAK1 inhibited. Relative light intensity =100. Stimulation duration indicated by color bars. (**e**) Comparison of Cdc42 TomKat sensor response measurements under the same conditions for Cdc42-KO cells and control cells. Shaded error region ± s.e.m. of $n_{well\ replicates}$ 65 for non-stimulated, $n_{well\ replicates}$ = 77 for control, $n_{well\ replicates}$ = 56 for Cdc42-KO. Relative light intensity =100. Stimulation duration indicated by color bars. (**f**) Comparison of the responses of the same cell lines to lower power stimulations. Shaded error region ± s.e.m. of $n_{well\ replicates}$ = 65 for non-stimulated, $n_{well\ replicates}$ = 27 for control, $n_{well\ replicates}$ = 16 for Cdc42-KO. Relative light intensity =1. Stimulation duration indicated by color bars. (**g**) Comparison of Cdc42 responses to prolonged stimulation with or without treatment with 1 mM of the actin depolymerizing agent Latrunculin-A. Shaded error region represents ± s.e.m. of $n_{well\ replicates}$ = 65 for non-stimulated, $n_{well\ replicates}$ = 77 for control, $n_{well\ replicates}$ = 32 for Latrunculin-A-treated cells. Relative light intensity =100. Stimulation duration indicated by color bars. (**h**) Comparison of single-pulse stimulation responses for the same conditions as in (g). Shaded error region ± s.e.m. of $n_{well\ replicates}$ = 76 for control, $n_{well\ replicates}$ = 42 for Cdc42-KO, $n_{well\ replicates}$ = 70 for Latrunculin-A-treated cells. Relative light intensity = 50. Stimulus duration indicated by gray bar. (**i**) Comparison of responses for untreated control cells and Cdc42-KO cells treated with 1 mM Latrunculin-A. Shaded error region represents ± s.e.m. of $n_{well\ replicates}$ = 65 for non-stimulated, $n_{well\ replicates}$ = 77 for control, $n_{well\ replicates}$ = 32 for Latrunculin-A + Cdc42-KO cells. Relative light intensity =100. Stimulation duration indicated by color bars.

Figure 5

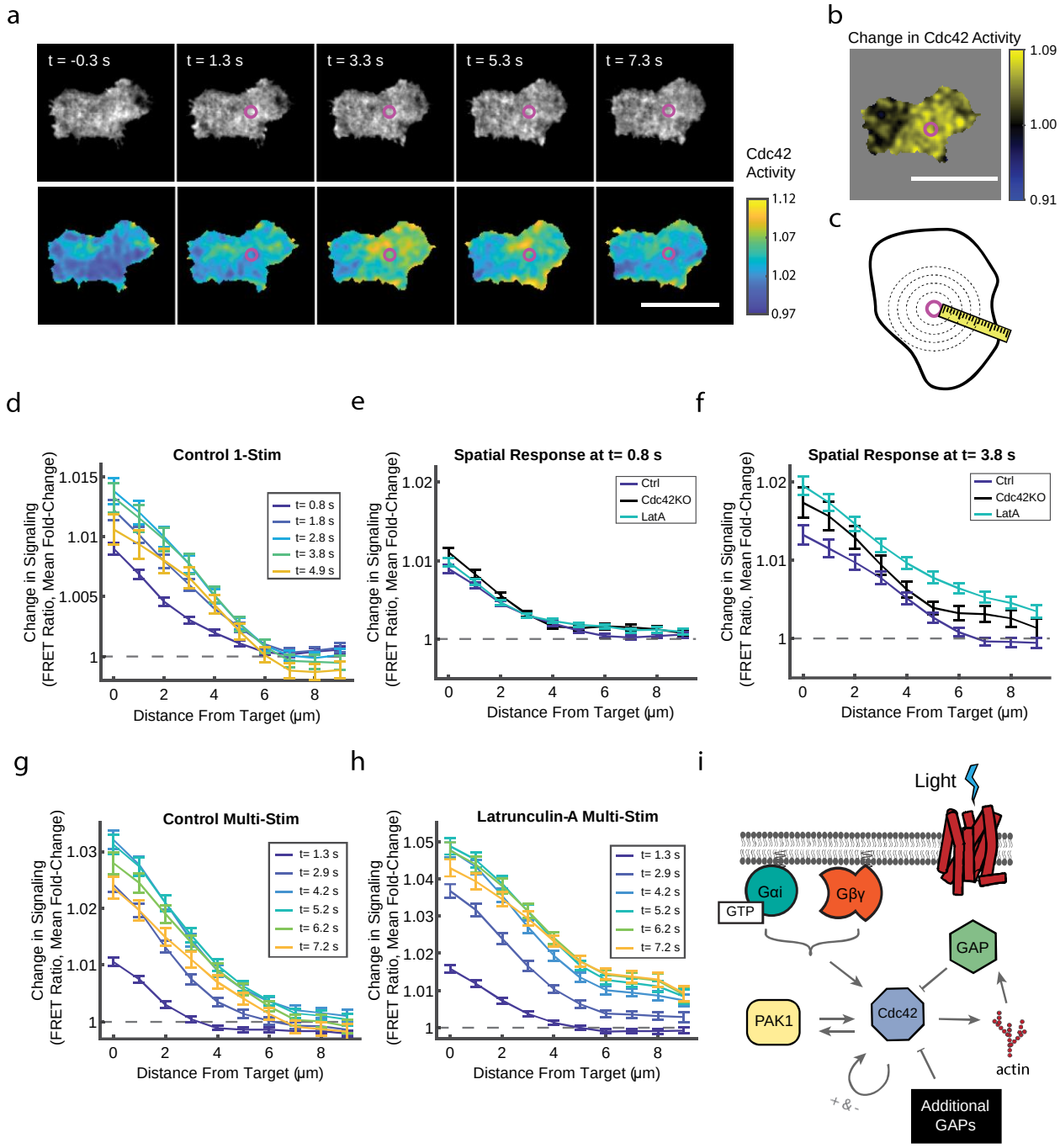

Figure 3.5 F-actin and Cdc42 spatially constrain the spread of signals downstream of receptors.

(**a**) A control cell responding to the center stimulation experiment. A single laser pulse (4.3 μW, 10 ms duration) was applied between frame 1 and 2. Purple circle indicates the stimulation site. Top panel images are the sum of the two FRET channels. Bottom panel images are FRET ratio images. Times

relative to stimulation are indicated. Scale bar, 15 μm. (**b**) The spatial Cdc42 response was calculated as fold-change between the FRET ratio images before and after stimulation (Frame 3 / Frame 1) for the cell shown in (**a**). Scale bar, 15 μm. (**c**) Schematic for center stimulation experiment analysis strategy. Cell pixels were aggregated based on their distance from the stimulus target site (magenta circle) for each frame in the experiment. (**d**) Relative Cdc42 response as a function of distance from the stimulus target site for control cells at the indicated time points. One 0.8 μW light-pulse of 10 ms duration was delivered at t = 0 s. Error bars represent ± s.e.m. of n = 181 cells. (**e-f**) Relative Cdc42 response as a function of distance from stimulus target site for control, Cdc42-KO, and Latrunculin-A conditions at t = 0.8 s (**e**) and t = 3.8 s (**f**) post-stimulation. Error bars represent ± s.e.m. of n = 181 cells for control, n = 67 for Cdc42-KO, n = 175 for Latrunculin-A-treated cells. (**g-h**) Relative Cdc42 responses as a function of distance from the stimulation site for control and Latrunculin-A conditions in response to five sequential 0.8 μW light-pulses of 10 ms duration delivered immediately after successive images, with the first stimulus delivered at t = 0 s. Error bars represent ± s.e.m. of n = 142 cells for control, n = 102 for Latrunculin-A-treated cells. (**i**) Schematic indicating the positive and negative regulators of the Cdc42 response identified in this study.

3.13 Supplementary Information

Supplementary Figure 1

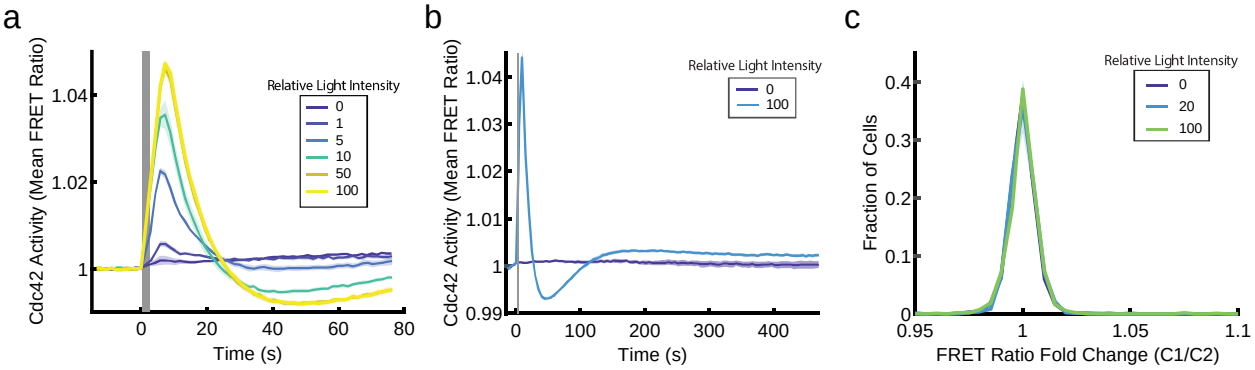

Supplementary Figure 3.1 Dose-dependent positive and negative signals downstream of receptors shape a graded Cdc42 response.

(**a**) Subset of Cdc42-dose response curves, highlighting the graded nature of the Cdc42 response. Shaded error regions represent ± s.e.m. of $n_{\text{well replicates}} = 7$ for each stimulation condition. (**b**) Single stimulation experiment with extended duration captures late phase oscillatory behavior as the Cdc42 response adapts to a baseline level. Shaded error regions represent ± s.e.m. of $n_{\text{well replicates}} = 11$ for each stimulation condition. (**c**) Control for fraction of cells responding to light stimulus strength. Control for FRET ratio fold change was calculated by taking the ratio of the control window (C1) to the control window (C2). Shaded error regions represent ± s.e.m. of $n_{\text{experiment}} = 4$. Across the four experiments, n=4127 cells (relative light intensity = 0), n=2317 cells (relative light intensity = 20), n=2261 cells (relative light intensity =100).

Supplementary Figure 2

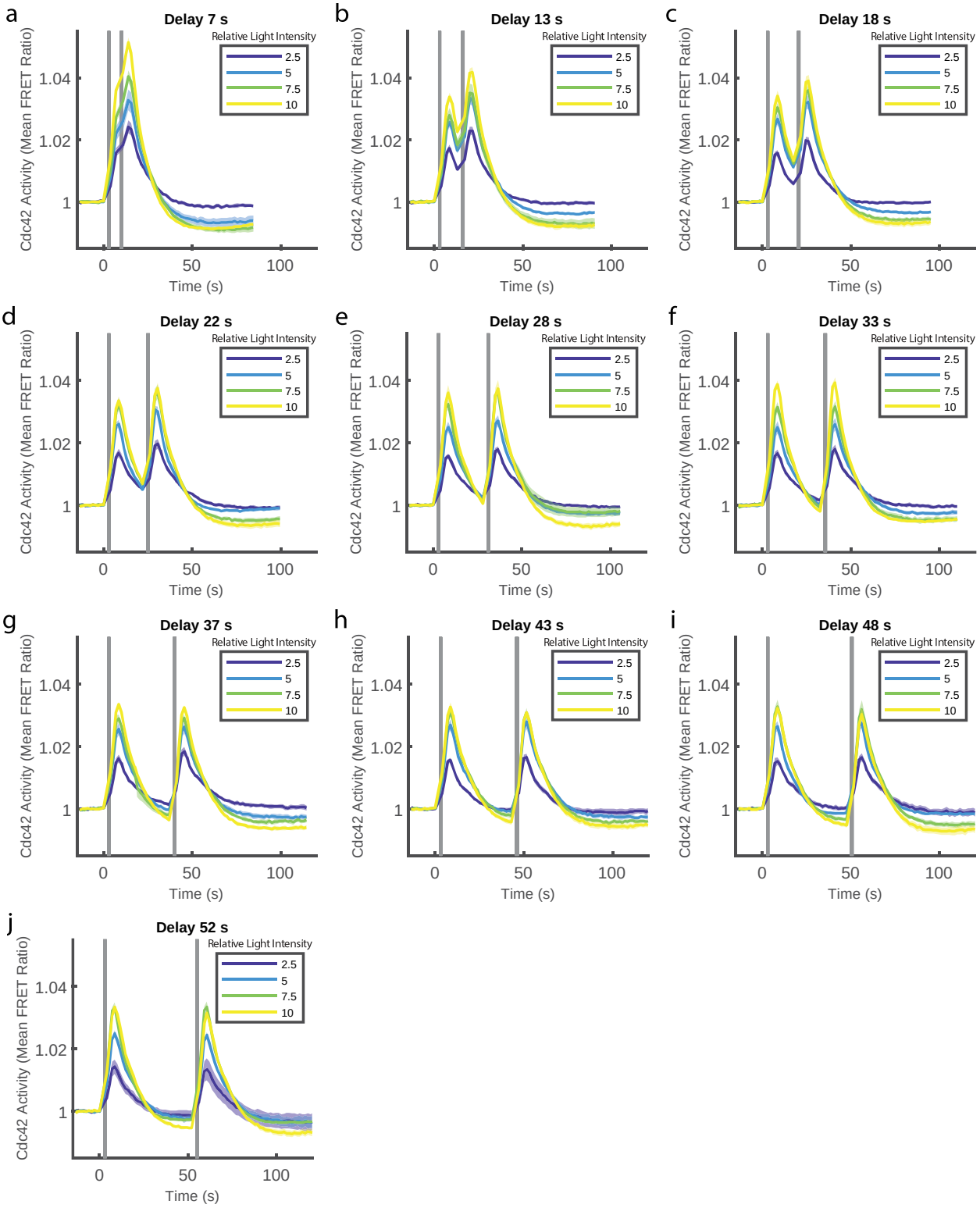

Supplementary Figure 3.2 Responses to sequential stimuli are independent.

(**a-j**) Cdc42 response to two equal duration and light intensity stimulations with varying time delays. (**a**) Shaded error regions represent ± s.e.m. of $n_{well\ replicates}$ = 6 (Relative light intensity = 2.5), $n_{well\ replicates}$ = 6 (Relative light intensity = 5), $n_{well\ replicates}$ = 6 (Relative light intensity = 7.5), $n_{well\ replicates}$ = 30 (Relative light intensity = 10). (**b**) Shaded error regions represent ± s.e.m. of $n_{well\ replicates}$ = 7 (Relative light intensity = 2.5), $n_{well\ replicates}$ = 6 (Relative light intensity = 5), $n_{well\ replicates}$ = 6 (Relative light intensity = 7.5), $n_{well\ replicates}$ = 6 (Relative light intensity = 10). (**c**) Shaded error regions represent ± s.e.m. of $n_{well\ replicates}$ = 30 (Relative light intensity = 2.5), $n_{well\ replicates}$ = 7 (Relative light intensity = 5), $n_{well\ replicates}$ = 6 (Relative light intensity = 7.5), $n_{well\ replicates}$ = 6 (Relative light intensity = 10). (**d**) Shaded error regions represent ± s.e.m. of $n_{well\ replicates}$ = 6 (Relative light intensity = 2.5), $n_{well\ replicates}$ = 30 (Relative light intensity = 5), $n_{well\ replicates}$ = 7 (Relative light intensity =7.5), $n_{well\ replicates}$ = 6 (Relative light intensity = 10). (**e**) Shaded error regions represent ± s.e.m. of $n_{well\ replicates}$ = 6 (Relative light intensity = 2.5), $n_{well\ replicates}$ = 6 (Relative light intensity = 5), $n_{well\ replicates}$ = 30 (Relative light intensity = 7.5), $n_{well\ replicates}$ = 6 (Relative light intensity = 10). (**f**) Shaded error regions represent ± s.e.m. of $n_{well\ replicates}$ = 5 (Relative light intensity = 2.5), $n_{well\ replicates}$ = 5 (Relative light intensity = 5), $n_{well\ replicates}$ = 5 (Relative light intensity =7.5), $n_{well\ replicates}$ = 26 (Relative light intensity = 10). (**g**) Shaded error regions represent ± s.e.m. of $n_{well\ replicates}$ = 5 (Relative light intensity = 2.5), $n_{well\ replicates}$ = 4(Relative light intensity = 5), $n_{well\ replicates}$ = 4 (Relative light intensity = 7.5), $n_{well\ replicates}$ = 4 (Relative light intensity = 10). (**h**) Shaded error regions represent ± s.e.m. of $n_{well\ replicates}$ = 26 (Relative light intensity = 2.5), $n_{well\ replicates}$ = 5 (Relative light intensity =5), $n_{well\ replicates}$ = 4 (Relative light intensity = 7.5), $n_{well\ replicates}$ = 4 (Relative light intensity = 10). (**i**) Shaded error regions represent ± s.e.m. of $n_{well\ replicates}$ = 4 (Relative light intensity = 2.5), $n_{well\ replicates}$ = 26 (Relative light intensity = 5), $n_{well\ replicates}$ = 5 (Relative light intensity = 7.5), $n_{well\ replicates}$ = 4 (Relative light intensity = 10). (**j**) Shaded error regions represent ± s.e.m. of $n_{well\ replicates}$ = 4 (Relative light intensity = 2.5), $n_{well\ replicates}$ = 4 (Relative light intensity = 5), $n_{well\ replicates}$ = 26 (Relative light intensity = 7.5), $n_{well\ replicates}$ = 4 (Relative light intensity = 10).

Supplementary Figure 3

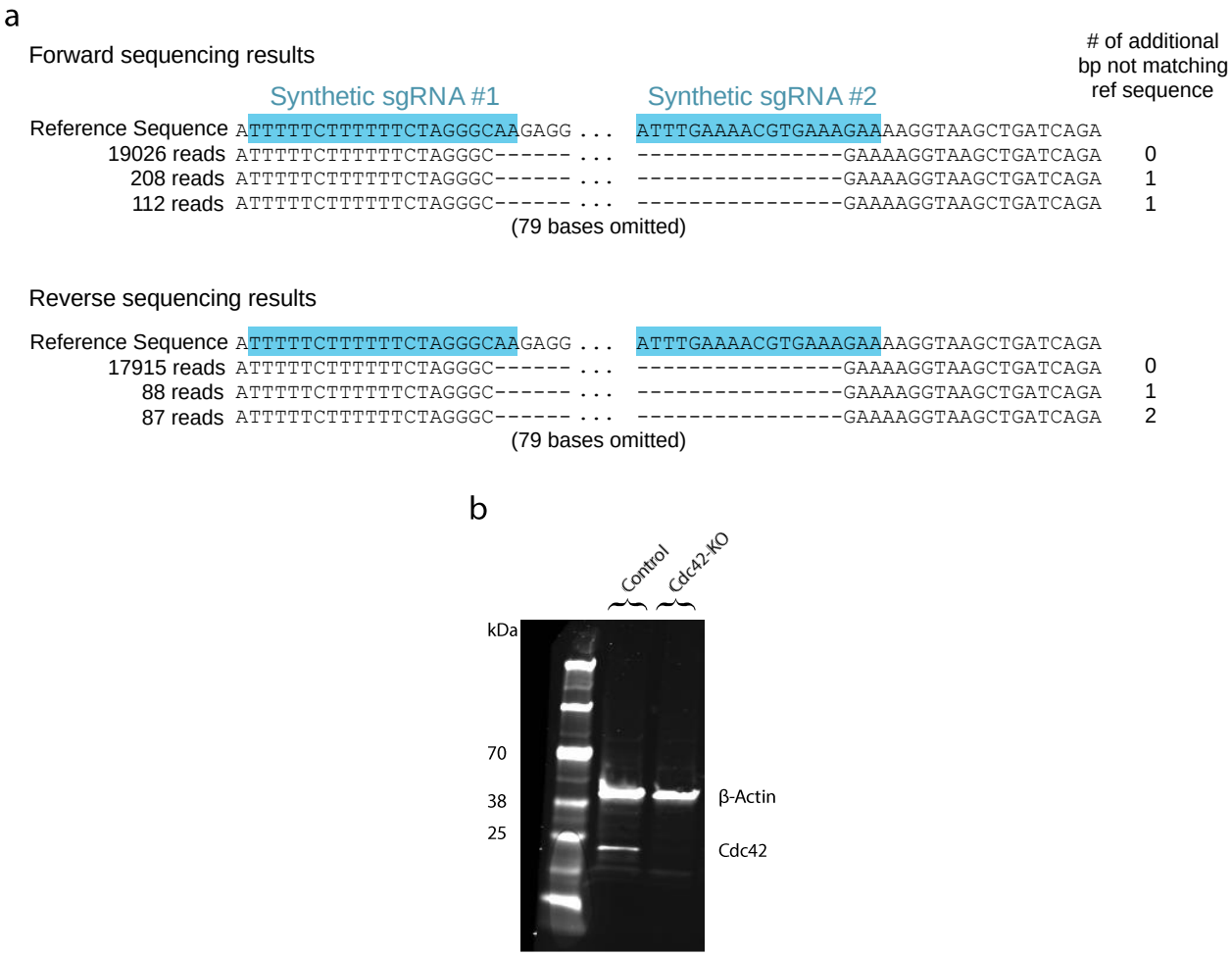

Supplementary Figure 3.3 The Cdc42 knockout is homozygous.

(**a**) Amplicon sequencing results. The dominant sequence was identical for both forward and reverse primers. The single dominant read indicates that the same deletion is present for both alleles. (**b**) Full-lane

western blot. Top bands correspond to an anti-β-Actin antibody while bottom band is reactive to an anti-Cdc42 antibody.

Supplementary Figure 4

a

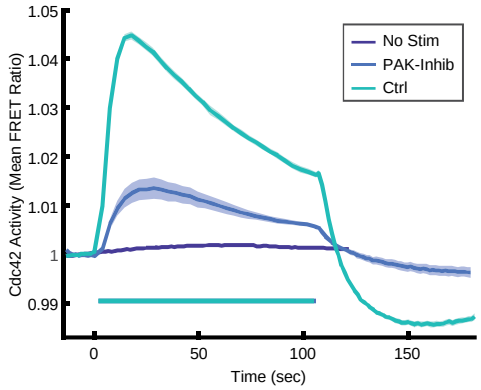

Supplementary Figure 3.4 Inhibition of PAK1 reduces Cdc42 response magnitude regardless of stimulation light power.

(**a**) Control and PAK1-Inhibited cells responding to medium power light stimulation (Relative light intensity = 50). Shaded error region ± s.e.m. of $n_{well\ replicates}$ = 65 for non-stimulated, $n_{well\ replicates}$ = 59 for control and $n_{well\ replicates}$ = 16 for PAK1 inhibited cells.

Supplementary Figure 5

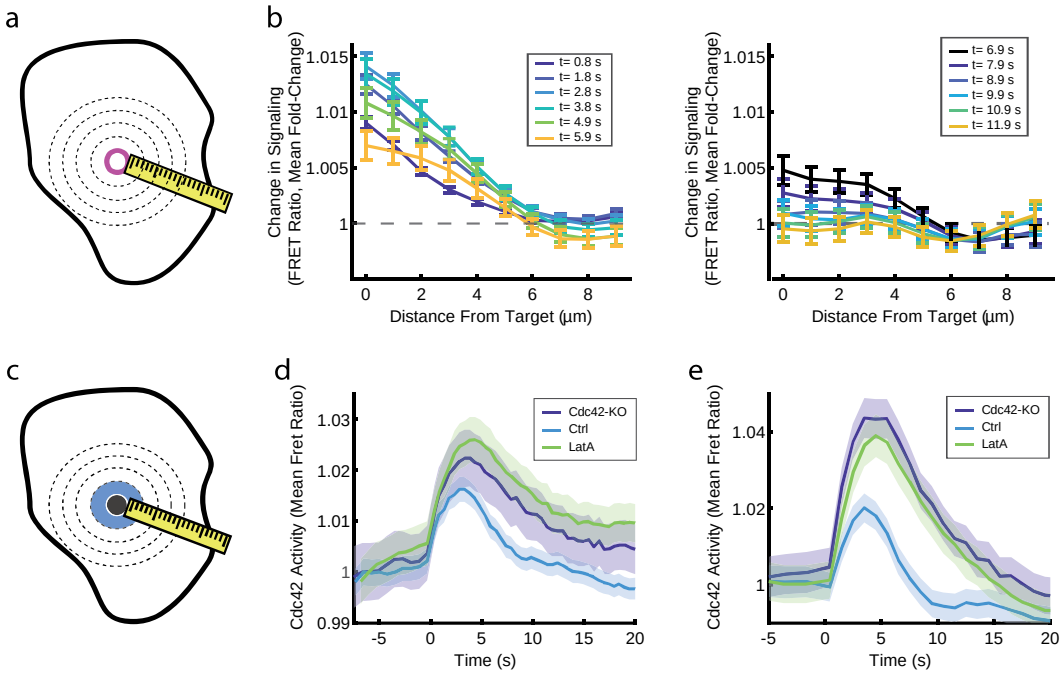

Supplementary Figure 3.5 The Cdc42-KO and Latrunculin-A perturbations prolong the duration of the Cdc42 response.

(**a**) Schematic for center stimulation experiment analysis strategy. Cell pixels were aggregated based on their distance from the stimulus target site (magenta circle) for each frame in the experiment. (**b**) Time course encompassing activation and attenuation of Cdc42 response to single pulse center stimulation experiment. Relative Cdc42 response as a function of distance from the stimulation target site for control cells. The response attenuates by ~10 seconds post stimulation (Right panel). Experimental stimulation condition: one, 0.8 µW light-pulse with 10ms duration. Error bars represent ± s.e.m. of n=181 cells. (**c**) Center stimulation experiment schematic. Pixels < 1µm from the stimulation site (blue shaded region) were used to generate plots in (**d-e**). (**d**) Cdc42 activity as a function of time for control, Cdc42-KO, and Latrunculin-A treated cells responding to one, 0.8 µW light-pulse with 10 ms duration. Error bars represent ± s.e.m. of n=181 cells for control, n=67 for Cdc42-KO, and n=175 for Latrunculin-A. (**e**) Cdc42 activity as a function of time for control, Cdc42-KO, and Latrunculin-A treated cells responding to

one, 4.3 µW light-pulse with 10 ms duration. Error bars represent ± s.e.m. of n=131 cells for control, n=43 for Cdc42-KO, and n=105 for Latrunculin-A-treated cells. responding to one, 4.3 µW light-pulse with 10 ms duration. Error bars represent ± s.e.m. of n = 131 cells for control, n = 43 for Cdc42-KO, and n = 105 for Latrunculin-A-treated cells.

Supplementary Figure 6

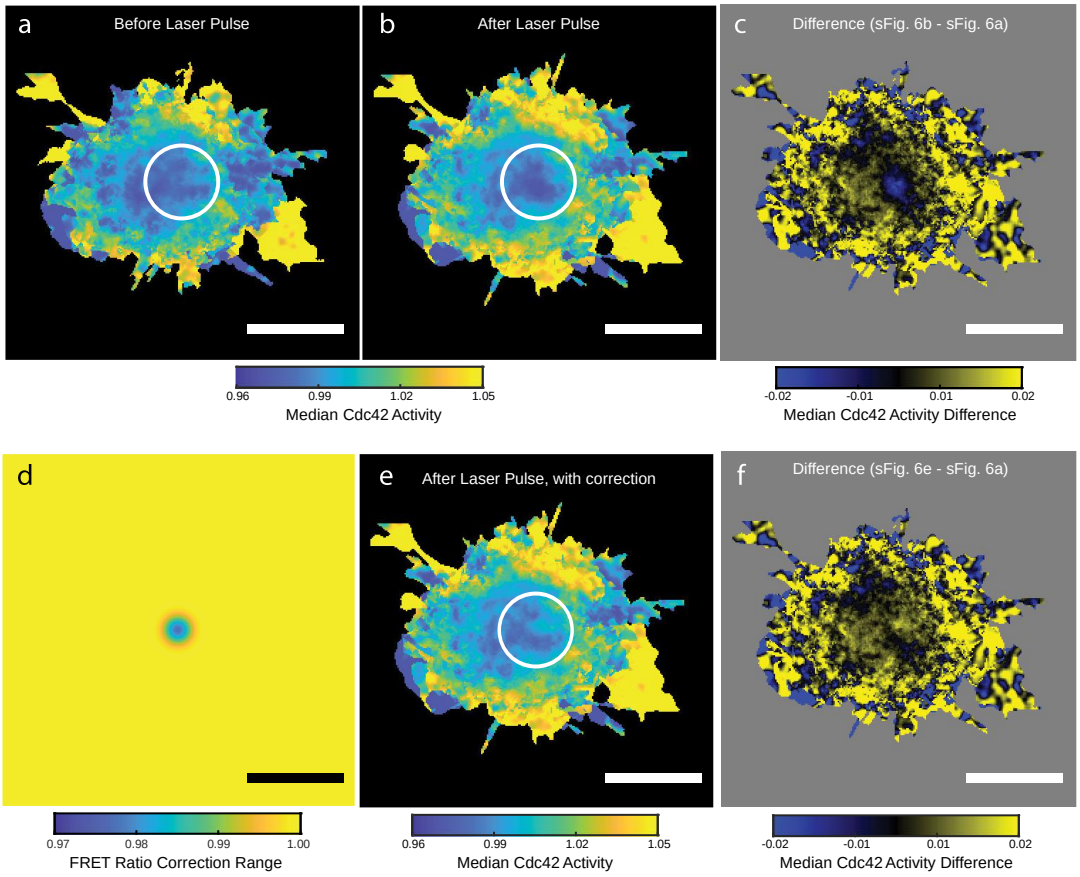

Supplementary Figure 3.6 Photobleaching correction for bleaching due to FRAP laser stimulation.

(**a**-**b**) Median Cdc42 FRET ratio of n = 79 cells for the image immediately preceding (**a**) and succeeding (**b**) stimulation. Cells were stimulated with a strong, 37 µW, 10 ms laser pulse to maximize bleaching for computing the correction. White circles indicate the FRAP target region. Photobleaching causes a reduction in FRET signal (**b**). (**c**) Difference between post-stimulus and pre-stimulus image. (**d**) Photobleaching correction image for the frame immediately succeeding FRAP stimulation. (**e**) Median

Cdc42 FRET ratio of n = 79 cells where the photobleaching correction was applied to the post-stimulation frame. (**f**) Difference between photobleaching corrected post-stimulus and pre-stimulus images. Scale bar for all panels, 15 μm.

Chapter 4

Directional reorientation of migrating neutrophils is limited by suppression of receptor input signaling at the cell rear through myosin II activity

Amalia Hadjitheodorou[1,2], George R. R. Bell[3], Felix Ellett[4], Shashank Shastry[3], Daniel Irimia[4], Sean R. Collins[3,*], and Julie A. Theriot[2,*]

[1]Department of Bioengineering, Stanford University

[2]Department of Biology and Howard Hughes Medical Institute, University of Washington

[3]Department of Microbiology and Molecular Genetics, University of California, Davis

[4]Department of Surgery, BioMEMS Resource Center Massachusetts General Hospital, Harvard Medical School, Shriners Burns Hospital

*For correspondence: jtheriot@uw.edu, srcollins@ucdavis.edu

4.1 Preface

This chapter represents the culmination of a collaborative project with Amalia Hadjitheodorou in the Theriot lab at the University of Washington and the Allen Institute. While I was not the first author, I made significant contributions to experimental design, cell line construction, and developing software for

automated imaging experiments and the image processing pipeline for data analysis. This work is currently under review and is linked to the manuscript in Chapter 3.

4.2 Citation

Hadjitheodorou, A. *et al.* Directional reorientation of migrating neutrophils is limited by suppression of receptor input signaling at the cell rear through myosin II activity. *bioRxiv* 2021.04.04.438336 (2021) doi:10.1101/2021.04.04.438336.

4.3 Author contributions

A.H., G.R.R.B., S.R.C. and J.A.T. designed the experiments, A.H. performed the experiments and analyzed the data, A.H., G.R.R.B. and S.R.C. created software for data analysis and automating experiments, G.R.R.B. and S.R.C. developed the optogenetic and imaging tools, G.R.R.B. and S.S. created the cell lines, F.E. and D.I. designed the microfluidic devices, A.H., S.R.C. and J.A.T. interpreted the data, A.H., S.R.C. and J.A.T. wrote the manuscript. All authors read and approved the manuscript.

4.4 Abstract

To migrate efficiently to target locations, cells must integrate receptor inputs while maintaining polarity: a distinct front that leads and a rear that follows. Here we investigate what is necessary to overwrite pre-existing front-rear polarity in neutrophil-like HL60 cells migrating inside straight microfluidic channels. Using subcellular optogenetic receptor activation, we show that receptor inputs can reorient weakly polarized cells, but the rear of strongly polarized cells is refractory to new inputs. Transient stimulation

reveals a multi-step repolarization process, confirming that cell rear sensitivity to receptor input is the primary determinant of large-scale directional reversal. We demonstrate that the RhoA/ROCK/myosin II pathway limits the ability of receptor inputs to signal to Cdc42 and reorient migrating neutrophils. We discover that by tuning the phosphorylation of myosin regulatory light chain we can modulate the activity and localization of myosin II and thus the amenability of the cell rear to 'listen' to receptor inputs and respond to directional reprogramming.

4.5 Introduction

Neutrophils, the most abundant circulating leukocytes in humans, comprise the first line of innate immune defense. Their directed migration is mediated by detection of chemoattractant such as fMLF via G protein-coupled receptors (GPCRs), fairly evenly distributed on the cell surface[1,2]. Ligand binding to the receptor activates signaling via G_i, leading to cell polarization and directional motility[3].

An early manifestation of neutrophil polarization is the generation of steep antagonistic gradients of Cdc42 and RhoA activity, formed synchronously towards the cell front and rear, respectively[4] (Fig. 1a). At the front, Cdc42 and Rac1 induce actin polymerization, while RhoA regulates myosin II contractility at the rear. The front and rear signaling modules are mutually exclusive[3] and are governed by positive feedback loops for self-amplification and polarity maintenance[5–7]. In addition, tension by the plasma membrane has been demonstrated to act as a long-range inhibitor, mechanically preventing the generation of multiple cell fronts[8].

Once established, front-rear polarity in migrating neutrophils is thought to be relatively stable, as evidenced by the observation that polarized neutrophils often steer their original front to make a U-turn instead of repolarizing, suggesting that neutrophils are more sensitive to chemoattractants towards their front as compared to their rear[1]. To examine the role of polarity in chemoattractant sensing, researchers have historically challenged neutrophils migrating on 2-D planar substrates using point sources of

chemoattractant at different angles with respect to the original direction of migration[3,9–11]. In these experiments, chemoattractant is typically delivered using a micropipette positioned near the cell, resulting in diffusion of the attractant over the entire cellular surface. Thus, it is difficult to decouple whether the rear was intrinsically less responsive to chemoattractant signaling than the front, or whether the greater amplification of signaling inputs at the cell front gave it the advantage. Recent studies have leveraged microfluidic devices, examining the response of neutrophil-like HL60 cells and *Dictyostelium* cells to flipping the direction of the chemoattractant gradient when cells are confined in 1-D channels and cannot physically perform a U-turn[12,13].

To probe the cellular sensitivity to receptor inputs at the level of signaling, and to determine what is necessary to overwrite front-rear polarity, we used an optogenetic approach to locally activate $G_{\alpha i}$ signaling, independent of fMLF, and drive cells to dynamically repolarize without modifying the environment in which they are embedded. We found that persistent optogenetic receptor activation at the rear of neutrophils migrating in 1-D microfluidic channels is sufficient to reorient weakly polarized and slowly migrating cells. However, in more strongly polarized cells, myosin II and RhoA activity limit the ability of the rear to respond, even at the level of signal transmission to Cdc42, creating a cell rear that is refractory to new receptor inputs. We show that by tuning the phosphorylation of myosin regulatory light chain, we can modulate the activity and localization of myosin II and thus the amenability of the cell rear and the ability of cells to reverse their direction of motion.

4.6 Results

Persistent optogenetic stimulation is sufficient to reverse weakly polarized and slowly migrating cells

We generated a neutrophil-like HL60 cell line stably expressing parapinopsin (a light-sensitive $G_{\alpha i}$-family GPCR) and a tdTomato/tdKatushka2 Cdc42 FRET biosensor, spectrally compatible with the reversible parapinopsin stimulation. This system allows direct recording of downstream Cdc42 activity in

cells whose migration is guided by parapinopsin[14]. We confined cells to migrate inside 1-D straight microfluidic channels in response to spatial serum gradients (Fig. 1a). Using a 407 nm laser, we locally stimulated cells with 10 ms light pulses and the spatial precision of about a 1 μm diameter spot, using real-time image analysis to automatically and dynamically position the activation spot at the appropriate location (see Methods). We found that repeatedly delivering light pulses every 3 s at the cell rear was sufficient to overwrite the front-rear polarity, drive a chemotaxis-like response on the level of Cdc42, and ultimately reverse the direction of motion in a subset (about 47%) of cells (Fig. 1b & Movie S1).

We were initially surprised by the observation that just 47% of cells reversed (Fig. 1c). To better understand why only some cells were able to reverse direction, we first used flow cytometry to measure the mCitrine-tagged parapinospin receptor (abbreviated as mCit on Fig. 1a) and found that over 97% of cells expressed the construct (Supplemental Fig. 1a). We next confirmed that at least 70-93% of cells were responsive to a 5-pulse optical stimulation administered at their center (Supplemental Figs. 1b-1c & Movie S2). These estimates of inherently responsive cells were significantly higher than the 47% of reversing cells, suggesting that the reversals were suppressed due to some other kind of variation among cells.

We then examined whether there were any measurable pre-stimulation differences between reversing and non-reversing cells. Reversing cells tended to be weakly polarized (Figs. 1d-1e), and slower migrators (Fig. 1f), although there was considerable overlap between the distributions of reversing and non-reversing cells. The primary determinant of reversibility came from the cell rear (Supplemental Fig. 2a-2c). Mean front/rear Cdc42 activity ratio appeared to correlate with centroid speed (Fig. 1g). We found no correlation between a cell's position along the channel or a cell's differentiation age and its likeliness to repolarize upon stimulation (Supplemental Figs. 2d-2e).

All together our analysis suggested that pre-existing variations in cell state could be influencing the ability of the cell to respond to new receptor inputs, and that the amenability of a cell to reverse polarity may be tunable by the sensitivity of the cell rear.

In reversing cells Cdc42 activation at the stimulated rear begins immediately and cells reverse their direction of migration before Cdc42 activity flips polarization

To gain further insight into what may be controlling the rear sensitivity to receptor inputs, we studied the stepwise order of events during optogenetic-driven cell reversals. We quantified the Cdc42 activity at the original rear and front for 78 reversing cells (Fig. 2a) as well as the derivative of Cdc42 activity at each edge (Fig. 2b). Notably, Cdc42 activity began to increase at the stimulated rear almost immediately, whereas the decrease in Cdc42 activity at the old front had a much slower onset. Most strikingly, the direction of migration flipped 27 s post-stimulation (Fig. 2c), considerably before the two cell edges reached equal levels of Cdc42 activity (Cdc42 cross-point) 51 s post-stimulation. Thus, the cell edge that has more Cdc42 activity is not necessarily the driving front.

Moreover, as the stimulated original rear began to increase local Cdc42 activity, the two cell edges pulled in competing directions, causing the normalized cell length to increase and peak 45 s after the initiation of stimulation (Fig. 2d), temporally close to the Cdc42 cross-point. The normalized cell area remained constant during this tug-of-war between the original and emerging front (Fig. 2d). We conclude that the stimulated rear quickly assumed front character and started to move towards the opposite direction, before the signal was transmitted to the original front. In other words, flipping polarity was not instantaneous, as flipping a switch, but was a multistep transition.

The above order of events was also evident in single cells (Fig. 2e-2f). Phase diagrams of mean centroid speed versus mean rear/front Cdc42 activity ratio (Fig. 2g) and of mean rear versus mean front Cdc42 activity (Fig. 2h) further illustrated the transitional states a cell occupied before flipping its polarity and resuming a new steady state (Fig. 2i). This analysis confirmed that Cdc42 activity at the stimulated rear rose quickly, and only after the Cdc42 activity at the original rear got quite high did the Cdc42 activity at the original front start decreasing.

Transient stimulation reveals a variety of distinct cellular responses

Surprised by the observation that cells reversed their direction of migration before Cdc42 activity flipped polarization, we asked what would happen if we stopped the stimulation in between these two key events, namely after the cell stalling at 27 s and before the Cdc42 cross-point at 51 s. We found that transient 12-pulse stimulation resulted in four distinct classes of observed cellular responses that manifested differently on the level of Cdc42 activity with distinct migration patterns (Fig. 3a & Movie S3). 56% of cells showed no measurable response, maintaining their original speed and showing no or minimal rise (<2%) in Cdc42 activity at their rear despite the stimulation. 21% of cells showed some increase of Cdc42 activity at their rear (>2%) but no engagement of the front which appeared strongly polarized and unyielding, resulting in only cell rear elongation. We termed this class "medium response". 7% of cells exhibited a "strong response", transiently flipping their direction of motion, but with Cdc42 polarity and migration reverting back to their original polarization post-stimulation. The remaining 6% of cells reversed. Transient stimulation was significantly less effective in overwriting polarity and reorienting cells as compared to persistent stimulation (6% instead of 47% reversing cells, respectively; Fig. 3b). Notably, the fraction of non-responding cells in the 12-pulse assay was comparable to the fraction of cells that did not reverse upon persistent stimulation (56% and 53%, respectively Fig. 3b). This suggests that cells forming the medium and strong response classes may represent cells with pre-existing conditions that permitted responsiveness and repolarization, but required greater stimulus inputs to completely reverse direction.

We asked whether we could identify any pre-stimulation variations among cells that exhibited these distinct responses. We found that strong responding and reversing cells were slower migrators with weaker polarization than cells that showed no or medium response (Supplemental Fig. 3a and Fig. 3c). Non-responding cells had the strongest rears (i.e. lowest rear-localized Cdc42 activity) among all classes (Supplemental Figs. 3b-3c). Lastly, front Cdc42 activity was higher in medium compared to strong

responding cells (Supplemental Fig. 3d), whose front eventually yielded to the original rear and transiently repolarized.

One possible explanation for why strong responding cells regained their original polarity orientation is that the pre-existing serum gradient might flip back their polarity axis after we switched off the optogenetic stimulus. We therefore examined what would happen if we performed similar experiments for cells moving through channels in a uniform serum environment instead of a gradient, but found no significant differences (Supplemental Fig. 3e), indicating that detection of the pre-existing serum gradient cannot explain why strong responding cells reorient back toward their original direction of motion after optogenetic stimulation ceases. In addition, no significant differences were found when comparing pre-stimulation polarization states of cells migrating in a uniform serum environment versus a gradient (Supplemental Figs. 3f-3j).

A strong cell rear is refractory to receptor inputs

We quantified the average centroid speed traces for the four different classes, namely no response, medium response, strong response and reversed (left to right Fig. 4a), as well as the magnitude and derivative of the Cdc42 activity at each edge (Figs. 4b-4c). The derivative revealed a key difference between the cells in the strong response and the reversed classes. The original rear of strong responding cells showed both a strong positive response to the initiation of stimulation and a prominent negative overshoot post-stimulation (black arrow on the third panel of Fig. 4c). In contrast, reversers showed a lower positive response and no overshoot. Simply put, a cell that overreacted when the stimulation commenced would also overreact when it stopped, emerging as a strong responder. This combination of positive and negative regulation of Cdc42 downstream of receptors was also documented in cell-wide optogenetic stimulation experiments and may reflect temporal processing of input signals[14].

Finally, average kymographs for the four distinct cellular responses compactly summarized on a whole-cell level the dynamic spatiotemporal response of Cdc42 activity in each cell class (Fig. 4d). The kymographs further highlighted our most surprising observation: that a strong rear can be refractory to receptor inputs, even at the level of signal transmission to Cdc42. In contrast, there was a clear trend in which a weaker rear can be amenable to receptor input and lead to a measurable whole-cell response. The migratory and signaling responses were qualitatively similar regardless of whether a serum gradient was present (Fig. 4 and Supplemental Fig. 4). Overall, our observations reveal that the strength of the rear is key in modulating the magnitude of the behavioral response, raising the question of what tunes the rear's strength in the first place.

The phosphorylation of myosin regulatory light chain tunes the amenability of the rear to respond to receptor inputs

We sought to explore what molecular pathways might be actively suppressing the rear response to receptor inputs. We considered two main candidates: i) myosin II/RhoA and ii) ERM (ezrin, radixin, and moesin) proteins/cortical actin.

Myosin II and RhoA signaling have been extensively shown to limit membrane protrusion at the cell rear antagonizing front polarity signaling[3,15,16]. Myosin motor activity and myosin filament assembly are regulated by the phosphorylation of Ser19 and Thr18 on the myosin regulatory light chain (MRLC)[17–19]. Phosphorylation of MRLC in Dictyostelium discoideum has been shown to regulate stable polarity and the ability of the cell to form new lateral protrusions[20]. RhoA activates Rho-associated kinase (ROCK) which directly phosphorylates MRLC and inhibits the phosphatase PP1 with its regulatory myosin-binding subunit MYPT1[21] (Fig. 5a). ROCK inhibition with Y27632 decreases MRLC phosphorylation[22,23]. Moreover, microtubules have been demonstrated to regulate MRLC phosphorylation by sequestering GEF-H1, a guanine nucleotide exchange factor of RhoA, in various cell types[24–27]. In neutrophils, microtubule

destabilization results in activation of RhoA, hyperphosphorylation of MRLC and enhanced myosin contractility[23,28]. Consequently, if the amenability of the cell rear to respond to receptor inputs is modulated by myosin II/RhoA activity we would expect that Y27632 treatment would reduce the antagonistic effect of myosin II/RhoA and make the rear more amenable to optogenetic reprogramming. Conversely, nocodazole treatment, shown to globally increase RhoA activity and MRLC phosphorylation[23,29,30], would be expected to further enhance the strength of the back polarity module, thus suppressing cell rear response.

ERM proteins have also been implicated in cytoskeletal remodeling and cell migration[31,32]. ERM proteins transition between an inactive/closed configuration in the cytosol and an active/phosphorylated form that links cortical actin to the plasma membrane[33] (Fig. 5b). Evidence suggests that the ERM protein moesin in its active/phosphorylated form is a key player in neutrophil polarization inhibiting the small GTPases Rac, Rho, and Cdc42 as well as protrusion at the cell rear[34]. Additionally, the persistence of directional migration of neutrophil-like cells towards fMLF gradients has been proposed to depend, at least in part, on the polarization of ERM proteins and moesin towards the cell rear[12]. Specifically, treatment of neutrophils with NSC668394, a quinoline that inhibits ezrin phosphorylation at Thr567 and ezrin-actin binding, has been shown to result in a considerable reduction of directional memory[12]. The above observations made NSC668394 a key perturbation to assess the involvement of ERM proteins in creating a refractory cell rear. Overall, we found that NSC668394 had no significant effect, while Y27632 and nocodazole had highly significant and opposite effects (Fig. 5c), suggesting that the dominant effect on the rear sensitivity is the myosin II/RhoA pathway rather than through ERM proteins.

Specifically, treating cells with Y27632 reduced the number of cells in the non-responding class (Fig. 5c), consistent with what we expected from our hypothesis that myosin II/RhoA could modulate the responsiveness of the rear. Interestingly, the non-responders decreased in number by almost 2-fold as compared to control, the medium responders increased marginally (1.3-fold), and the strong responders and reversers increased by 1.8-fold and 2.3-fold, respectively. The strong and the reversed classes gained more than what would be expected from just depleting the non-responders, suggesting that the Y27632 treatment

pushes each cell along the response distribution rather than simply suppressing one particular class. Thus, Y27632 is likely not only making the rear more amenable to optogenetic inputs but also may act on a whole-cell backness component. Consistent with these results, Y27632 treatment also increased the percentage of reversing cells in response to persistent stimulation (Fig. 5d).

In contrast, nocodazole treatment resulted in a striking 1.6-fold increase of the no response class as compared to control (Fig. 5c). Medium responding cells decreased by 3.6-fold, and no cells under this condition exhibited a strong response, whilst the fraction of cells that reversed was comparable that in the control case. Nocodazole's effect of increasing the fraction of non-responders was exactly what we expected as the converse of the Y27632 finding, further strengthening the evidence of a role for MRLC phosphorylation in tuning the responsiveness of the rear to receptor inputs.

In addition, average kymograph representation of the Cdc42 activity for the tested perturbations showed a consistent trend: non-responding cells were strongly polarized, whereas cells that showed some kind of response were progressively (from medium, to strong, to reversed) more and more weakly polarized (Figs. 5e-5g).

Myosin II suppresses cellular reorientation and redistributes more slowly than the Cdc42 activity response

Overall, our results pointed to a model in which MRLC phosphorylation regulates the rear response to receptor inputs. In order to visualize myosin dynamics in optogenetic-driven reversals, we generated an HL60 cell line stably expressing fluorescently-tagged MRLC (Myl9-mScarlet) and parapinopsin. We found that the myosin line exhibited a higher percentage of non-responding cells as compared to the Cdc42 line (Fig. 6a). Using flow cytometry, we confirmed that all cells expressed the parapinopsin construct (Supplemental Fig. 5a). This observation led us to hypothesize that the over-expression of MRLC might

itself suppress cellular response, consistent with a causative role for myosin II activity in creating a refractory rear.

Myosin was polarized to the rear of cells in each response class, but with varying degrees of polarization (Fig. 6b and Supplemental Fig. 5b, also Movie S4). The average centroid speed traces for the four classes (Fig. 6c) were qualitatively identical and temporally close to the ones computed from the Cdc42 line (Fig. 4a), allowing us to draw direct comparisons between Cdc42 activity and myosin dynamics.

We quantified the subcellular normalized myosin II localization for cells in each response class and found that myosin relocalization lags behind Cdc42 activity response (Fig. 6b), suggesting that Cdc42 activity is a faster representation of polarity change. Furthermore, the derivative of the normalized myosin at each edge reveals the same key difference we observed on a Cdc42 activity level between the strong and the reverse response (black arrow on the third panel of Fig. 5e). That is, strong responding cells "overreact" both at the onset and the end of stimulation compared to reversing cells.

Finally, average kymographs of intracellular myosin II further illustrated how myosin over-expression seemed to bias cell behavior, with non-reversing cells having higher myosin levels (Supplemental Fig. 5c). This trend was also captured by comparing the averaged pre-stimulation myosin signal over the entire cell body (Supplemental Fig. 5d). Importantly, the difference was not just in the overall myosin expression level but also in its subcellular distribution, reflecting stronger asymmetry in myosin activity. We quantified the pre-existing subcellular myosin localization (Supplemental Figs. 5e-5g) and found a larger accumulation of myosin at the rear of non-responding cells (Supplemental Fig. 5e). Overexpression may result in increased contractile activity and steeper myosin polarization, rendering the cell rear more refractory to receptor inputs.

The phosphorylation of myosin regulatory light chain alters the intracellular localization of myosin II and modulates the receptiveness of the rear to respond

Treating the myosin cell line with Y27632 and nocodazole revealed the same trends as noted before with the Cdc42 line: Y27632 significantly reduced the percentage of non-responding cells as compared to control, whereas nocodazole greatly increased it (Fig. 7a). Y27632 treatment significantly increased the percentage of reversing cells both in response to 12-pulse (Fig. 7a) and persistent stimulation (Supplemental Fig. 6a). Notably, the proportion of myosin-expressing non-responding cells was higher in all conditions as compared to the Cdc42-expressing cells under the respective treatment conditions, consistent with the hypothesis that the myosin line is less amenable to input simply due to overexpression of the fluorescently-tagged MRLC.

We confirmed that drug perturbations were not affecting myosin expression (Supplemental Fig. 6b). However, the perturbations had measurable effects on subcellular myosin distribution, as quantified by front/rear myosin ratio (Fig. 7b), normalized front (Fig. 7c), rear (Fig. 7d) and middle myosin (Supplemental Fig. 6c), as well as cellular speed (Supplemental Fig. 6d). Y27632 greatly suppressed rear myosin as compared to the control and increased the normalized front myosin, resulting in a more symmetric myosin distribution. Acting opposite, nocodazole dramatically increased rear myosin and suppressed the front myosin pool. Average kymographs of myosin II for Y27632- and nocodazole-treated cells (Figs. 7e-7f, respectively) and kymographs of the difference between each drug treatment and the control confirm the above (Supplemental Fig. 6e-6f). In other words, nocodazole amplifies the myosin distribution asymmetry; whereas Y27632 eliminates it to a great extent. Notably, even upon Y27632 treatment 43% of tagged MRLC-expressing cells were not responsive, suggesting that ROCK-regulated myosin activity and asymmetry, while being a strong predictive component, is not exclusively regulating the rear responsiveness.

4.7 Discussion

In this study we demonstrated a causative role for myosin II and RhoA activity in creating a stabilized cell rear that is refractory to receptor inputs. We showed that the asymmetric localization of myosin II, being a readout of myosin activity, correlates with the strength of the rear, and that increased myosin II in the cell rear suppresses responsiveness to receptor inputs. Simply put, the higher the myosin levels and the greater the asymmetry, the more likely cells are to be non-responsive. Furthermore, we found that Y27632 and nocodazole perturbations, acting in opposite directions of the RhoA/ROCK/myosin II pathway (through decreasing and increasing the phosphorylation of MRLC, respectively), tune the rear's ability to respond to new receptor inputs and reorient migrating neutrophils.

Our results extend a longstanding model that antagonism between "frontness" and "backness" activities stabilizes polarity and causes asymmetric responses to receptor inputs. However, it had been difficult to distinguish whether this asymmetry was due to feedback-based competition between front and back programs or interference with signal transmission from receptors. Our approach allowed us to surgically examine the latter hypothesis by activating receptors only in the rear of cells without perturbing the cell front in a constrained environment. Rather than simply limiting the ability of new inputs to develop a fully functional front and reverse the cell, we found that a high level of myosin II activity at the cell rear was capable of blocking any detectable response downstream of receptors at the level of Cdc42 activity, in many cells.

For cells that maintain persistent polarity, like neutrophils, there are several models describing how long-range communication underlying directional decisions might occur. A long-standing model in the field, abbreviated as LEGI (local-excitation-global-inhibition), suggests that, in addition to generating local protrusive signals, receptor activation also generates a chemical long-range global inhibitor to suppress protrusion at distant sites. The sequence of repolarization events described in Fig. 2 reveal that the stimulated cell rear quickly assumed front character and the long distance effects did not appear to be transmitted to the previous cell front until the cell was physically stretched. Our results are consistent with

a simple mechanical coupling between the two cell edges[8], without the need to invoke an additional LEGI-type chemical signal.

In addition, through transient optogenetic stimulation we discovered a particularly interesting class of cellular response, where cells transiently changed direction of motion and repolarized their Cdc42 activity and myosin but reverted back to their original polarity after stimulation ceased. This strong response is reminiscent of a previously documented cellular behavior in which a subset of neutrophil-like cells retained their directional memory after the removal and later re-introduction of external fMLF chemotactic environment[12]. This directional memory was in part associated with ERM protein moesin, as inhibition through NSC668394 reduced this behavior. In our assay, treatment with NSC668394 did not result in a similar suppression of strong responding cells. This leads us to believe that the strong response in our assay is primarily resulting from the sensitivity to signal onset and removal we previously described. We note that nocodazole treatment resulted in no strong responding cells, which may suggest that microtubules or RhoA confer some biochemical memory of the original polarity. Decoupling a role for microtubules from RhoA is particularly complicated because of the known effect of microtubules to regulate MRLC phosphorylation by sequestering GEF-H1, such that microtubule destabilization triggers activation of RhoA, enhancing myosin II contractility[23,28]. However, nocodazole treatment also resulted in a dramatic increase in the fraction of non-responding cells, making it difficult to distinguish effects on biochemical memory from the general suppression of rear responsiveness.

Finally, by directly measuring Cdc42 activity in optogenetic-driven reversals of cells migrating inside 1-D channels, we discovered that the direction of motion flipped before the polarity of Cdc42 activity flipped. In other words, it is not always the cell edge with more Cdc42 activity that defines the migratory direction. Our analysis may reflect neutrophils also engaging temporal-sensing mechanisms, evaluating how Cdc42 activity dynamically changes at each edge, rather than just comparing absolute or relative magnitudes of activity to dictate cytoskeletal polarization and ultimately migratory direction. A subtle point here is that although Cdc42 is a primary regulator of cell direction and formation of protrusive fronts in

neutrophil-like cells[4], there may be other components that could change faster. Nevertheless, evidence of temporal signal processing has also been shown in neutrophil-like cells when confined to migrate in a 2-D plane under agarose[14], in primary neutrophils upon fast switching of chemoattractant gradients[35], and in myeloid cells whose persistent migration to certain intermediate chemokines involves temporal sensing[36].

Historically, the cytoskeleton has usually been perceived as an effector operating downstream of signaling due to receptor inputs. However, growing evidence highlights that the system can also work the opposite way around, with the cytoskeleton critically influencing receptor activity[37]. Our findings strongly support this more complex view (Fig. 8), revealing a new dimension of the interplay between the cytoskeleton and signal transduction.

4.8 Methods

Generation of HL60 cell lines stably expressing parapinopsin-Cdc42 FRET sensor and parapinopsin-Myl9

Zebrafish parapinopsina and Cdc42 Tom/Kat FRET sensor plasmids were cloned as previously described[14] HL60 cell lines were generated by using the 2nd generation lentiviral system to stably insert the parapinopsina gene. Next, the Cdc42 FRET sensor was stably integrated using the piggybac transposon system[38]. The sensor plasmid was co-electroporated at a 1:1 ratio with the piggybac transposase plasmid using the Neon electroporation transfection system (Thermo Fisher Scientific). We used pulse voltage 1350 V and pulse width 35 ms.

The myosin light chain plasmid was generated using multi-part Gibson cloning where iRFP670 fluorescent protein (to enable cytosolic segmentation), a tandem P2AT2A element and mScarlet-I fused to Myl9 were inserted into a lentiviral vector. The plasmid and plasmid maps will be made available on Addgene for the published version of this manuscript. The myosin construct was then stably inserted using

the lentiviral system. HL60 cells expressing the myosin construct were selected using 10 µg/ml blasticidin (Corning 30-100-RB). The line was sorted for cells highly expressing the myosin light chain (mScarlet-I), and cytoplasmic iRFP670 using a Beckman Coulter Astrios EQ at the UC Davis Flow Cytometry Core Facility.

Cell culture and differentiation

HL-60 cells were cultured and differentiated into a neutrophil-like state as previously described[39]. Briefly, cells were cultured in RPMI 1640 plus L-glutamine and 25 mM HEPES media (Gibco RPMI 1640 Medium, HEPES, Thermo Fisher Scientific), supplemented with 10% heat-inactivated fetal bovine serum (hiFBS) (Foundation Fetal Bovine Serum, Gemini Bio, heated in a water bath for 40 min at 56 ºC to inactivate), 100U/mL penicillin, 10 mg/mL streptomycin, and 0.25 mg/mL Amphotericin B (Gibco Antibiotic-Antimycotic, Thermo Fisher Scientific). Cells were maintained at 37 ºC and 5% CO2 in a tissue culture incubator and were passaged every day so as to maintain a cell density close to $5x10^5$ cells/mL. Cell differentiation was achieved by diluting cells in the complete RPMI media at a starting density of $2x10^5$ cells/mL and spiking 1.3% DMSO (Acros 61097). Experiments were performed with cells differentiated for 6 or 7 days.

Flow cytometry measurements of mCitrine-tagged parapinopsin expression

We used flow cytometry to measure the mCitrine-tagged parapinospin receptor in the Cdc42- and myosin II-expressing HL60 cell lines. Roughly $5x10^5$ cells were centrifuged at 200 RCF for 5 min, and resuspended in ice-cold FACs buffer (Phosphate buffered saline (PBS) + 5% FBS +0.01% sodium azide). Next, cells were analyzed using a Becton-Dickinson (BD) FACSCanto II Flow Cytometer. Cells were gated using a polygonal FSC versus SSC gate, to gate for viable cells. The gate was drawn manually to best

separate the distinct two populations. A threshold for "positive" presence of mCitrine was manually set at 10^3 to separate the two peaks in a clearly bimodal distribution across samples.

Microfluidic device fabrication

Microfluidic devices were prepared as previously described[40]. They consisted of a cell loading channel of 200 µm height and 200 µm width bordered on one side by an array of straight, 944 µm long migratory channels of 6 µm width and 3 µm height. Migration channels were arrayed in groups of three, each triplet connecting to a common 4 nL volume reservoir.

Devices were fabricated using photolithography and soft-lithography approaches. Briefly, photolithography masks were designed using AutoCAD software (Autodesk) and provided in chrome on glass by Front Range Photomask (Lake Havasu City, AZ). The master wafer was prepared by sequentially spin-coating the wafer with two layers of SU-8 negative photoresist (Microchem, Newton, MA) and patterning by exposure to UV light through the two chrome masks. Two cycles were carried out to produce the migration channels at 3 µm height and the loading channels and reservoirs at 200 µm height. To fabricate polydimethylsiloxane (PDMS) devices, the master wafer was used as a replica mold for soft lithography. PDMS (Fisher Scientific, Fair Lawn, NJ) was mixed thoroughly with a curing agent at a ratio of 10:1, poured over the master wafer, then degassed for 1 h prior to curing in an oven at 75 ºC overnight. Once cooled, PDMS devices were cut from the master wafer and the inlets and outlets punched using a 1 mm biopsy punch (Harris Uni-Core, Ted Pella Inc. Redding, CA). Following treatment with oxygen plasma, devices were then bonded irreversibly to 35 mm glass-bottomed (No. 0 coverslip) gamma-irradiated culture dishes (MatTek Corp. Ashland, MA) by heating to 85 ºC for 10 min on a hotplate.

Microfluidic device priming

Similar to previously published[41], to prime the device 20 μL of L-15 media (Gibco) containing 20% hiFBS was pipetted through one of the two loading ports. 10 μL of the same solution was pipetted on top of each loading port. The device was then placed in a vacuum desiccator connected to house vacuum (27 inHg) for 10 min. Upon removal the device was rested for an additional 10 min, until the attractant filled entirely the straight migration channels, connected orthogonally to the central loading channel. The device was then washed twice, by pipetting into a loading port 200 μL of L-15 media. These washing steps removed the attractant from the central loading channel and its passive diffusion from the migration channels into the central loading channel established a serum gradient. To prevent evaporation, 3 mL of L-15 media were added to the glass-bottomed dish to cover the device.

Retinal preparation

Preparation of retinal stock solutions was performed in a dark room with red-light sources as previously described[14]. In brief, 9-cis-Retinal (Sigma Aldrich R5754) was dissolved in 200 proof ethanol purged (Sigma Aldrich) with argon gas resulting in a concentration of 10 mg/mL. Aliquots were stored at -80 °C in amber glass tubes (Sigma Aldrich).

0.1 g of Bovine Serum Albumin (BSA), Fraction V—Low-Endotoxin Grade (Gemini Bio 700-102P) was vigorously mixed in 10 mL of L-15 media (Gibco), to prepare a 1% BSA solution. In darkness, 10uL of retinal stock was diluted to a working concentration of 10 μg/mL by gradually adding the 1% BSA solution (9 x 10 μL, 9 x 100 μL, 2 x 500 μL, 8 x 1 mL) until all 10 mL were used. The final retinal solution was kept in darkness, on a rocker located in a standard cold room, and was left to incubate overnight. Final retinal solutions were used for experiments within 2 days after preparation.

Retinal incubation and cell loading

3×10^5 differentiated HL60 cells were spun down at 200 g for 5 min and re-suspended in 1 mL of retinal solution to incubate at 37 ºC for 1 h. This incubation and all remaining cell handling happened in darkness with red-light sources. Incubated cells were spun down at 200 g for 10 min and were resuspended in ~20 μL of L-15. Out of this cell suspension, 10 μL were pipetted into the loading port of the device. The device was then transferred on the microscope at 37 ºC, where the cells would be imaged. As a control, we performed some experiments without incubating cells with retinal and found that cells were not responsive to stimulation (data not shown).

Pharmacological perturbations

To explore the role of myosin II/RhoA and ERM proteins/cortical actin in creating a cell back refractory to receptor inputs we pre-treated cells with either 20 μM Y-27632 (Sigma), or 50 μM nocodazole (Sigma) or 50 μM NSC668394 (Sigma) for the last 30 min of retinal incubation. Cells were spun down at 200 g for 5 min and were re-suspended in ~20 μL of L-15 containing the same final drug concentration. Of this cell suspension, 10 μL were loaded in a device that was pre-treated with the same drug concentration. The pharmacological compound was included in both the attractant solution as well as the L-15 solution used for washing, in the same final concentration. For all pharmacological perturbations DMSO was used as a vehicle and 0.15% DMSO As a control, we performed experiments with 0.25% DMSO to match the maximum final DMSO concentration in the drug treatments as controls. We found no significant differences between untreated and DMSO-treated cells (data not shown).

Fluorescence microscopy

Fluorescence microscopy was performed on a Ti-E inverted Nikon microscope with a XLED1 LED light source for epi-fluorescence illumination. Images were acquired every 3 s on two Andor Zyla 4.2

sCMOS cameras, using a Cairn TwinCam LS image splitter equipped with a dichroic mirror (Chroma ZT594rdc, ~ 605 nm edge wavelength) and emission filters to allow simultaneous imaging. The Cdc42 TomKat FRET imaging was performed as previously described[14]. For myosin imaging experiments, we used a 405/488/561/640 nm quad band filter cube (Chroma 91032) that allowed rapid, sequential 407 nm optogenetic stimulation, and simultaneous imaging of mScarlet-I-Myl9 (~ 561 nm excitation), and cytoplasmic iRFP (~ 640 nm excitation). Bandpass emission filters were used to eliminate bleedthrough of iRFP into the myosin channel, but some bleedthrough of mScarlet signal into the iRFP channel was unavoidable and tolerated to allow simultaneous imaging. Rapid and precise stage movements were achieved using an ASI stage (MS-2000 Flat-top) equipped with linear encoders. The microscope was controlled through custom-built MATLAB R2015a software (MathWorks) interfaced with Micro-Manager (Version 1.4.23) to automate cell stimulation and time-lapse microscopy protocols, enabling highly reproducible experimental conditions. Cells were imaged with a 60x oil immersion objective (Nikon Apochromat 1.49 NA) and were maintained at 37 ºC using a temperature and humidity control unit (OkoLab Microscope Lexan Enclosure). Each experiment was terminated within 2 hours of imaging.

Stimulation assays

Cell stimulation and imaging was performed using a custom made MATLAB R2015a interface for Micro-Manager (Version 1.4.23). Subcellular opsin stimulation was performed using a 407 nm laser (Coherent Cube) with a custom fiber coupling inserted in a FRAP port on the microscope. Both the TomKat dichroic and the dichroic used for myosin imaging can pass 407 nm light, enabling rapid FRAP stimulation without the need to swap cubes. To focus the FRAP module, HL60 cells expressing either the TomKat FRET sensor or the mScarlet-I-Myl9 were loaded in a microfluidic device as previously described. Cells were imaged, as described, to determine the appropriate focal plane. We selected cells, zapped them by setting the laser to 40 ms exposure and 10 % power and imaged them using the FRAP channel. The x-y translation knobs of the FRAP module were adjusted to bring the FRAP spot near the center of the image (around 512 pixel x 512 pixel on a 1024 pixel x 1024 pixel image, where 1 pixel is 0.21 μm). Thereafter,

we used the z-adjustment knob to focus the FRAP spot into a tight approximately gaussian-shaped spot. We measured the power of the FRAP laser at the objective using a Thorlabs handheld optical power meter (PM100D) and a microscope slide power sensor (S170C). Cell-stimulation experiments were conducted using ~1.8 µW power measured at the objective. On each experimental day, pictures of the FRAP spot were collected and averaged to identify the pixel with the maximum FRAP spot intensity. The x-y coordinates of the maximum intensity pixel were saved and later used to dynamically translate the stage, so the maximum activation spot coincided with the desired sub-cellular stimulation location.

Each lane on the microfluidic chip was organized into a grid of x-y coordinates that were imaged consequently. Cells were segmented in real time using a minimum fluorescence threshold and minimum and maximum size thresholds. The target point was computed by determining the cell centroid (in the center stimulation assay) or the cell rear (in all other cases). Determination of the cell rear relied on extracting the cell body boundary from the binary mask and determining the point in the cell perimeter as specified by a target angle (for us 180^{o} in respect to the original orientation of cell movement). For persistent stimulation experiments, UV stimulation and imaging were alternated until the imaging period was over. For the 12-pulse stimulation assays we administered a total of 12 pulses of light, whereas for center stimulation assays we administered a total of 5 pulses. For all assays we maintained the same time interval (3 s) for imaging and stimulation. In all assays cells were allowed to migrate unstimulated for 21 frames and right after imaging the 21st frame, we commenced the sub-cellular stimulation, alternating between imaging and stimulation. This results in turning the receptor off with each image and then rapidly back on again with the following stimulation pulse, as parapinopsina is a $G_{\alpha i}$-family coupled GPCR that is activated by UV light and inactivated by orange light (> 530 nm)[14] leading to rapid activation and deactivation cycles. Thus, our stimulation assays are pulsed.

Camera and illumination corrections

Raw images were corrected for the camera dark-state noise, for differences in the camera chip sensitivity, and for dust in the light path as previously described[14]. Moreover, a gradient in apparent FRET ratio activity was empirically observed from the top to bottom of the TomKat FRET sensor images due to imperfections in the light path. To correct for this gradient, we developed a ratio correction image. Images of unstimulated Cdc42 TomKat FRET sensor HL60 cells loaded in microfluidic channels were collected systematically with different stage positions and the same 60x objective so that at least one cell was imaged on every portion of the camera sensor. We computed FRET ratios using our standard analysis pipeline for each image, and assembled the images into a 3D image stack. We took the median of the FRET ratio over the stack (including only pixels corresponding to cells) to generate a single representative full-field FRET image. To reduce local variability, we then smoothed this image by taking the median over each 24 pixel x 24 pixel block and smoothing using a gaussian filter (sigma=5). We then smoothly resized the result to generate a "ratio correction image" with the same dimensions as the input image. We applied the correction by dividing the FRET ratio images by the ratio correction image. We note that this last correction was not necessary for the Myl9 imaging.

Cell segmentation and image background subtraction

Raw FRET pair images were registered using the coordinate-mapping strategy described[14]. Cell segmentation was performed on the sum of the aligned FRET donor and acceptor images, to improve signal to noise ratio. First, we conservatively defined background and cell object pixels. A background image was then determined using the median intensity of background pixels in the local neighborhood of each pixel. The background image was subtracted from the sum image. Object edges were enhanced by first smoothing the image using a broader gaussian filter (sigma=5), and then subtracting the smoothed image from the original image. Finally, the cell object binary masks were determined through the Otsu's threshold method. For each FRET donor and acceptor image we subtracted the background as defined through the above

segmentation strategy. Pixels not included in the cell mask were defined as not a number (NAN), so as to eliminate them from downstream analysis. The FRET ratio image was calculated as FRET acceptor divided by FRET donor. We used a similar strategy to register the mScarlet-I-Myl9 and cytoplasmic iRFP pair images for the myosin cell line and to subtract the background.

Movie processing

For the supplemental movies (Movie S1-Movie S3), each donor and acceptor image was smoothed using a gaussian filter (sigma=2), after subtracting the background as previously described. We note that this smoothing step was only applied to movies and not for any other analysis. The FRET ratio image was calculated, once again, as FRET acceptor divided by FRET donor (using the smoothed images). The same smoothing strategy was applied for the mScarlet-I-Myl9 signal (Movie S4). The Cdc42 activity ratio for each cell was a bit different and since the relative activity across each cell is most informative, we choose to show cells in Movies S1-S3 with a FRET range from the 1^{st} percentile to the 99^{th} percentile of the corrected FRET ratio images on a movie-by-movie basis. For Movie S4, since differences in myosin expression levels had functional consequences, we displayed myosin-expressing cells with fixed bounds from 100 to 2000.

Data analysis

Analysis of the center stimulation assay and threshold assignment for responding cells

We quantified the mean Cdc42 activity over the entire cell body for 60 cells and found a clear increase in Cdc42 activity for most of the cells that started immediately after the initiation of stimulation, peaking at 15 s, right after the last stimulation pulse (Supplemental Fig. 1c). Cdc42 activity returned back to the baseline 15 s later (30 s after the first light pulse). We went on to quantify the relative increase of

Cdc42 activity (Supplemental Fig. 1c) by breaking the cellular response into 4 windows ("Control 1"=[-60:-42] s, "Control 2"=[-39:-21] s, "Control 3"=[-18:0] s and a "Peak" window centered at the maximum Cdc42 activity found between 3 and 33 s with a spread ± 9 s around that, to match the window size with the one of the three other windows). For each cell, we quantified the mean value in each of the 4 windows and then computed a "control" response (by dividing the respective means of "Control 2" by "Control 1"), and a "peak response" (by dividing the respective means of "Peak" by "Control 3"). The control distribution is symmetric around the median 0.9993. Leveraging that, we expected half of the inherently non-responding cells in the peak response distribution to have a relative increase less than 0.9993. Using this statistical argument, we estimated that 93% of cells were responsive (close to the 97% of cells that expressed the opsin). Applying a more stringent threshold at 1.008 (which was exceeded in the control ratio by only 5% of cells) provided a lower bound estimate of 70% responding cells. In both estimated thresholds, the percentage of inherently responding cells was significantly higher than the 47% of cells that reversed upon repetitive stimulation, suggesting that the suppressed percentage of reversing cells was due to some other kind of variation among the cells.

Analysis of the Cdc42 activity profile

To quantify the pre-stimulus Cdc42 activity profiles (Fig. 1d) we stratified cells as reversers and non-reversers, based on their migratory speed. We assumed and verified that cells are in a steady state for the 15 s prior to stimulation, so we averaged over that time window to minimize noise in our measurements. Specifically, for each cell we considered the 6 frames prior to stimulation onset, corresponding to 15 s. For each time point we computed a 1-D profile of the Cdc42 activity, centered at the cell centroid and interpolated the Cdc42 activity profile over a fixed number of points (the average cell length) to account for variabilities in cell length. Interpolation was carried out via fitting a cubic smooth spline with the smoothing parameter set at the default value of 0.5 (where 0 fits a straight line and 1 gives a total fit). We

computed a mean profile over each cell averaging these 6 interpolated profiles. As a final step, we averaged across all cells in each of the two groups and computed mean profiles (solid lines), standard deviations (shaded regions) and standard error of the means (error bars).

Subcellular localization of Cdc42 activity and myosin II

Cell front and rear areas were defined as the 800 points closest to the cell front and rear edge. The 800 points enabled us to capture the entire penetration depth of the Cdc42 activity at the cell front. We note that the order of events (Fig. 2) was qualitatively the same for different penetration depths (800 points, 400 points and 200 points): the stimulated rear responded first, then the front, followed by the cell reversing its direction of migration, before the Cdc42 cross-over point. To define the cell middle, we computed the major axis of the segmented cell body, divided it into three equidistant length segments, and took a rectangular window around the middle part of the cell. For each area of interest (front, rear and middle) we computed the Cdc42 activity as the sum of the donor signal divided by the sum of the acceptor signal in that area. We used the same strategy to identify the front, rear, and middle of Myl9-expressing cells, so that we can directly compare the dynamic re-localization of Cdc42 activity and myosin II (Figs. 6c-6e). To analyze the relative subcellular distribution of myosin, we computed the normalized myosin at the front, rear and middle as the sum of the Myl9 signal in each area of interest divided by the sum of the Myl9 signal in the entire segmented cell body (Figs. 6d-6e, 7e-7f, Supplemental Figs. 5e-5g and Supplemental Fig. 6c).

Cell speed, length and area analysis

Cell centroid speed was computed by dividing the displacement of the cell's centroid between two consecutive frames with the frame time interval (3 s). For each cell its speed trace was then smoothed with a local regression using weighted linear least squares and a 2^{nd} degree polynomial model ("loess" or locally weighted smoothing in MATLAB). We used a span of 10% of the total number of data points for this

smoothing. We then computed the mean cell speed averaging these smoothed speed traces (Figs. 2c, 2g, 4a and 6c and Supplemental Fig. 4a).

Cell length was approximated via computing the major axis of the binary cell mask, while cell area was calculated by summing the total number of pixels of the computed binary cell mask. Relative changes in length and area were plotted by dividing the cell length and area for each cell by its respective length and area before stimulation (Fig. 2d).

Determination of the order of events

Temporal determination of the order of events relied on interpolating the time between the closest time-points to key events, namely rear response, front response, cell stalling and Cdc42 activity cross-point. Stimulated rear response was defined as a 1% increase in the Cdc42 activity at the rear, whereas front response was defined as a 1% decrease in Cdc42 activity at the front from the steady-state baseline values for rear and front at t=0 s. Cell stalling was defined as the interpolated time-point where the cell's centroid speed was zero, and Cdc42 cross-point as the interpolated time-point where the Cdc42 activities of front and rear intersected. This temporal analysis was performed both on average trends (Figs. 2a-2c) as well as on a single-cell level (Figs. 2e-2f).

Stratification into cellular responses

Cells were stratified into reversers and non-reversers based on whether they responded to the persistent optogenetic stimulation by reversing their direction of migration and Cdc42 activity axis (Figs. 1c-1g). Transient stimulation resulted in additional cellular responses, namely no response, medium response, strong response, and stably reversing cells (Figs. 3-5). We classified "no response" cells as cells that showed no or minimal rise (<2%) in Cdc42 activity at their rear, when compared to the pre-stimulation

rear activity (averaging over 15 s prior to the initiation of stimulation). Medium responding cells were cells that showed some increase of Cdc42 activity at their rear (>2%) but no engagement of the front (difference between minimum front Cdc42 activity and maximum back Cdc42 activity > 0.03), often resulting in cell body elongation. Strong responding cells were classified as cells that showed engagement of both the rear and the front, but not stably reversing (many of these cells transiently reversed direction but flipped back to their original direction after the stimulus ended). Reversed cells were defined as previously described. To extend this analysis to the myosin cell line, the method had to be adjusted, given the lack of a Cdc42 signal reporter in that line (Figs. 6-7). Similar to before, strong responding and reversed Myl9-expressing cells were classified based on reversing their myosin polarity and direction of migration transiently or stably, respectively (for Y27632-treated cells only migratory speed was considered). Non-responding and medium responding Myl9-expressing cells were classified using a combination of migratory speed, morphology and manual curation.

Kymograph representation for Cdc42 activity and myosin

For each cell and each time point, a 1-D profile of either Cdc42 activity or myosin was computed from cell front to rear. These 1-D profiles were aligned according to the cell centroid. To account for the fact that the cell length was variable across cells and time points we took these 1-D profiles and aligned them to a fixed average cell length, through interpolation. For each time point we took the interpolated 1-D profiles and computed an average profile from all cells. Interpolation was carried out as described above, via fitting a cubic smooth spline with the smoothing parameter set at the default value of 0.5. Synthesizing the average profiles along time, we constructed kymograph representations (Fig. 4d, Figs. 5e-5g, Figs. 7e-7f, Supplemental Fig. 4d and Supplemental Fig. 5c).

Statistical analysis

For categorical data, day-to-day and experiment-to-experiment variation was consistent with counting noise and the observed standard deviations were reasonably explained by the binomial model in each case. For quantitative signaling, speed, and localization data, cell-to-cell variability was the dominant source of variability. Given the limited and variable number of cells that could be analyzed in each experiment, we felt that individual cells represented the most relevant independent unit for statistical analysis. We were also careful to perform control experiments on each day to avoid potential bias. Based on these considerations, we pooled data from all independent experiments performed. We indicate the number of cells and the number of independent experiments in the Figure Legends. All measurements were taken using independent cell. Statistical parameters and significance are reported in the Figures and the Figure Legends. Data are determined to be statistically significant when $p < 0.05$ by either Wilcoxon rank sum test or Fisher exact test ("ranksum" or "fishertest" in MATLAB, respectively). All statistical tests were two-sided.

To depict the percentage of reversing cells (Fig. 1c and Supplemental Fig. 2d) under persistent stimulation we represented data with bar plots showing the cumulative mean value and an error bar which represents the confidence interval assuming a binomial distribution around the cumulative mean, pulling data from all independent experiments.

For the statistical analysis of the subcellular localization of Cdc42 activity and myosin II as well as the centroid speed, we used violin plots pooling all cells that passed our pre-processing standards of masking and tracking, from all independent experiments (Figs. 1e-1f, 3c, 7b-7d and Supplemental Figs. 1a-1c, 3a-3d and 3f-3j, 4d-4g, 5a-5c). In each violin plot the dashed line represents the median of the distribution and the dotted lines the 25% and 75% quartiles of the distribution. To compare among groups (*e.g.* reversing and non-reversing cells or among cellular responses or drug perturbations), we performed non-parametric two-sided Wilcoxon rank sum tests.

To depict the percentage of cells in each response class under titrated stimulation, we used stacked bar plots (Figs. 3b, 5c, 6a, 7a and Supplemental Fig. 3e). We performed the Fisher exact test on the distributions as a whole to examine whether at least one of the classes differed between compared pairs (p-values are reported on the Figs.). In addition, we computed the Fisher exact for each cellular response class between conditions (*e.g.* comparing the reversers in untreated cells vs Y27632-treated cells etc.) to probe which classes significantly changed. Based on those two considerations, we highlighted the significant difference in the main text.

Plotting

Plotting was performed using MATLAB R2018a (MATHWORKS) and GraphPad Prism 8.

4.9 Acknowledgments

We thank Emel Akdogan for help with the flow cytometry measurements. We thank Tony Y.-C. Tsai and Effie Bastounis for insightful discussions and comments on the manuscript. We thank Bridgette McLaughlin at the UC Davis Cancer Center Flow Cytometry core (supported by P30 CA093373) for technical assistance with cell sorting. This work was supported by the Howard Hughes Medical Institute (J.A.T.), and an NIH Director's New Innovator Award (DP2 HD094656) to S.R.C. A.H. was a Stanford Bio-X Bowes Fellow, an Onassis Foundation Scholar, and was supported by the Foundation for Education and European Culture (IPEP), the A.G. Leventis Foundation and the Attica Tradition Foundation. Microfabrication work was supported by NIG grant GM092804 to D.I. G.R.R.B. thanks the National Science Foundation Graduate Research Fellowship (Grant Number 1650042) for support.

4.10 Data availability statement

The data that support the findings of this study are available from the corresponding authors upon request.

4.11 Code availability statement

The code we developed for automating experiments and data analysis is available from the corresponding authors upon request.

4.12 Competing interests statement

The authors declare no competing financial interests.

4.13 References

1. Iijima, M., Huang, Y. E. & Devreotes, P. Temporal and Spatial Regulation of Chemotaxis. *Dev. Cell* **3**, 469–478 (2002).
2. Servant, G. *et al.* Polarization of Chemoattractant Receptor Signaling During Neutrophil Chemotaxis. *Science* **287**, 1037–1040 (2000).
3. Xu, J. *et al.* Divergent Signals and Cytoskeletal Assemblies Regulate Self-Organizing Polarity in Neutrophils. *Cell* **114**, 201–214 (2003).
4. Yang, H. W., Collins, S. R. & Meyer, T. Locally excitable Cdc42 signals steer cells during chemotaxis. *Nat. Cell Biol.* **18**, 191–201 (2016).
5. Hind, L. E., Vincent, W. J. B. & Huttenlocher, A. Leading from the back: the role of the uropod in neutrophil polarization and migration. *Dev. Cell* **38**, 161–169 (2016).
6. Wang, F. *et al.* Lipid products of PI(3)Ks maintain persistent cell polarity and directed motility in neutrophils. *Nat. Cell Biol.* **4**, 513–518 (2002).
7. Weiner, O. D. *et al.* A PtdInsP(3)- and Rho GTPase-mediated positive feedback loop regulates neutrophil polarity. *Nat. Cell Biol.* **4**, 509–513 (2002).
8. Houk, A. R. *et al.* Membrane Tension Maintains Cell Polarity by Confining Signals to the Leading Edge during Neutrophil Migration. *Cell* **148**, 175–188 (2012).

9. Zigmond, S. H., Levitsky, H. I. & Kreel, B. J. Cell polarity: an examination of its behavioral expression and its consequences for polymorphonuclear leukocyte chemotaxis. *J. Cell Biol.* **89**, 585–592 (1981).

10. Dehghani Zadeh, A., Seveau, S., Halbwachs-Mecarelli, L. & Keller, H. U. Chemotactically-induced redistribution of CD43 as related to polarity and locomotion of human polymorphonuclear leucocytes. *Biol. Cell* **95**, 265–273 (2003).

11. Gerisch, G. & Keller, H. U. Chemotactic reorientation of granulocytes stimulated with micropipettes containing fMet-Leu-Phe. *J. Cell Sci.* **52**, 1–10 (1981).

12. Prentice-Mott, H. V. *et al.* Directional memory arises from long-lived cytoskeletal asymmetries in polarized chemotactic cells. *Proc. Natl. Acad. Sci.* **113**, 1267–1272 (2016).

13. Skoge, M. *et al.* Cellular memory in eukaryotic chemotaxis. *Proc. Natl. Acad. Sci.* **111**, 14448–14453 (2014).

14. Bell, G. R. R., Rincón, E., Akdoğan, E. & Collins, S. R. Optogenetic control of receptors reveals distinct roles for actin- and Cdc42-dependent negative signals in chemotactic signal processing. *bioRxiv* 2021.04.03.438340 (2021) doi:10.1101/2021.04.03.438340.

15. Smith, L. A., Aranda-Espinoza, H., Haun, J. B., Dembo, M. & Hammer, D. A. Neutrophil Traction Stresses are Concentrated in the Uropod during Migration. *Biophys. J.* **92**, L58–L60 (2007).

16. Uchida, K. S. K., Kitanishi-Yumura, T. & Yumura, S. Myosin II contributes to the posterior contraction and the anterior extension during the retraction phase in migrating Dictyostelium cells. *J. Cell Sci.* **116**, 51–60 (2003).

17. Craig, R., Smith, R. & Kendrick-Jones, J. Light-chain phosphorylation controls the conformation of vertebrate non-muscle and smooth muscle myosin molecules. *Nature* **302**, 436–439 (1983).

18. Smith, R. C. *et al.* Regulation of myosin filament assembly by light-chain phosphorylation. *Philos. Trans. R. Soc. Lond. B. Biol. Sci.* **302**, 73–82 (1983).

19. Heissler, S. M. & Sellers, J. R. Myosin light chains: Teaching old dogs new tricks. *BioArchitecture* **4**, 169–188 (2014).

20. Zhang, H. *et al.* Phosphorylation of the myosin regulatory light chain plays a role in motility and polarity during Dictyostelium chemotaxis. *J. Cell Sci.* **115**, 1733–1747 (2002).

21. Kimura, K. *et al.* Regulation of Myosin Phosphatase by Rho and Rho-Associated Kinase (Rho-Kinase). *Science* **273**, 245–248 (1996).

22. Niggli, V. Rho-kinase in human neutrophils: a role in signalling for myosin light chain phosphorylation and cell migration. *FEBS Lett.* **445**, 69–72 (1999).

23. Tsai, T. Y.-C. *et al.* Efficient Front-Rear Coupling in Neutrophil Chemotaxis by Dynamic Myosin II Localization. *Dev. Cell* **49**, 189-205.e6 (2019).

24. Krendel, M., Zenke, F. T. & Bokoch, G. M. Nucleotide exchange factor GEF-H1 mediates cross-talk between microtubules and the actin cytoskeleton. *Nat. Cell Biol.* **4**, 294–301 (2002).

25. Matsuzawa, T., Kuwae, A., Yoshida, S., Sasakawa, C. & Abe, A. Enteropathogenic Escherichia coli activates the RhoA signaling pathway via the stimulation of GEF-H1. *EMBO J.* **23**, 3570–3582 (2004).

26. Birukova, A. A. *et al.* GEF-H1 is involved in agonist-induced human pulmonary endothelial barrier dysfunction. *Am. J. Physiol.-Lung Cell. Mol. Physiol.* **290**, L540–L548 (2006).

27. Chang, Y.-C., Nalbant, P., Birkenfeld, J., Chang, Z.-F. & Bokoch, G. M. GEF-H1 Couples Nocodazole-induced Microtubule Disassembly to Cell Contractility via RhoA. *Mol. Biol. Cell* **19**, 2147–2153 (2008).

28. Niggli, V. Microtubule-disruption-induced and chemotactic-peptide-induced migration of human neutrophils: implications for differential sets of signalling pathways. *J. Cell Sci.* **116**, 813–822 (2003).

29. Takesono, A., Heasman, S. J., Wojciak-Stothard, B., Garg, R. & Ridley, A. J. Microtubules Regulate Migratory Polarity through Rho/ROCK Signaling in T Cells. *PLOS ONE* **5**, e8774 (2010).

30. Liu, B. P., Chrzanowska-Wodnicka, M. & Burridge, K. Microtubule Depolymerization Induces Stress Fibers, Focal Adhesions, and DNA Synthesis via the GTP-Binding Protein Rho. *Cell Adhes. Commun.* **5**, 249–255 (1998).

31. Ivetic, A. & Ridley, A. J. Ezrin/radixin/moesin proteins and Rho GTPase signalling in leucocytes. *Immunology* **112**, 165–176 (2004).

32. Yoshinaga-Ohara, N., Takahashi, A., Uchiyama, T. & Sasada, M. Spatiotemporal regulation of moesin phosphorylation and rear release by Rho and serine/threonine phosphatase during neutrophil migration. *Exp. Cell Res.* **278**, 112–122 (2002).

33. Fehon, R. G., McClatchey, A. I. & Bretscher, A. Organizing the cell cortex: the role of ERM proteins. *Nat. Rev. Mol. Cell Biol.* **11**, 276–287 (2010).

34. Liu, X. *et al.* Moesin and myosin phosphatase confine neutrophil orientation in a chemotactic gradient. *J. Exp. Med.* **212**, 267–280 (2015).

35. Irimia, D. *et al.* Microfluidic system for measuring neutrophil migratory responses to fast switches of chemical gradients. *Lab. Chip* **6**, 191–198 (2006).

36. Petrie Aronin, C. E. *et al.* Migrating Myeloid Cells Sense Temporal Dynamics of Chemoattractant Concentrations. *Immunity* **47**, 862-874.e3 (2017).

37. Moujaber, O. & Stochaj, U. The Cytoskeleton as Regulator of Cell Signaling Pathways. *Trends Biochem. Sci.* **45**, 96–107 (2020).

38. Yusa, K., Rad, R., Takeda, J. & Bradley, A. Generation of transgene-free induced pluripotent mouse stem cells by the piggyBac transposon. *Nat. Methods* **6**, 363–369 (2009).

39. Millius, A. & Weiner, O. D. Chemotaxis in neutrophil-like HL-60 cells. *Methods Mol. Biol. Clifton NJ* **571**, 167–177 (2009).

40. Boneschansker, L., Yan, J., Wong, E., Briscoe, D. M. & Irimia, D. Microfluidic platform for the quantitative analysis of leukocyte migration signatures. *Nat. Commun.* **5**, 4787 (2014).

41. Garner, R. M. *et al.* Neutrophil-like HL-60 cells expressing only GFP-tagged β-actin exhibit nearly normal motility. *Cytoskeleton* **77**, 181–196 (2020).

42. Chau, A. H., Walter, J. M., Gerardin, J., Tang, C. & Lim, W. A. Designing synthetic regulatory networks capable of self-organizing cell polarization. *Cell* **151**, 320–332 (2012).

43. Bourne, H. R. & Weiner, O. Cell polarity: A chemical compass. *Nature* **419**, 21–21 (2002).

44. Khaliullin, R. N. *et al.* A positive-feedback-based mechanism for constriction rate acceleration during cytokinesis in Caenorhabditis elegans. *eLife* **7**, e36073 (2018).

45. Carlsson, A. E. Growth of Branched Actin Networks against Obstacles. *Biophys. J.* **81**, 1907–1923 (2001).

46. Lomakin, A. J. *et al.* Competition of two distinct actin networks for actin defines a bistable switch for cell polarization. *Nat. Cell Biol.* **17**, 1435–1445 (2015).

4.14 Figures

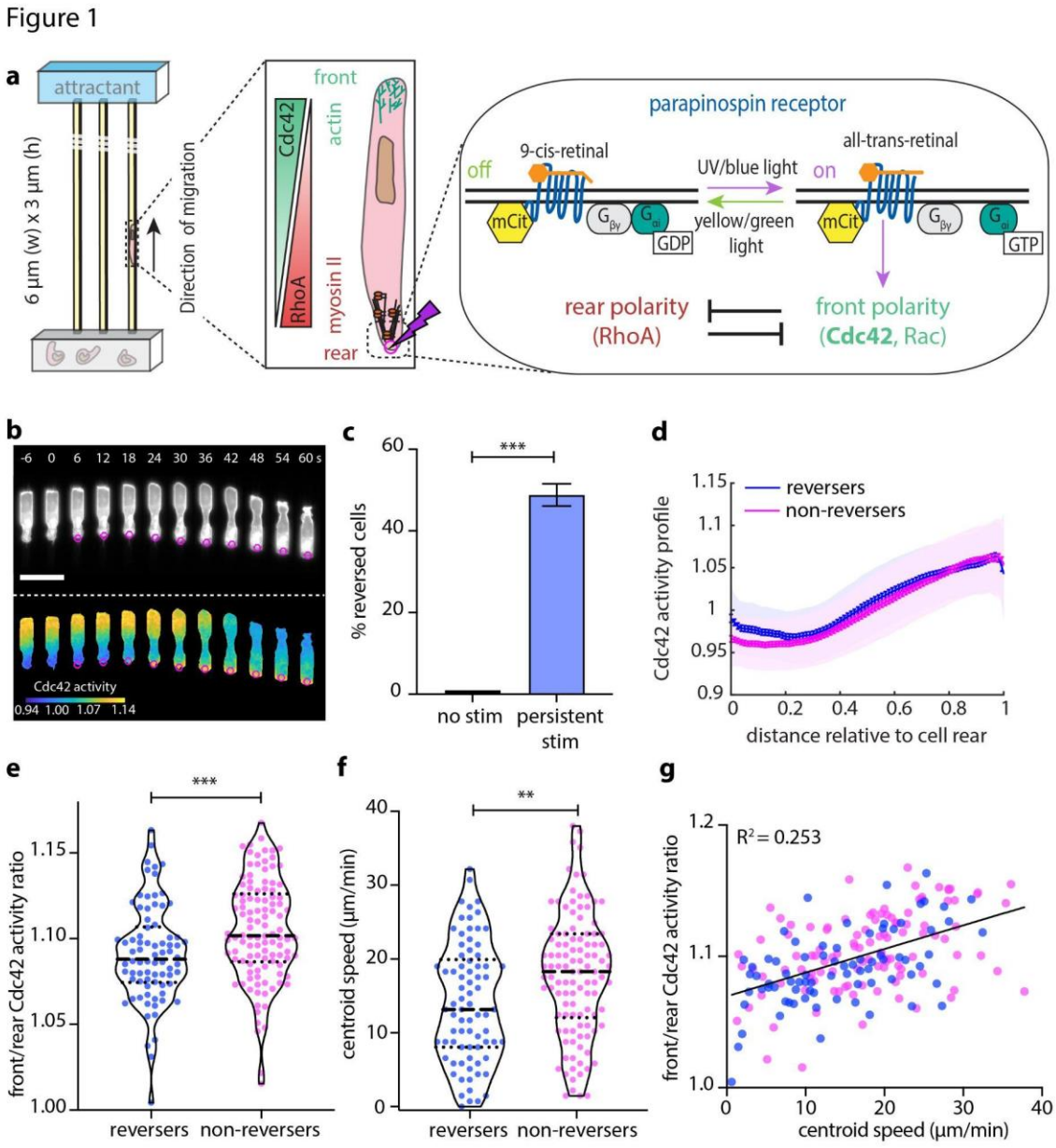

Figure 4.1 Persistent optogenetic stimulation is sufficient to reverse weakly polarized and slowly migrating cells.

(a) Schematic representation of the front-rear polarity reversal assay. HL60 cells expressing parapinopsin, an optogenetic GPCR, migrate inside microfluidic devices that harbor straight channels. A heat inactivated

serum gradient is used as an attractant. The opsin can be turned on using UV/blue light and off with yellow/green light, offering complete control of the receptor activity. Blue light stimulation (magenta circle/lighting bolt) at the rear of the cell turns on the receptor. The receptor is coupled to the polarity signal transduction network and activation re-enforces the front module. **(b)** Live-cell imaging snapshots of cells expressing parapinopsin and a red/far-red Cdc42 FRET sensor. Cells migrate unperturbed for 60 s prior to initiation of persistent pulsed stimulation (magenta circles) at their rear. Upper and lower panels show the registered sensors (grey scale) and the computed Cdc42 activity, respectively. Images captured every 3 s and subsampled for illustration purposes. Scale bar: 25 μm. **(c)** Box plot of the percentage of cells that reversed with persistent pulsated stimulation (n=336 cells from 36 independent experiments) versus non-stimulated control (n=32 cells from 3 independent experiments). Error bar represents confidence intervals assuming a binomial distribution around the cumulative mean. Fisher exact test revealed a significant difference between the two conditions (***: $p<0.001$). **(d)** Mean Cdc42 activity profiles for n=78 reverser (blue) and n=110 non-reverser (magenta) cells averaging cell profiles over 15 s prior to stimulation (lines: means, shaded regions: SD, error bars: SE). **(e-f)** Violin plots of mean front/rear Cdc42 activity ratio **(e)** and of mean centroid speed **(f)** of n=78 reversers and n=110 non-reversers cells, averaging over 15 s prior to stimulation; p-values of two-sided Wilcoxon rank sum test (**: $p<0.01$, ***: $p<0.001$). **(g)** Linear regression between calculated mean front/rear Cdc42 activity, shown in **(e)**, and mean centroid speed, shown in **(f)**, prior to stimulation, for n=188 cells yields $R^2=0.253$ ($p=2x10^{-13}$).

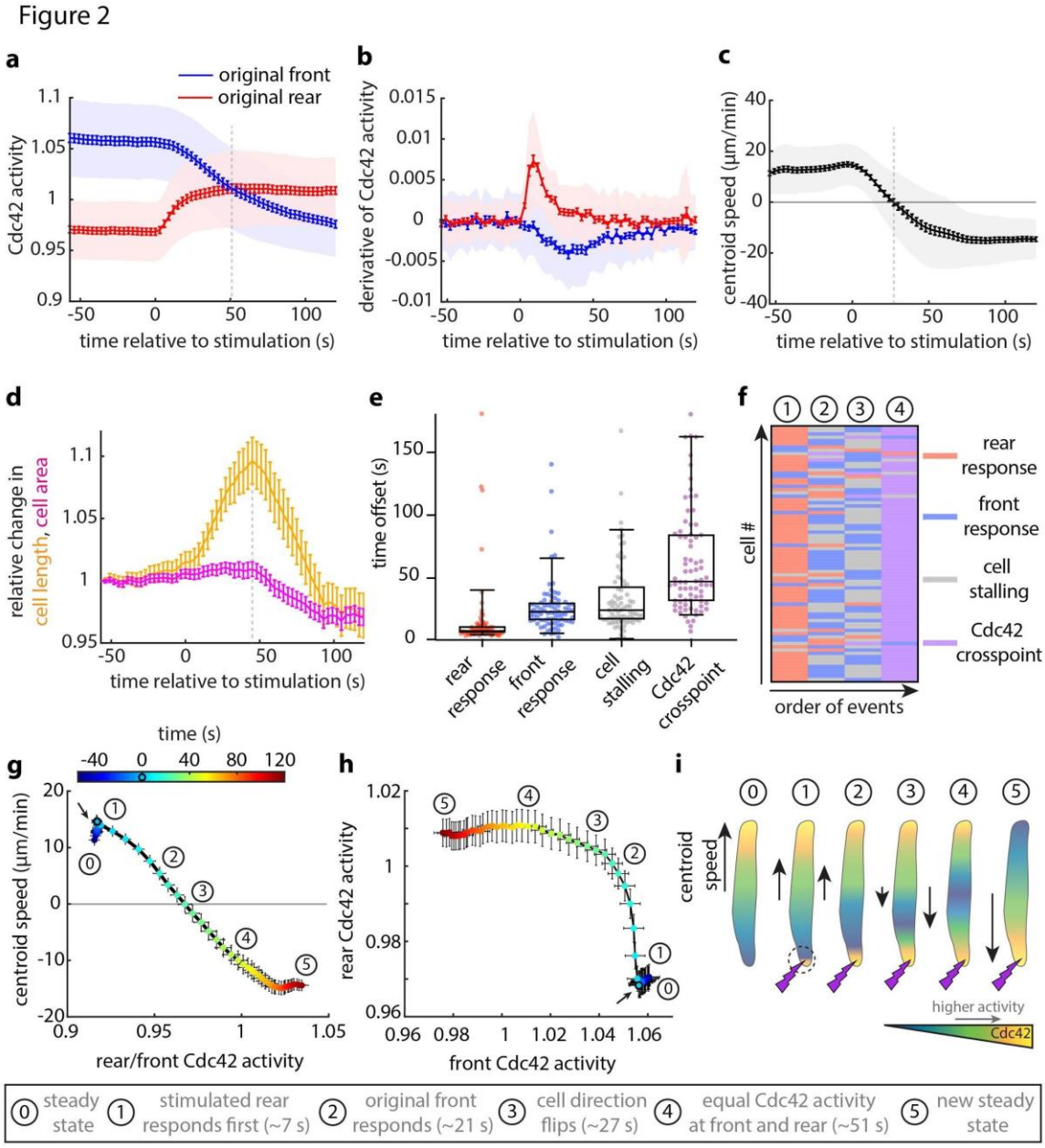

Figure 4.2 In reversing cells Cdc42 activation at the stimulated original rear begins immediately and cells reverse their direction of migration before Cdc42 activity flips polarization.

(a-b) Mean magnitude **(a)** and derivative **(b)** of Cdc42 activity at the original cell front (blue) and rear (red) over time (lines: means, shaded regions: SD, error bars: SE). Data are averages from n=78 reverser cells from 36 independent experiments. Dashed vertical line in **(a)** shows Cdc42 crossover point. **(c)** Centroid

speed of cells that reversed their migratory direction over time (line: mean, shaded region: SD, error bars: SE). Data are averages from the same 78 cells shown before. Dashed vertical line indicates when cell stalling (zero speed) occurs. **(d)** Relative change in cell length (orange) and cell area (magenta) both normalized to the initial length and area for each of 78 cells. Dashed vertical line indicates the time when the relative change in cell length reaches maximum value. Note that the normalized area appeared to decrease post-stimulation, overshooting below the starting value. This relative decrease in cell area was associated with a smaller rear after repolarization. Moreover, the Cdc42 activity at the new emerging front was restricted in a smaller depth as compared with the pre-stimulus steady state (Movie S1), suggesting that the repolarized cell adopted a sharper Cdc42 activity profile with a more constricted rear. **(e)** Box plots of the time-offset for rear response, front response, cell stalling, and Cdc42 cross-point for 78 cells that reversed. **(f)** Heat map of the order of events (columns) across 78 reversed cells (rows). Circled numbers correspond to the cell states shown in **(i)**. **(g-h)** Phase diagrams of mean centroid speed versus mean rear/front Cdc42 activity **(g)** and of mean rear versus mean front Cdc42 activity **(h)**, averaging over 78 reversed cells. Colored points correspond to the average cell state at different time points relative to the start of the persistent pulsated stimulation (black circle/arrow). Circled numbers indicate the cell states as summarized in **(i)** and error bars denote SE. **(i)** Cartoon depiction of the average order of events for a cell that reverses.

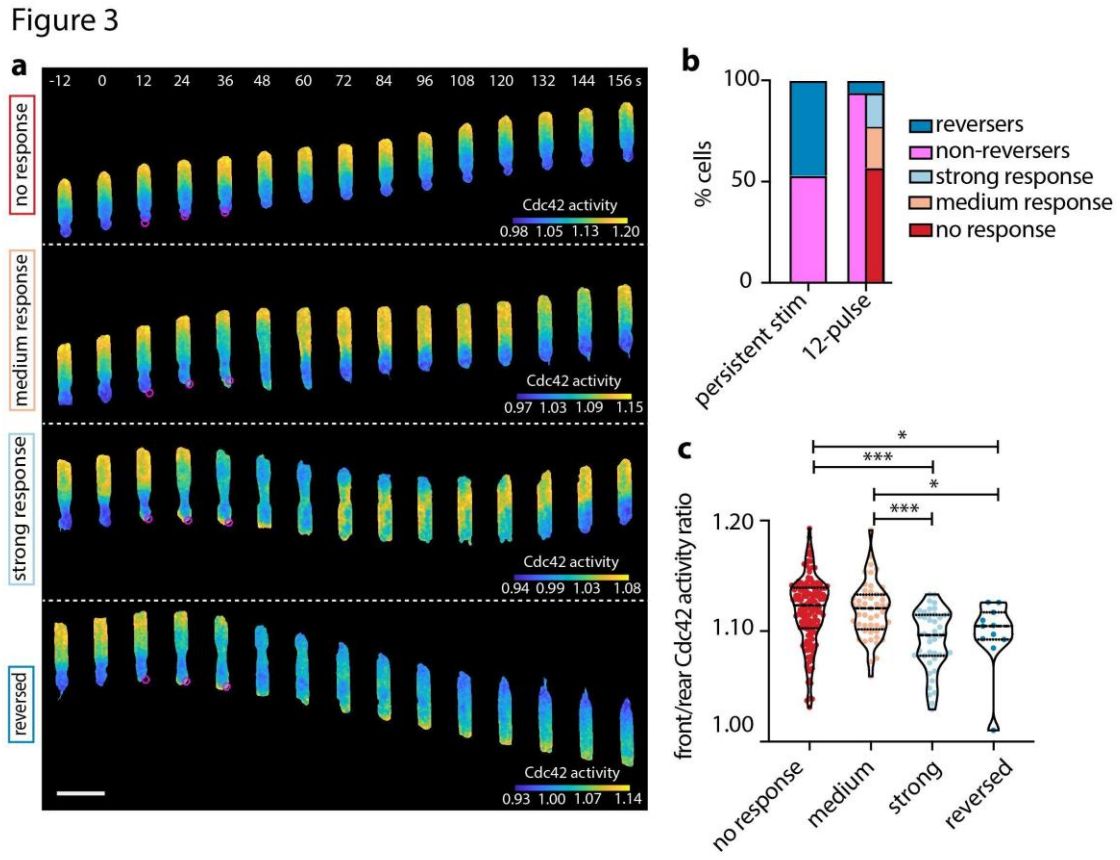

Figure 4.3 Transient stimulation reveals a variety of distinct cellular responses.

(a) Representative live-cell imaging snapshots of stimulation experiments with cells expressing parapinopsin and a red/far-red Cdc42 FRET sensor, showing no response (upper panel), medium response, strong response, and a reversed response (lower panel). Cells migrated unperturbed for 60 s prior to starting a transient 12-pulse stimulation at their cell rear (magenta circles). Images captured every 3 s and subsampled for illustration purposes. Scale bar: 25 μm. **(b)** Stacked bar plot of the percentage of cells that exhibited each cellular response with persistent pulsated stimulation (n=336 cells from 36 independent experiments), and with transient 12-pulse stimulation (n=264 cells from 20 independent experiments). **(c)** Violin plot of mean front/rear Cdc42 activity ratio of n=141 non-responders, n=49 medium responders, n=44 strong responders, and n=11 reversers, averaging over 15 s prior to stimulation; p-values of two-sided Wilcoxon rank sum test (*: $p<0.05$, ***: $p<0.001$, pairs not shown have $p>0.05$).

Figure 4

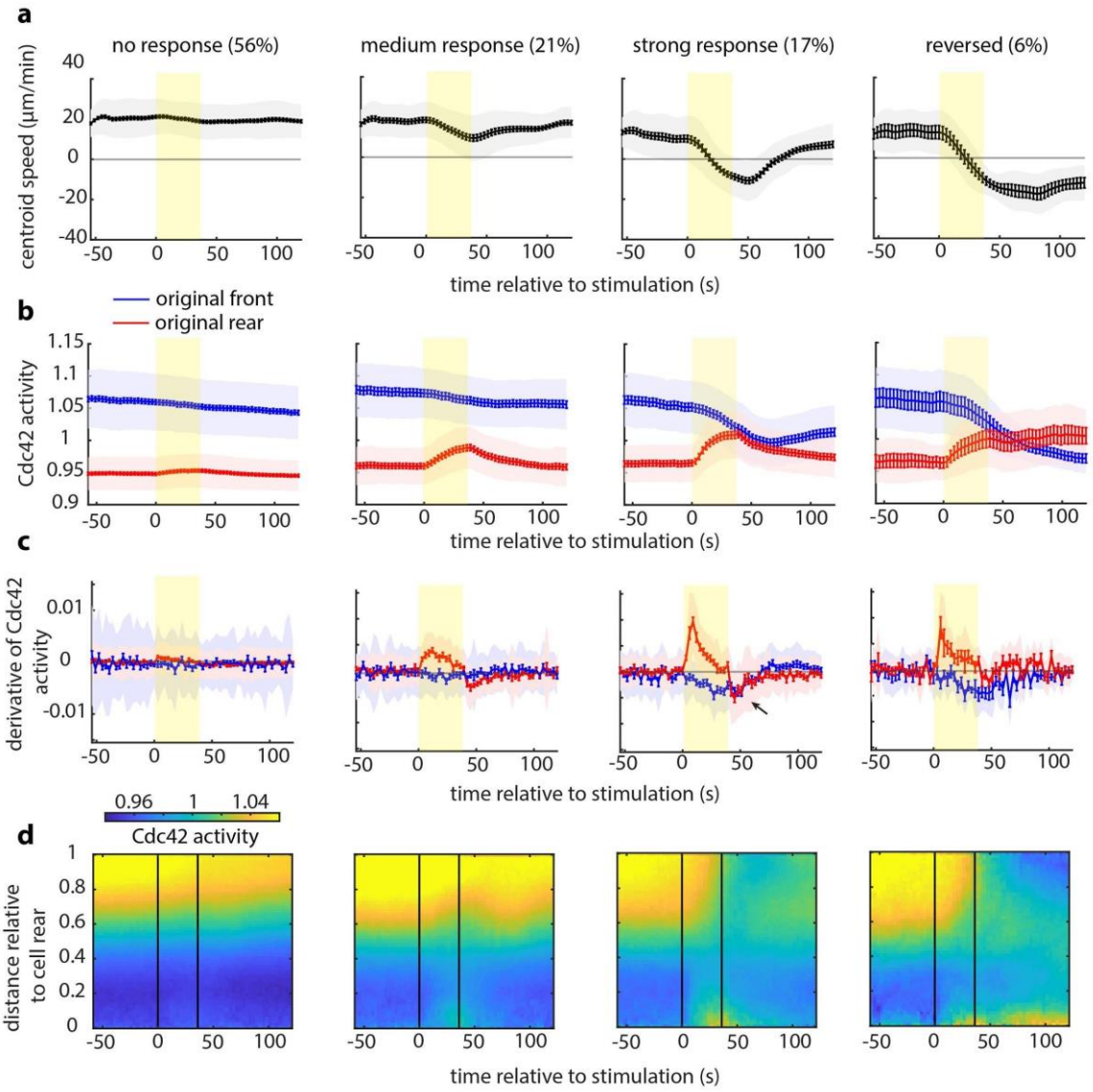

Figure 4.4 A strong cell rear is refractory to receptor inputs.

(a-c) Cell centroid speed **(a)**, mean Cdc42 activity **(b)** and derivative of Cdc42 activity **(c)** at the original front (blue) and rear (red) over time for each cellular response (lines: means, shaded regions: SD, error bars: SE). Data are averages from n=141 non-responders, n=49 medium responders, n=44 strong responders, and n=11 reversers from 20 independent experiments. Rectangular yellow shaded region marks the start and end of the 12-pulse stimulation. **(d)** Average kymograph representation of Cdc42 activity as a function of

time (x-axis) and vertical position relative to the cell rear (y-axis) for non-responding, medium responding, strong responding and reversing cells. Vertical black lines indicate the start and end of the pulsated stimulation.

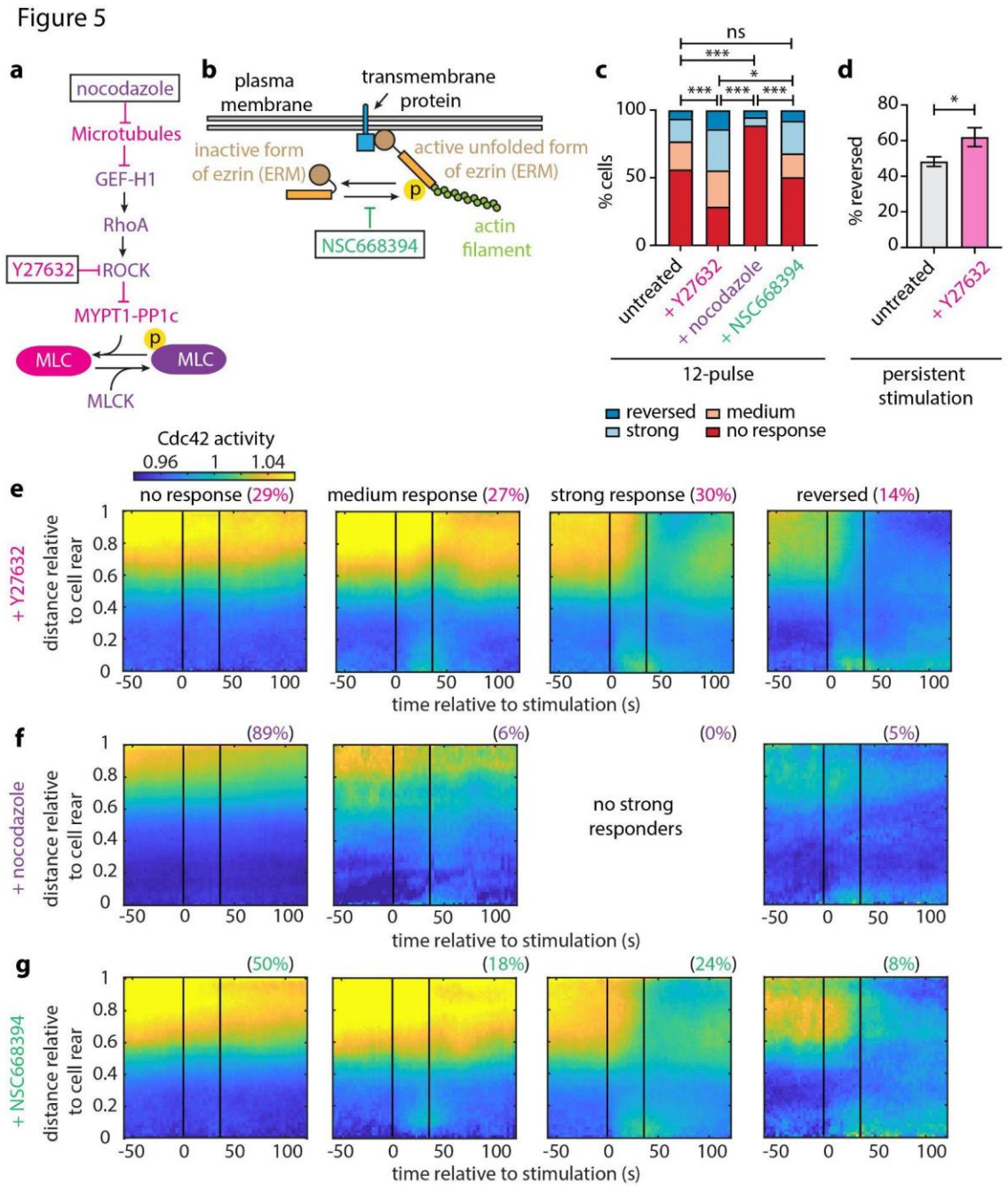

Figure 4.5 The phosphorylation of myosin regulatory light chain tunes the amenability of the rear to respond to receptor inputs.

(a) Diagram of the signaling cascade regulating MRLC phosphorylation (adapted from [23]). A protein or perturbation that increases or decreases MRLC phosphorylation is colored with purple or magenta,

respectively. **(b)** Sketch showing how the ERM proteins establish crosslinks between the plasma membrane and cortical actin. **(c)** Stacked bar plots of percentage of cells exposed to transient stimulation that showed no response, medium response, strong response and reversed for n=264 untreated cells, for n=115 Y27632-treated cells, n=99 nocodazole-treated cells, and n=91 NSC668394-treated cells (from 20, 7, 7 and 6 independent experiments, respectively); p-values of Fisher exact tests (*: $p<0.05$, ***: $p<0.001$, ns: $p>0.05$). (d) Bar plot of the percentage of Cdc42-expressing cells that reversed in response to persistent stimulation for n=336 untreated cells and n=84 Y27632-treated cells (from 36 and 6 independent experiments, respectively). Error bars represent confidence intervals assuming a binomial distribution around the cumulative mean of each group. Fisher exact test revealed a significant difference between the two conditions (*: $p<0.05$). **(e-g)** Average kymograph representation of Cdc42 activity as a function of time (x-axis) and vertical position relative to the cell rear (y-axis) for n=107 Y27632-treated cells **(e)**, n=76 nocodazole-treated cells **(f)**, and n=84 NSC668394-treated cells **(g)**. Vertical black lines indicate the start and end of the pulsated stimulation.

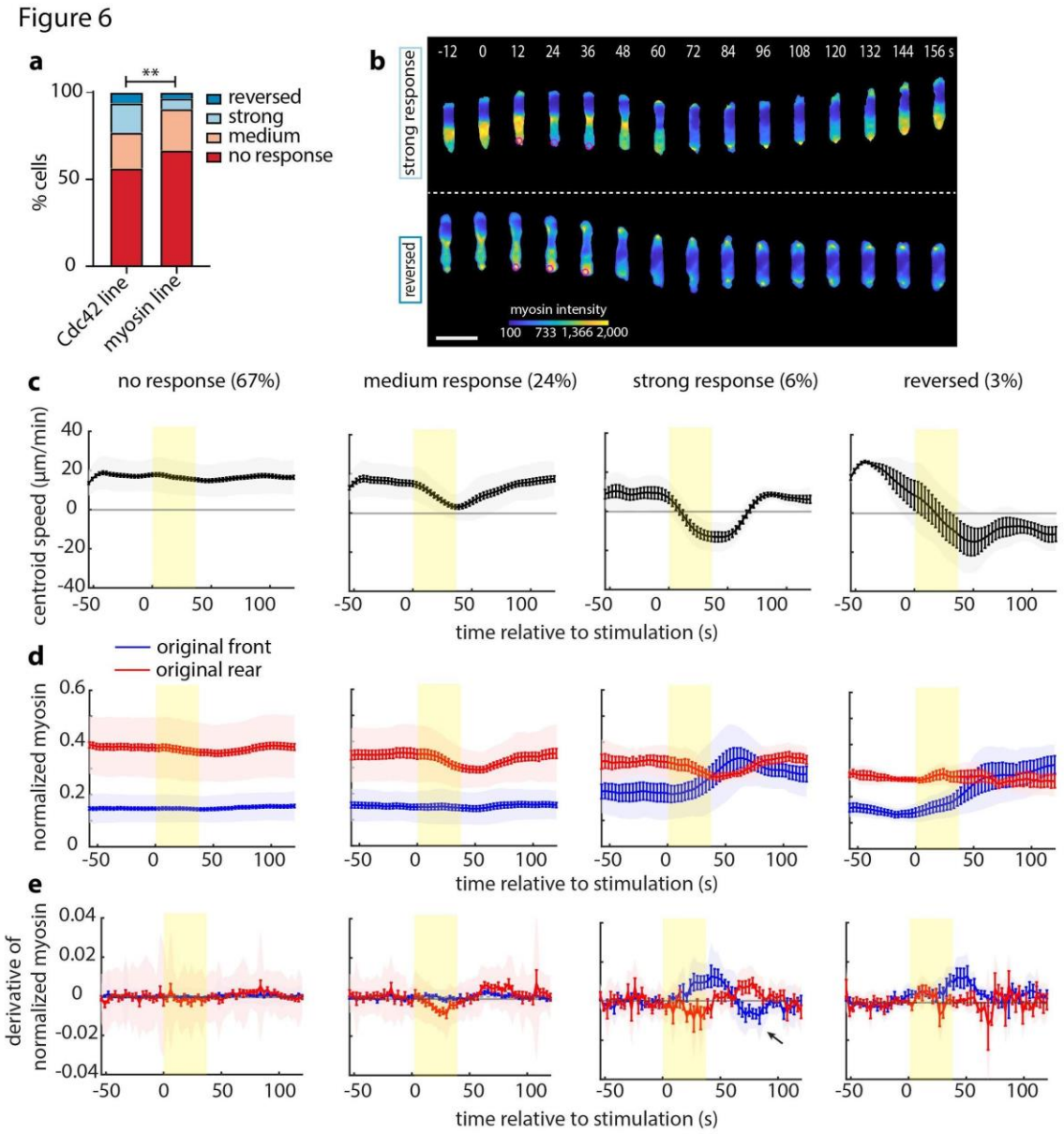

Figure 4.6 Myosin II suppresses cellular reorientation and lags behind Cdc42 activity response.

(a) Stacked bar plots of percentage of cells exposed to transient stimulation that showed no response, medium response, strong response and reversed for n=264 cells of the Cdc42 line and n=147 cells of the myosin line (from 20 and 8 independent experiments, respectively); p-value of Fisher exact test (**: $p<0.01$). **(b)** Representative live-cell imaging snapshots of stimulation experiments with cells expressing parapinopsin and a myosin light chain sensor/cytosolic tag, showing a strong response (upper panel), and a

reversed response (lower panel). Cells migrated unperturbed for 60 s prior to starting a transient 12-pulse stimulation at their cell rear (magenta circles). Myosin intensity pseudo colored to facilitate visualization. Images captured every 3 s, and subsampled for illustration purposes. Scale bar: 25 μm. **(c-e)** Mean cell centroid speed **(c)**, normalized magnitude **(d)** and normalized derivative **(e)** of myosin intensity at the original front (blue) and rear (red) over time for each cellular response (lines: means, shaded regions: SD, error bars: SE). Data are averages from n=98 non-responders, n=35 medium responders, n=9 strong responders, and n=5 reversers. Rectangular yellow shaded region represents the start and stop of the pulsated stimulation.

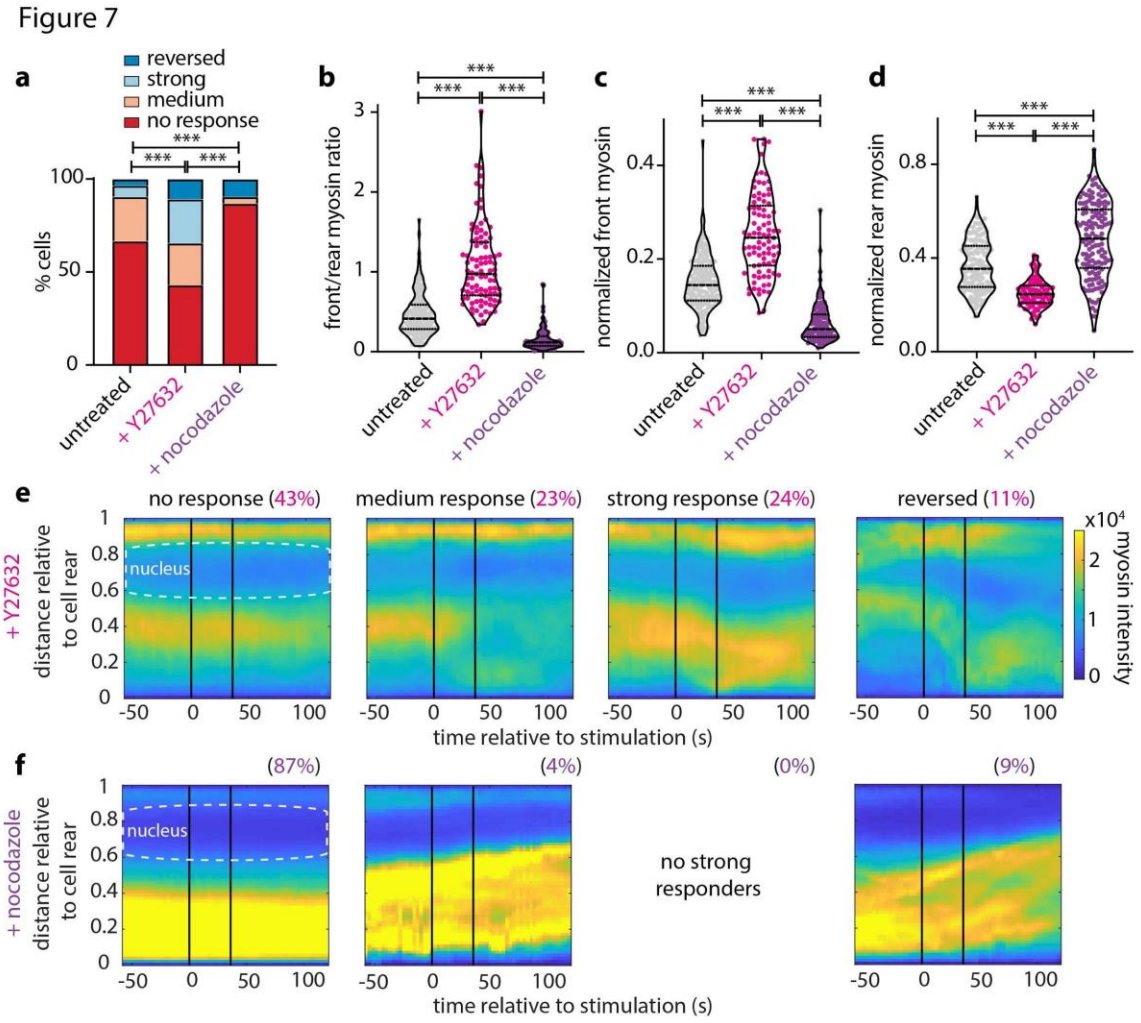

Figure 4.7 Myosin phosphorylation state alters the intracellular localization of myosin II and tunes the sensitivity of the cell rear.

(a) Stacked bar plots of percentage of cells exposed to transient stimulation that showed no response, medium response, strong response and reversed for n=147 untreated cells, for n=93 Y27632-treated, and n=137 nocodazole-treated cells (from 8, 10 and 8 independent experiments, respectively); p-values of Fisher exact tests (***: p<0.001). **(b-d)** Violin plots of mean front/rear myosin ratio **(b)**, normalized front myosin **(c)** and normalized rear myosin **(d)** averaging over 15 s prior to stimulation for the same conditions and cells shown in **(a)**; p-values of two-sided Wilcoxon rank sum test (***: p<0.001). **(e-f)** Average kymograph representation of myosin intensity as a function of time (x-axis) and vertical position relative

to the cell rear (y-axis) for cells treated with Y27632 (n=93) **(e)** and nocodazole (n=137) **(f)**. Vertical black lines indicate the start and stop of the pulsated stimulation.

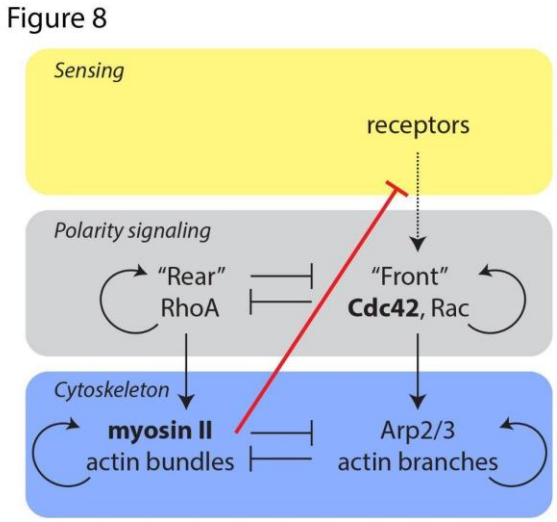

Figure 4.8 Simplified model of cell polarization.

Figure Neutrophil polarization is thought to arise through antagonism between front and rear signaling modules. Information is typically thought to flow from a sensing module containing receptors (yellow layer) to the polarity signaling circuit (grey layer), which guides organization of the cytoskeleton (blue layer). At the front of the cell, Cdc42 and Rac lead to Arp2/3 actin branch formation, while RhoA regulates myosin II actin bundles at the cell rear (vertical arrows). The front and rear signaling modules are mutually exclusive[3] and are governed by positive feedback loops (semicircular arrows) for self-amplification and polarity maintenance[5–7]. This particular signaling scheme has been demonstrated to be the most robust general motif that gives a stable polarization[42]. Similarly, the cytoskeleton also exhibits positive self-reinforcement and mutual inhibition by the different actin organizations[23,43–46]. Signaling has usually been perceived to be upstream of the cytoskeleton, informing cytoskeletal responses. Our work revealed that

myosin II is capable of blocking any detectable response downstream of receptor activation, even at the level of Cdc42 activity (red line).

4.15 Supplementary Information

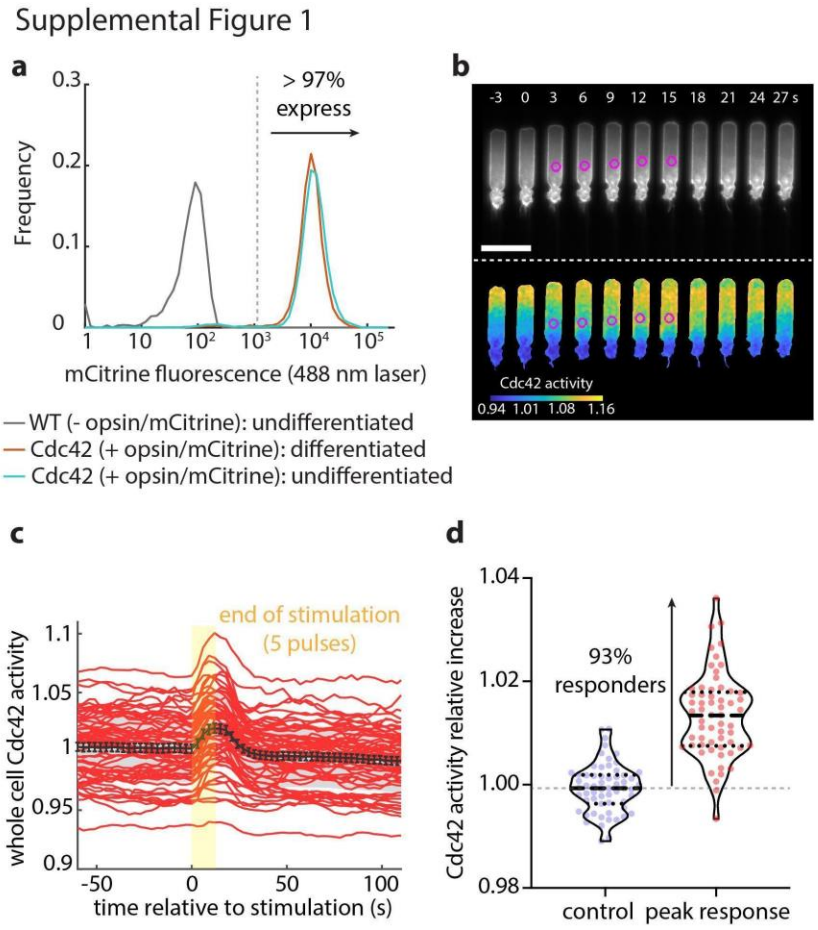

Supplementary Figure 4.1 Flow cytometry and center stimulation assay reveal that almost all cells are expressing the opsin receptor and that activated receptors signal to Cdc42.

(a) Flow cytometry measurement for mCitrine fluorescence of n=9972 differentiated (red) and n=10019 undifferentiated (cyan) HL60 cells expressing parapinopsin (tagged with mCitrine) and a red/far-red Cdc42 FRET sensor. Wild type cells (n=9904) not expressing the opsin used as control (grey). **(b)** Live-cell imaging snapshots of a representative center stimulation experiment on an HL60 cell expressing parapinopsin and the Cdc42 FRET sensor. Cells migrate unperturbed for 60 s before administering 5 pulses

at their centroid (magenta circles). Upper and lower panels show the registered sensors (grey scale) and the computed Cdc42 activity, respectively. Images captured every 3 s and subsampled for illustration purposes. Scale bar: 25 μm. **(c)** Mean Cdc42 activity averaged over the entire cell body over time (n=60 cells from 6 independent experiments) stimulated 5 times at their centroid (red lines: individual cells, black line: mean, grey shaded region: SD, error bars: SE). Rectangular yellow shaded region represents the start and end of the 5-pulse stimulation. **(d)** Violin plots of the relative increase of Cdc42 activity over a control zone and over the peak response zone for the same cells shown in **(c)**. Dashed grey line represents the threshold as defined by the median of the control response distribution.

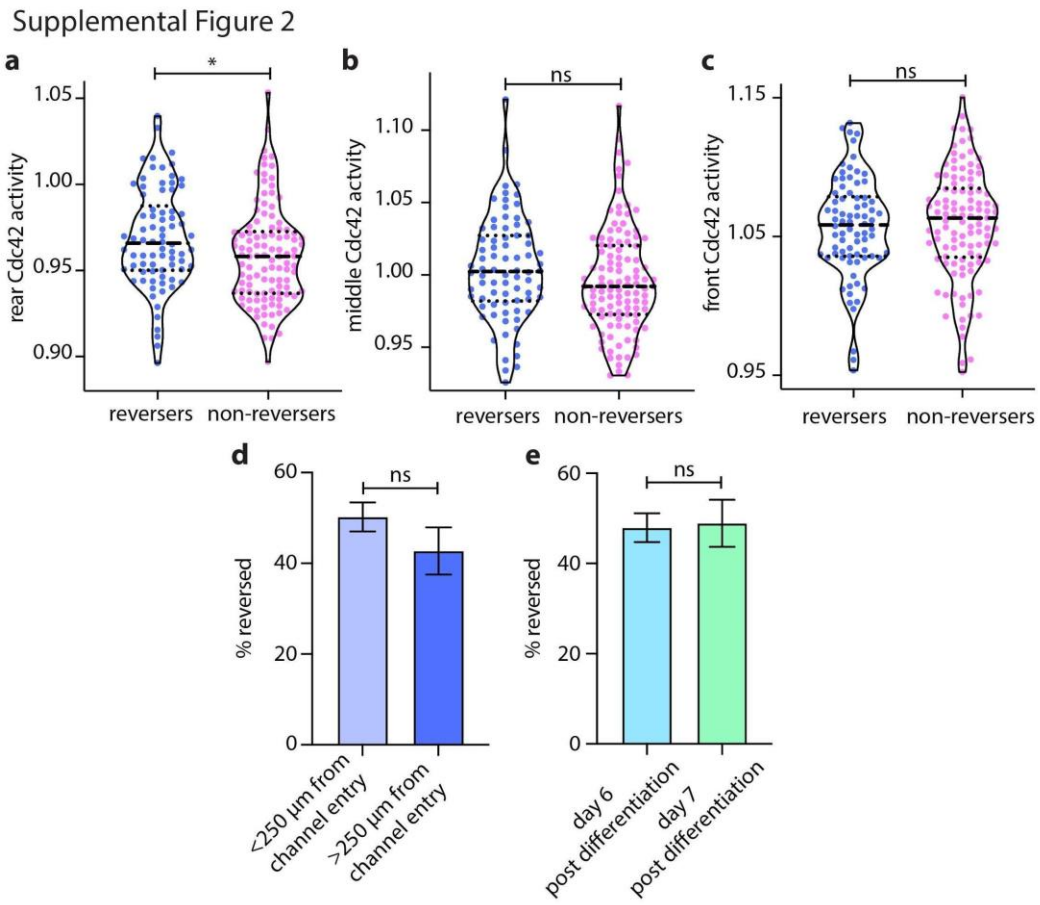

Supplementary Figure 4.2 Subcellular analysis reveals that non-reversers have a stronger rear as compared to reversing cells.

(a-c) Violin plots of mean cell rear **(a)**, cell middle **(b)**, and cell front **(c)** Cdc42 activity of n=78 reversers and n=110 non-reversers, averaging over 15 s prior to initiating persistent rear stimulation; p-values of two-sided Wilcoxon rank sum test (* represents $p<0.05$, ns represents $p>0.05$). **(d-e)** Bar plots of the percentage of cells that reversed stratified by the distance from the channel entrance **(d)**; closer to the channel entry: distance from entry <250 µm (n=247 cells), farther from channel entry: distance>250 µm (n=89 cells) as well as stratified by their differentiation age **(e)**: day 6 (n=244 cells), day 7 (n=92 cells). Error bars represent confidence intervals assuming a binomial distribution around the cumulative mean of each group and Fisher exact test revealed no significant difference between the compared conditions ($p>0.05$).

Supplemental Figure 3

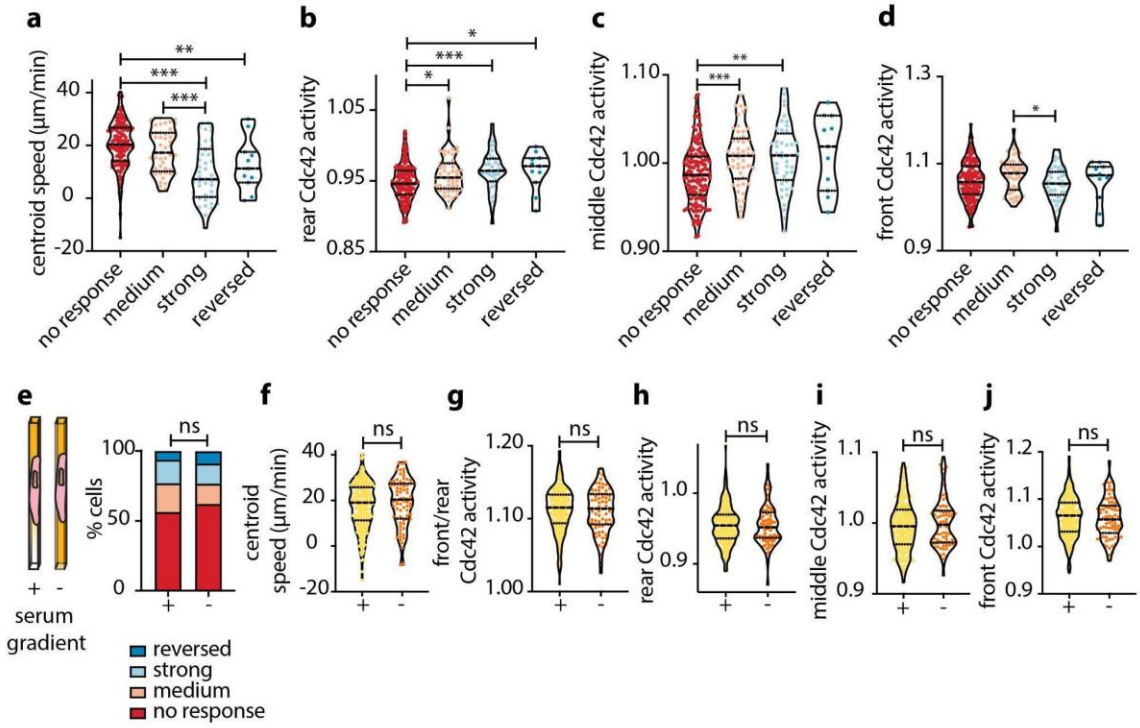

Supplementary Figure 4.3 Behavioral responses are due in part to pre-existing variation in Cdc42 polarity, which is independent of the serum gradient.

(a-d) Violin plots of mean centroid speed **(a)**, and mean cell rear **(b)**, cell middle **(c)**, and cell front **(d)** Cdc42 activity of n=141 non-responders, n=49 medium responders, n=44 strong responders, and n=11 reversers, averaging over 15 s prior to initiating 12-pulse stimulation; p-values of two-sided Wilcoxon rank sum test (*: $p<0.05$, **: $p<0.01$, ***: $p<0.001$, pairs not shown have $p>0.05$). **(e)** Stacked bar plots of the percentage of cells that showed no response, medium response, strong response and reversed for n=264 cells that migrated up a serum gradient and for n=101 cells that migrated in a homogeneous serum environment (from 20 and 6 independent experiments, respectively), fisher exact test revealed no significant difference between the two conditions ($p>0.05$). **(f-j)** Violin plots of mean centroid speed **(f)**, and mean front/rear **(g)**, cell rear **(h)**, cell middle **(i)**, and cell front **(j)** Cdc42 activity of n=245 cells that migrated up

a serum gradient and n=75 cells that migrated in a homogeneous serum environment, averaging over 15 s prior to initiating 12-pulse stimulation; ns represents p>0.05 of two-sided Wilcoxon rank sum test.

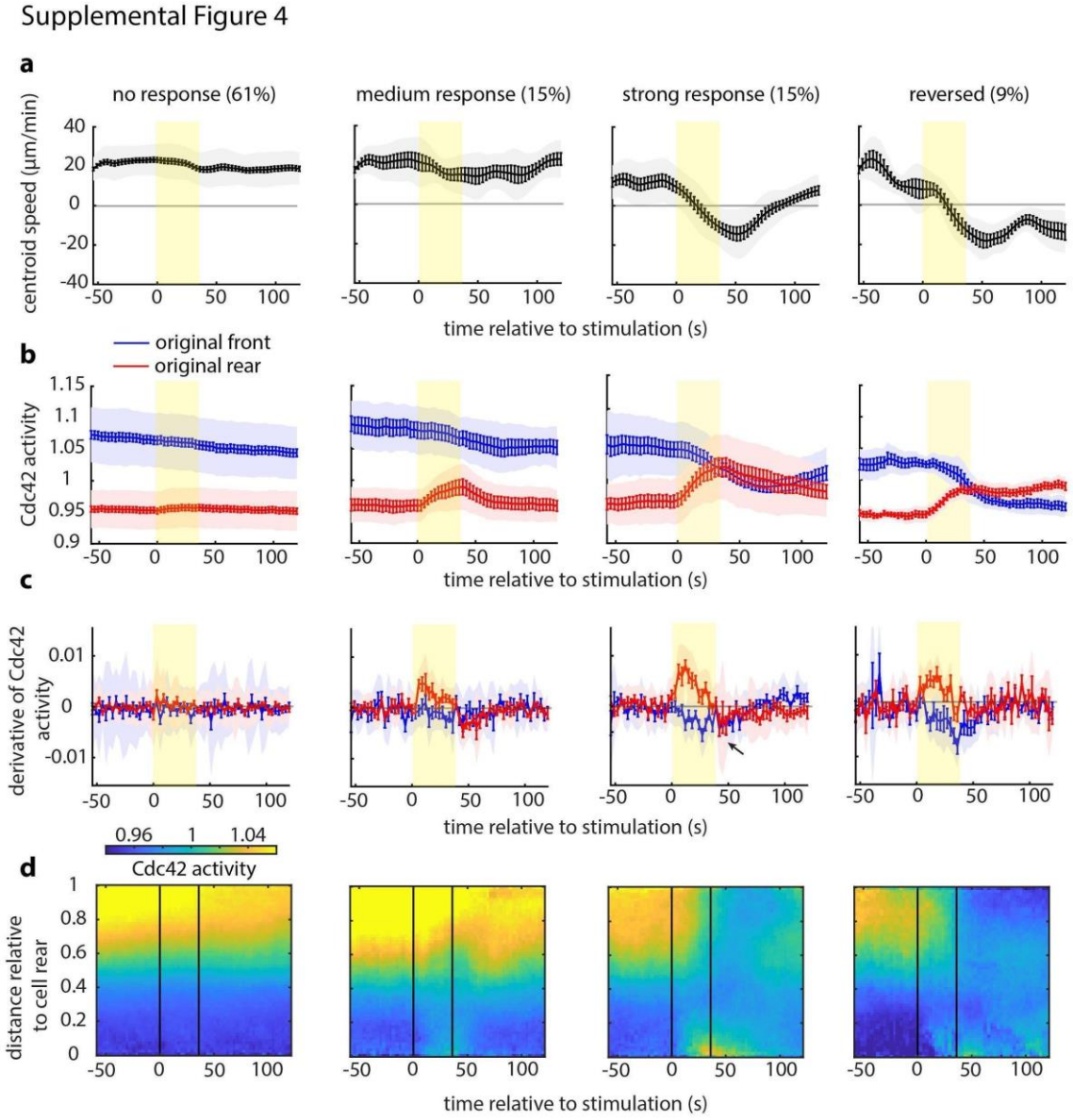

Supplementary Figure 4.4 Migratory and signaling responses are qualitatively similar with and without a serum gradient.

(a-c) Cell centroid speed **(a)**, mean Cdc42 activity **(b)** and derivative of Cdc42 activity **(c)** at the original front (blue) and rear (red) over time for each cellular response (lines: means, shaded regions: SD, error bars:

SE). Data are averages from n=46 non-responders, n=9 medium responders, n=13 strong responders, and n=7 reversers that migrated in a homogeneous serum environment from 6 independent experiments. Rectangular yellow shaded region marks the start and end of the 12-pulse stimulation. **(d)** Average kymograph representation of Cdc42 activity as a function of time (x-axis) and vertical position relative to the cell rear (y-axis) for non-responding, medium responding, strong responding and reversing cells. Vertical black lines indicate the start and end of the pulsated stimulation.

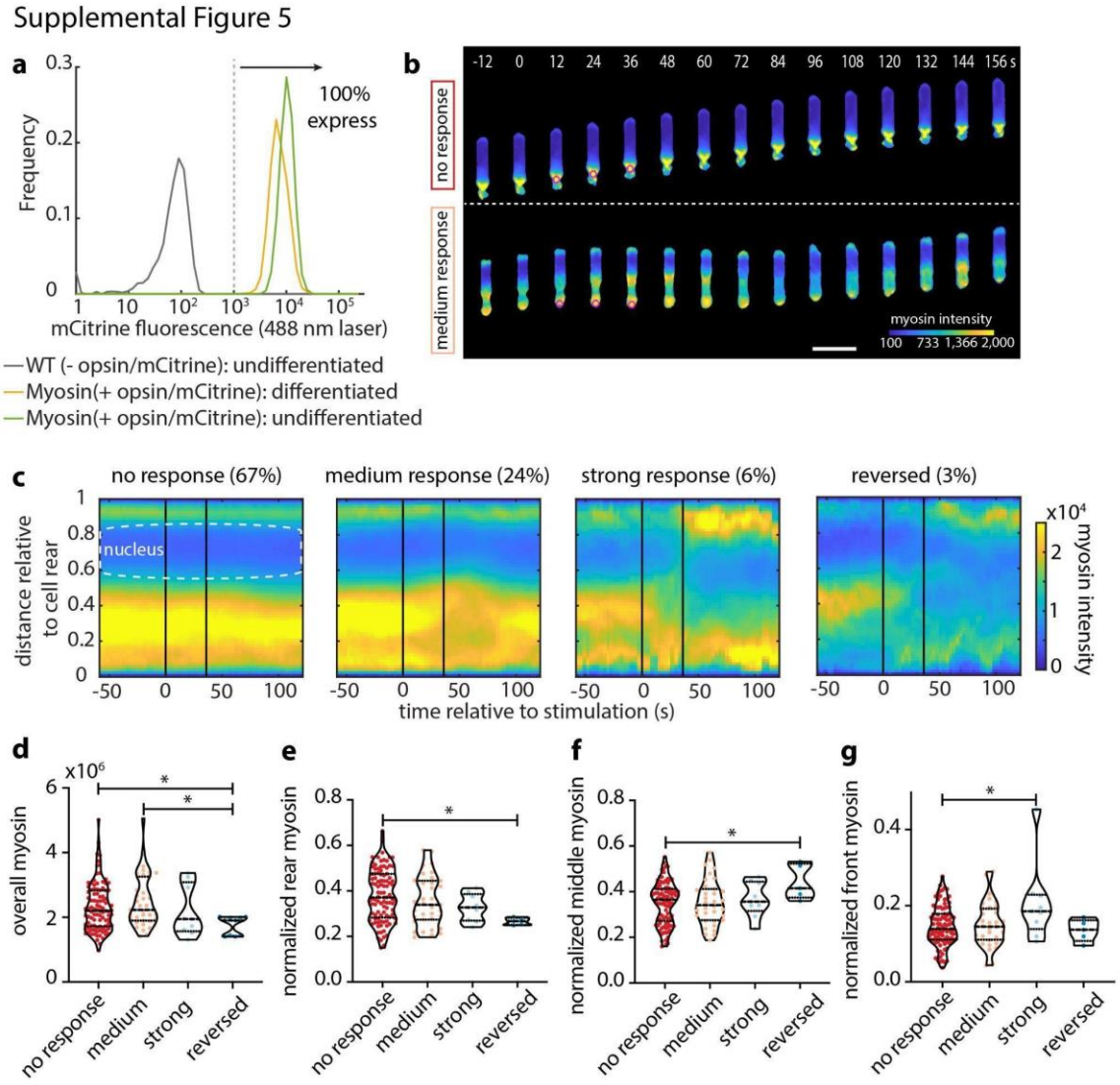

Supplementary Figure 4.5 Myosin quantification supports the idea that cellular responses are resulting from pre-existing variation.

(a) Flow cytometry measurement for mCitrine fluorescence of n=9990 differentiated (red) and n=10243 undifferentiated (purple) HL60 cells expressing parapinopsin (tagged with mCitrine), Myl9 and a cytosolic tag. Wild type cells, n=9904, not expressing the opsin used as control (grey). **(b)** Live-cell imaging snapshots of stimulation experiments with cells expressing parapinopsin and a myosin light chain sensor/cytosolic tag showing no response (upper panel) and a medium response (lower panel). Cells migrated unperturbed for 60 s prior to starting a transient 12-pulse stimulation at their cell rear (magenta

circles). Myosin intensity pseudo colored to facilitate visualization. Images captured every 3 s and subsampled for illustration purposes. Scale bar: 25 μm. **(c)** Average kymograph representation of myosin intensity as a function of time (x-axis) and vertical position relative to the cell rear (y-axis) of n=147 cells from 8 independent experiments stratified as non-responding, medium responding, strong responding and reversing cells. Vertical black lines indicate the start and end of the pulsated stimulation. **(d-g)** Violin plots of mean overall myosin **(d)**, mean normalized rear myosin **(e)**, mean normalized middle myosin **(f)**, and mean normalized front myosin **(g)** of n=147 cells, averaging over 15 s prior to initiating 12-pulse stimulation; p-values of two-sided Wilcoxon rank sum test (*: $p<0.05$, pairs not shown have $p>0.05$).

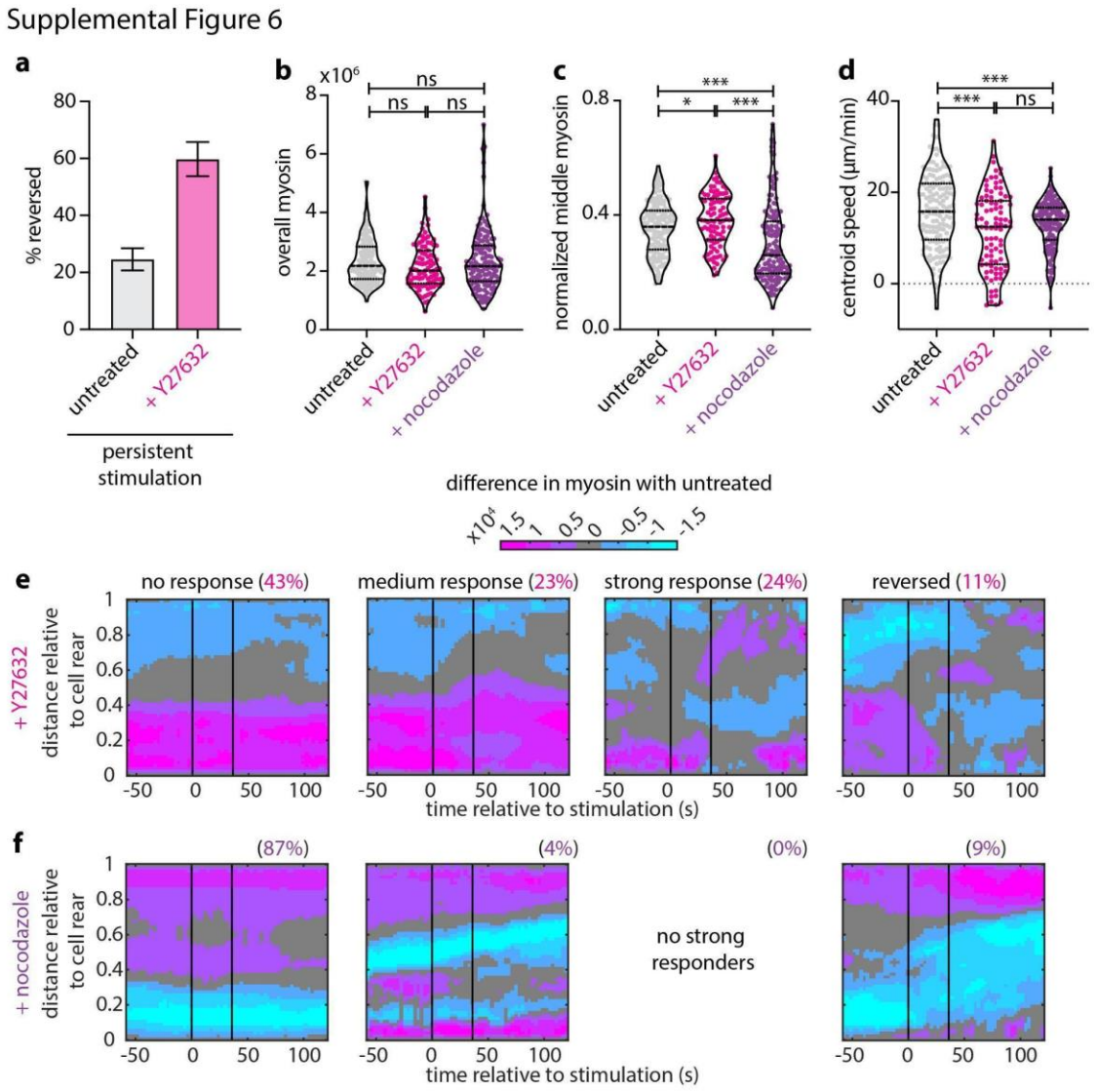

Supplementary Figure 4.6 Intracellular myosin localization depends on phosphorylation of myosin regulatory light chain.

(a) Bar plot of the percentage of myosin-expressing cells that reversed in response to persistent stimulation for n=122 untreated cells and n=67 Y27632-treated cells (from 5 and 4 independent experiments, respectively). Error bars represent confidence intervals assuming a binomial distribution around the cumulative mean of each group. Fisher exact test revealed a significant difference between the two conditions (***: p<0.001). **(b-d)** Violin plots of mean overall myosin **(b)**, mean normalized cell middle

myosin **(c)**, and mean centroid speed **(d)** for n=147 untreated cells, for n=93 Y27632-treated, and n=137 nocodazole-treated cells (from 10 and 8 independent experiments, respectively), averaging over 15 s prior to initiating 12-pulse stimulation; p-values of two-sided Wilcoxon rank sum test (*: $p<0.05$, ***: $p<0.001$, ns: $p>0.05$). **(e-f)** Average kymograph representation of the difference in myosin intensity as a function of time (x-axis) and vertical position relative to the cell rear (y-axis) between n=147 untreated cells and n=93 Y27832-treated **(e)**, and n=137 nocodazole-treated cells **(d)**, stratified as no responders, medium responders, strong responders and reverses (left to right) for 12-pulse stimulation assays. Vertical black lines indicate the start and end of the pulsated stimulation.

Chapter 5

Concluding Remarks

5.1 Conclusions

Neutrophils are capable of measuring chemoattractant concentration differences across the length of the cell, enabling spatially accurate chemotaxis[1,2]. To achieve this behavior, signals from chemoattractant GPCRs and their cognate $G_i\alpha$ family of heterotrimeric G-proteins are integrated by the underlying cell polarity cascade[3–5]. While several connections from the G-Proteins to downstream polarity regulators have been identified[6–9], the interplay between G-Proteins and the polarity circuit is highly complex and remains poorly understood. Indeed, the cell manages to encode local, spatial signals despite amplification of receptor cues during the polarization response[10,11]. How these opposing behaviors co-exist is unclear; however, specialization within the G-Protein and Rho GTPase levels likely plays a role[12,13]. Relatedly, because the polarity circuit is capable of spontaneous activation, whether the polarity cascade is always receptive to new receptors' inputs is enigmatic.

Addressing these questions requires local control over where receptors are activated to accurately measure how downstream polarity signals propagate in space and time. Experimentally, rapid diffusion of small chemoattractants is limiting as these signals will quickly activate receptors across the cell. To overcome this challenge, I developed an optogenetic chemotaxis receptor system that enables light-driven chemotaxis signaling. Additionally, I constructed a red-shifted, spectrally compatible biosensor for Cdc42, a cell polarity regulator that is predictive of cell turning. In Chapter 3, I used these tools to investigate spatial signal transduction in the Cdc42 polarity circuit. Because signal amplification inherent to the polarity cascade could spread receptor cues, I tested the hypothesis that negative regulation downstream of receptor activation balances the amplification response. I found that the Cdc42 circuit is optimized to limit the spatial spread and duration of the response. Additionally, I found that negative

feedback from endogenous Cdc42 and F-actin are required for accurate spatial signal processing[14]. Collectively, these results further indicate that Cdc42 is playing a central role in regulating spatial signal processing for accurate cell steering during neutrophil chemotaxis.

Migrating neutrophils will often U-turn when presented with novel chemoattractant gradients rather than fully repolarize in a new direction[15]. This behavior raises the question of whether the cell rear is insensitive to new receptor inputs. In Chapter 4, I collaborated with Amalia Hadjitheodorou of the Theriot lab to test this hypothesis. We paired the optogenetic tools with 1-D microfluidic channels that physically prevent cells from U-turning. We found that local optogenetic receptor activation on the cell rear could indeed reverse cell polarity; however, only half of the population would complete the polarity reversal. We found that over 90% of cells were responding to the receptor input, suggesting that the cell rear was ignoring receptor cues. In support, we found that we could enhance or diminish cell repolarization events by tuning the strength of the cell rear polarity through the RhoA/Myosin II axis. Additionally, we found that strong cell rear polarity was refractory to receptor inputs at the level of Cdc42 signaling. These results indicate that heterogeneity in cell signaling state influences ability of cells to respond to new receptor inputs[16].

In total, my dissertation research has advanced the chemotaxis field by developing new methodologies while also contributing novel insights into the interplay between directional sensing and cell polarity pathways.

5.2 Future Directions

Neutrophil spatial signal processing is highly optimized, allowing cells to accurately steer in shallow chemoattractant gradients[1,2]. This signaling network is known to contain connections from GPCRs to the downstream cell polarity cascade, however the molecular mechanisms that underpin directional accuracy during cell steering remain unknown. Building on work from my dissertation, I

envision two future projects that represent the logical next steps in deciphering how spatial information is stored in the chemotaxis pathway.

The directional sensing pathway is known to contain the chemotaxis receptors and the $G_i\alpha$ family of heterotrimeric G-Proteins[4,5,17]. Importantly, G-protein signaling must inherently contain directional information regarding the extracellular chemoattractant gradient, yet how that information is transmitted downstream remains unclear. RGS proteins function as GAPs for the Gα subunit, which stimulate GTP hydrolysis and limit the lifetime of active G-protein subunits[18]. I hypothesize that directional information is encoded by the spatial activity pattern of the G-proteins and that negative regulation by RGS proteins is critical for maintaining directionally accurate information. To test this hypothesis, future work will take advantage of $G_i\alpha$ CRISPR knockouts coupled with a $G_i\alpha$ mutant that no longer interacts with RGS proteins[19]. The mutant cell line can then be combined with the parapinopsina and TomKat Cdc42 fret sensor tools to determine if prolonging the heterotrimeric G-proteins cycle alters the global Cdc42 kinetics as well as the Cdc42 spatial signaling response. Additionally, the RGS-insensitive mutant will be tested in the HT-chemotaxis assay to determine if the loss of RGS impairs the cell's directional accuracy. Finally, there are more than 20 RGS proteins, and the identity of the RGS regulators for the chemotaxis response are unknown. Arrayed screening using CRISPR-interference will be used in conjunction with the parapinopsina and Cdc42 TomKat sensor to perturb all expressed RGS proteins in neutrophils. The temporal kinetics of the Cdc42 response will be used as the screen readout. Importantly, the Cdc42 response phenotype of the RGS-insensitive mutant will serve as the positive control. Collectively, these proposed experiments will help elucidate whether disrupting the G-Protein cycle kinetics alter the spatial accuracy of the directional sensing circuit. Additionally, this project will also identify the specific RGS regulators of chemotaxis signaling.

Thus far, the cell polarity network has functional redundancy and interconnected feedback loops that have been challenging to decipher. In neutrophils, there are over 100 expressed GAP and GEF regulators that control Rho-GTPases dynamics[20]. These GAP and GEF regulators likely exhibit context

dependent signaling that fuel the complex, inter-connected nature of the cell polarity circuit[21]. Understanding which GAP and GEF regulators control specific features of the chemotaxis response, especially response directional accuracy, would be a breakthrough in the field. Realistically, a systems level approach is required to identify the specific GAP and GEF regulators. Excitingly, the improved spatial and temporal control over receptor stimulation using parapinopsina allows for the detection of Rho GTPase signaling network features that would be impossible to discern with diffusible chemoattractants. Thus, for a second project, I anticipate that the network features of the Cdc42 response can be used as phenotypes for systematic screening of chemotaxis regulators using CRISPR interference methodologies. The goal of this project will be to identify the GAP and GEF regulators that shape the Cdc42 signaling response. Indeed, the Collins lab has already embarked on this endeavor, and one GEF and two GAPs have been identified as hits. As TomKat sensors are developed for other Rho-GTPases, this modular screen could be expanded to include signaling response phenotypes for additional Rho-GTPases. Through identifying and validating hits for each GAP and GEF regulator, I expect a clearer picture of chemotaxis signaling to resolve as the mechanisms of each new regulator are elucidated. Ultimately, I think this work has the potential to unlock the next chapter of the chemotaxis field, similar to the discovery of the Rho-GTPases during the 1990s.

5.3 References

1. Zigmond, S. H. Ability of polymorphonuclear leukocytes to orient in gradients of chemotactic factors. *J. Cell Biol.* **75**, 606–616 (1977).

2. Zigmond, S. H. Mechanisms of sensing chemical gradients by polymorphonuclear leukocytes. *Nature* **249**, 450–452 (1974).

3. Van Haastert, P. J. M. & Devreotes, P. N. Chemotaxis: Signaling the way forward. *Nat. Rev. Mol. Cell Biol.* **5**, 626–634 (2004).

4. Devreotes, P. & Janetopoulos, C. Eukaryotic chemotaxis: distinctions between directional sensing and polarization. *J. Biol. Chem.* **278**, 20445–20448 (2003).

5. Weiner, O. D. Regulation of cell polarity during eukaryotic chemotaxis: the chemotactic compass. *Curr. Opin. Cell Biol.* **14**, 196–202 (2002).

6. Welch, H. C. *et al.* P-Rex1, a PtdIns (3, 4, 5) P 3-and Gβγ-regulated guanine-nucleotide exchange factor for Rac. *Cell* **108**, 809–821 (2002).

7. Li, Z. *et al.* Directional sensing requires Gβγ-mediated PAK1 and PIX alpha-dependent activation of Cdc42. *Cell* **114**, 215–27 (2003).

8. Stephens, L. *et al.* A novel phosphoinositide 3 kinase activity in myeloid-derived cells is activated by G protein βγ subunits. *Cell* **77**, 83–93 (1994).

9. Hawkins, P. T., Stephens, L. R., Suire, S. & Wilson, M. PI3K signaling in neutrophils. in *Phosphoinositide 3-kinase in Health and Disease* 183–202 (Springer, 2011).

10. Janetopoulos, C., Jin, T. & Devreotes, P. Receptor-mediated activation of heterotrimeric G-proteins in living cells. *Science* **291**, 2408–2411 (2001).

11. Servant, G. *et al.* Polarization of Chemoattractant Receptor Signaling During Neutrophil Chemotaxis. *Science* **287**, 1037–1040 (2000).

12. Collins, S. R. *et al.* Using light to shape chemical gradients for parallel and automated analysis of chemotaxis. *Mol. Syst. Biol.* **11**, 804 (2015).

13. Yang, H. W., Collins, S. R. & Meyer, T. Locally excitable Cdc42 signals steer cells during chemotaxis. *Nat Cell Biol* **18**, 191–201 (2016).

14. Bell, G. R. R., Rincón, E., Akdoğan, E. & Collins, S. R. Optogenetic control of receptors reveals distinct roles for actin- and Cdc42-dependent negative signals in chemotactic signal processing. *bioRxiv* 2021.04.03.438340 (2021) doi:10.1101/2021.04.03.438340.

15. Iijima, M., Huang, Y. E. & Devreotes, P. Temporal and Spatial Regulation of Chemotaxis. *Dev. Cell* **3**, 469–478 (2002).

16. Hadjitheodorou, A. *et al.* Directional reorientation of migrating neutrophils is limited by suppression of receptor input signaling at the cell rear through myosin II activity. *bioRxiv* 2021.04.04.438336 (2021) doi:10.1101/2021.04.04.438336.

17. Xu, J. *et al.* Divergent signals and cytoskeletal assemblies regulate self-organizing polarity in neutrophils. *Cell* **114**, 201–14 (2003).

18. Siderovski, D. P. & Willard, F. S. The GAPs, GEFs, and GDIs of heterotrimeric G-protein alpha subunits. *Int. J. Biol. Sci.* **1**, 51–66 (2005).

19. Fu, Y. *et al.* RGS-insensitive G-protein mutations to study the role of endogenous RGS proteins. *Methods Enzymol.* **389**, 229–243 (2004).

20. Rincón, E., Rocha-Gregg, B. L. & Collins, S. R. A map of gene expression in neutrophil-like cell lines. *BMC Genomics* **19**, 573 (2018).

21. Müller, P. M. *et al.* Systems analysis of RhoGEF and RhoGAP regulatory proteins reveals spatially organized RAC1 signaling from integrin adhesions. *Nat. Cell Biol.* **22**, 498–511 (2020).